

Aus dem Institut für Physiologie und Pathophysiologie

Geschäftsführender Direktor: Prof. Dr. Dominik Oliver  
des Fachbereichs Medizin der Philipps-Universität Marburg

Characterization of *Drosophila* Swiprosin-1,  
a novel conserved actin cross-linking protein,  
controlling immune cell migration,  
wound closure and regulated exocytosis

Inaugural-Dissertation zur Erlangung des  
Doktorgrades der Naturwissenschaften

dem Fachbereich Medizin der Philipps-Universität Marburg  
vorgelegt von

**Franziska Lehne**

aus Braunschweig

Marburg, 2022

Angenommen vom Fachbereich Medizin  
der Philipps-Universität Marburg am: 25.08.2022

Gedruckt mit Genehmigung des Fachbereichs Medizin

Dekanin: Frau Prof. Dr. D. Hilfiker-Kleiner

Referent: Herr Prof. Dr. S. Bogdan

1. Korreferent: Herr Prof. Dr. R. Jacob

## Summary

Filamentous actin (F-actin) is a dynamic polymer providing mechanical forces to change cell morphology. Calcium is a known modulator of actin cytoskeleton organization, required for many cellular functions including cell migration, wound closure and exocytosis. EFHD2/Swiprosin-1 (Swip-1) is an actin-binding protein that can link calcium directly to actin network rearrangements.

Upregulation of Swip-1 has been found in a number of pathologies including neurodegenerative diseases and invasive cancer highlighting its importance to study. A role of Swip-1 in cell migration had been previously shown, however, how Swip-1 regulates the underlying F-actin rearrangements, especially in response to calcium, had not been solved, yet.

*Drosophila* Swip-1 is upregulated in highly motile pupal macrophages and localizes to the protruding lamellipodia. CRISPR/Cas9-mediated *swip-1* null mutants are viable, fertile but their macrophages display disrupted lamellipodia formation and defects in integrin-dependent migration. Moreover, Swip-1 is also crucial for the rapid reorganization of F-actin at a wound edge necessary for the healing process to re-establish tissue integrity. Single-cell ablation in the *Drosophila* larval epidermis showed dramatic reduction of wound closure in *swip-1*-deficient flies. Rescue experiments unambiguously showed that calcium binding to Swip-1 is essential for lamellipodia formation for both migration and wound closure.

Mechanistically, Swip-1 can cross-link actin networks. Upon calcium ion binding to Swip-1 these crosslinks become transient, relaxing the actin meshwork and allowing severing and branching to take place. At low calcium levels, Swip-1 stabilizes this network. Notably, the calcium-dependent cross-linking activity had previously not been addressed.

A stable yet dynamic network is also required for regulated exocytosis of secretory vesicles in the *Drosophila* larval salivary gland. Here, Swip-1 is necessary for the efficient cargo expulsion to the lumen. However, the regulatory mechanism seems to be independent of its calcium binding. Rather, changes in phosphorylated non-muscle myosin II might change the contractility of the F-actin coat surrounding the vesicles. This suggests a role of Swip-1 in a signal pathway upstream of the phosphorylation of myosin regulatory light chain.

## Zusammenfassung

Filamentöses Aktin (F-Aktin) ist ein dynamisches Polymer, dessen Kraftentwicklung die Zellmorphologie verändern kann. Kalzium ist ein bekannter Modulator der Aktin-Zytoskelettorganisation und ist für viele Zellfunktionen erforderlich. Diese umfassen unter anderem Zellmigration, Wundverschluss und Exozytose. EFHD2/Swiprosin-1 (Swip-1) ist ein Aktin-bindendes Protein, das Kalzium direkt mit den hervorgerufenen Veränderungen des Aktin-Netzwerks verknüpfen kann. Übermäßige Expression von Swip-1 tritt bei vielen Pathologien auf, darunter neurodegenerative Erkrankungen und invasiver Krebs. Dies unterstreicht die Bedeutung der Funktionsuntersuchung von Swip-1. Eine Rolle von Swip-1 bei der Zellmigration wurde bereits gezeigt, jedoch konnte noch nicht geklärt werden, wie Swip-1 die zugrunde liegende Umgestaltung des Aktin-Netzwerkes reguliert, insbesondere die Reaktion auf eine Veränderung der Kalziumkonzentration.

*Drosophila* Swip-1 ist in hoch motilen pupalen Makrophagen hochreguliert und lokalisiert in ihren Lamellipodien. CRISPR/Cas9-vermittelte *swip-1*-Nullmutanten sind lebensfähig, fertil und zeigen keine äußerlichen Veränderungen, aber ihre Makrophagen zeigen eine gestörte Lamellipodienbildung und Defekte in der Integrin-abhängigen Migration. Darüber hinaus ist Swip-1 auch entscheidend für die schnelle Reorganisation von Aktin im epithelialen Wundverschluss um die Gewebeintegrität wiederherzustellen. In *swip-1*-defizienten Fliegen zeigte die Ablation von einzelnen Zellen in der *Drosophila* larvalen Epidermis eine dramatische Beeinträchtigung des Wundverschlusses. Rettungsexperimente zeigten eindeutig, dass die Kalziumbindung an Swip-1 für die Bildung von Lamellipodien sowohl in der Migration als auch für den Wundverschluss unerlässlich ist.

Mechanistisch gesehen kann Swip-1 Aktin-Netzwerke durch Homodimerisierung vernetzen. Nach der Bindung von Kalziumionen an Swip-1 werden diese Quervernetzungen kurzlebiger, wodurch das Aktin-Netzwerk aufgelockert wird. Hierdurch wird die Bindung von Proteinen ermöglicht, die Aktinfilamente trennen und so neue Verzweigungen fördern. Bei einer niedrigen Kalziumkonzentration stabilisiert Swip-1 dieses neue Netzwerk dann wieder. Bemerkenswerterweise wurde diese Kalzium-abhängige Vernetzungsaktivität in vorherigen Arbeiten übersehen.

Ein stabiles und dennoch dynamisches Netzwerk ist auch für die regulierte Exozytose sekretorischer Vesikel in der Speicheldrüse der *Drosophila* Larve erforderlich. Hier ist Swip-1 für den effizienten Cargo-Ausstoß zum Lumen notwendig. Allerdings scheint hier

der Regulationsmechanismus unabhängig von der Bindung des Kalziums an Swip-1 zu sein. Vielmehr könnten Veränderungen der Phosphorylierung von Myosin der Klasse II der nicht-Muskelzellen die Kontraktilität der F-Aktin-Hülle, die die Vesikel umgibt, verändern. Dies deutet auf eine Rolle von Swip-1 in einem Signalweg der Phosphorylierung der regulatorischen leichten Kette des Myosins hin.

# TABLE OF CONTENTS

SUMMARY .....	I
ZUSAMMENFASSUNG .....	II
LIST OF FIGURES .....	IV
LIST OF USED ABBREVIATIONS .....	V
<b>1 INTRODUCTION .....</b>	<b>1</b>
1.1 ACTIN FORMS DYNAMIC FILAMENTS SHAPING CELLS .....	1
1.2 F-ACTIN ORGANIZATION INTO A DENDRITIC NETWORK IS HIGHLY REGULATED .....	1
1.3 <i>DROSOPHILA</i> AS A MODEL ORGANISM TO STUDY CELL MIGRATION .....	4
1.4 THE LAMELLIPODIUM AT THE FRONT OF CELL MOTILITY .....	5
1.5 CROSS-LINKING PROTEINS PROVIDE CONNECTIVITY TO F-ACTIN STRUCTURES.....	6
1.6 ACTOMYOSIN GENERATES FORCES NECESSARY FOR CELL SHAPE CHANGES .....	8
1.7 <i>DROSOPHILA</i> AS MODEL ORGANISM TO STUDY WOUND CLOSURE .....	10
1.8 CALCIUM IS A REGULATOR FOR ACTIN DYNAMICS.....	13
1.9 SWIPROSIN-1/EFHD2 IS A CALCIUM- AND F-ACTIN-BINDING PROTEIN .....	15
1.10 AIM OF THIS WORK.....	17
<b>2 PUBLICATIONS.....</b>	<b>2</b>
2.1 PUBLICATION 1 .....	2
2.2 PUBLICATION 2 (UNDER REVIEW) .....	25
<b>3 ADDITIONAL METHODS.....</b>	<b>49</b>
3.1 KYMOGRAPH ANALYSIS OF MACROPHAGES .....	49
3.2 FLUORESCENCE RECOVERY AFTER PHOTBLEACHING (FRAP) .....	49
3.3 AUTOMATED DETECTION AND ANALYSIS OF PROTRUSIONS (ADAPT).....	50
3.4 VESICLE SIZE IN LARVAL SALIVARY GLANDS .....	50
3.5 RECRUITMENT OF PROTEIN OF INTEREST TO SECRETING VESICLE MEMBRANE .....	50
3.6 CRUMPLING ANALYSIS OF SECRETING VESICLES .....	51
3.7 PROTEIN PURIFICATION .....	51
3.8 LOW-SPEED ACTIN CO-SEDIMENTATION ASSAY .....	51
3.9 SIZE EXCLUSION CHROMATOGRAPHY .....	52
3.10 QUANTIFICATION OF DIRECTED MIGRATION OF MACROPHAGES .....	52
<b>4 ADDITIONAL RESULTS.....</b>	<b>53</b>
4.1 SWIP-1 LOCALIZES TO PROTRUDING LAMELLIPODIA.....	53
4.2 SWIP-1'S COILED-COIL DOMAIN IS REQUIRED FOR F-ACTIN CROSS-LINKING .....	55
4.3 SWIP-1 CALCIUM BINDING AND DIMERIZATION ARE NECESSARY FOR LAMELLIPODIA-BASED MIGRATION OF MACROPHAGES .....	56
4.4 ACTIVE NON-MUSCLE MYOSIN II HAS A DIFFERENT LOCALIZATION PATTERN IN MACROPHAGES DEPENDING ON SWIP-1 PROTEIN LEVELS .....	59
4.5 LOSS OF SWIP-1 IMPAIRS ACTOMYOSIN CONTRACTION OF SECRETORY VESICLES.....	59
<b>5 DISCUSSION .....</b>	<b>63</b>
5.1 SWIP-1 IS HIGHLY EXPRESSED IN TISSUES THAT REQUIRE DYNAMIC CALCIUM-DEPENDENT ACTIN REMODELING .....	63
5.2 SWIP-1 CROSS-LINKS F-ACTIN IN A CALCIUM-DEPENDENT MANNER.....	63
5.3 LOSS OF <i>SWIP-1</i> INCREASES MACROPHAGE RANDOM MIGRATION THROUGH STABILIZATION OF FOCAL ADHESIONS .....	64
5.4 PROPOSED MODEL FOR SWIP-1 FUNCTION IN LAMELLIPODIA FORMATION FOR 2D CELL MIGRATION .....	66
5.5 WOUND CLOSURE IS DEPENDENT ON SWIP-1 TRANSIENT F-ACTIN CROSS-LINKS .....	67
5.6 SWIP-1 IS NECESSARY FOR REGULATED EXOCYTOSIS .....	69
5.7 LOSS OF <i>SWIP-1</i> MIGHT LEAD TO INCREASED NON-MUSCLE MYOSIN ACTIVATION.....	70

5.8	PHOSPHORYLATION OF HUMAN EFHD2 MIGHT ACT AS A SWITCH FROM F-ACTIN BUNDLING TO CROSS-LINKING ACTIVITY .....	71
5.9	UNDERSTANDING HOW EFHD2/SWIP-1 UPREGULATION CAUSES PATHOLOGIES .....	72
6	CONCLUSION AND OUTLOOK .....	74
7	REFERENCES .....	76
8	APPENDIX.....	VII
8.1	AUTHOR CONTRIBUTIONS.....	VII
8.2	<i>DROSOPHILA</i> TRANSGENIC LINES USED IN THIS WORK .....	VIII
8.3	PLASMIDS GENERATED IN THIS WORK .....	VII
8.4	LIST OF PCR PRIMERS .....	VII
8.5	VERZEICHNIS DER AKADEMISCHEN LEHRER UND LEHRERINNEN.....	IX
8.6	DANKSAGUNG .....	X

## List of figures

Figure 1 – The dendritic nucleation model for protrusion of the leading edge.....	2
Figure 2 – Scheme of the cellular actin organization. ....	3
Figure 3 – Actin network organization and the relationship of its connectivity to contractility. ....	7
Figure 4 – The structure of non-muscle myosin II. ....	9
Figure 5 – Scheme of the molecular clutch at the leading edge of a migrating cell.....	10
Figure 6 – Scheme of different <i>Drosophila</i> wound closure models.....	13
Figure 7 – Comparison of <i>Drosophila</i> Swip-1, human EFHD2 and human EFHD1.....	16
Figure 8 – Swip-1 localizes in the protruding lamellipodia of macrophages.....	54
Figure 9 – Swip-1’s binding of calcium impacts f-actin co-sedimentation and apparent complex size. ....	56
Figure 10 – Localization of Swip-1 variants in <i>ex vivo</i> macrophages.....	57
Figure 11 – Loss of <i>swip-1</i> leads to increased velocity of randomly migrating macrophages. ....	58
Figure 12 – Localization of active non-muscle myosin II is dependent on Swip-1 expression. ....	60
Figure 13 – Loss of <i>swip-1</i> reduces secretion efficiency by acting on the crumpling of vesicle membrane. ....	61
Figure 14 – Model for Swip-1’s function in lamellipodia formation.....	67



## List of used abbreviations

ABP	actin binding protein
ABS	actin binding site
ADAPT	automated detection and analysis of protrusions
ADP/ATP	adenosine diphosphate/triphosphate
AJ	adherens junction
Arp	actin-related protein
BCR	B-cell receptor
Ca <sup>2+</sup>	calcium (ions)
CC	coiled-coil
Cdk5	cyclin-dependent kinase 5
ConA	Concanavalin A
e.g.	exempli gratia, for example
ECM	extracellular matrix
EGF(R)	epidermal growth factor (receptor)
ER	endoplasmic reticulum
F-actin	filamentous actin
FN	fibronectin
fps	frames per second
FRAP	fluorescence recovery after photobleaching
G-actin	globular actin
GDP/GTP	guanosine diphosphate/triphosphate
GEF	guanine nucleotide exchange factor
GFP	green fluorescent protein
GST	glutathione S-transferase
h	hours
i.e.	id est, that is
JNK	c-Jun N-terminal kinase
LM	ligand mimic
LPS	lipopolysaccharide
Mg <sup>2+</sup>	magnesium (ions)
min	minutes
MLCK	myosin light chain kinase

MRLC	myosin regulatory light chain
NMII	non-muscle myosin II
p	phospho (indicates phosphorylated amino acid)
PBS	phosphate-buffered saline
PKC	protein kinase C
PMCA	plasma membrane Ca <sup>2+</sup> ATPases
Rho GTPase	Rho family of small guanosine triphosphatases
ROCK	Rho-associated kinase
s	seconds
S	serine
SERCA	sarcoendoplasmic reticular Ca <sup>2+</sup> ATPases
SG	salivary gland
Swip-1	EFHD2/Swip-1, Swiprosin-1
TCA	trichloroacetic acid
TIRF-M	total internal reflection microscopy
TRPM	transient receptor potential channel M
VN	vitronectin
WASp	Wiskott-Aldrich syndrome protein

# 1 Introduction

## 1.1 Actin forms dynamic filaments shaping cells

Just like the bones of our body the cytoskeleton gives a cell the structural integrity and the ability to interact with its environment. It is composed of four major components: actin, microtubules, intermediate filaments and septins (Wickstead & Gull, 2011). Because it is one of the cytoskeletal proteins, actin is also one of the most abundant proteins in eukaryotes. It is highly conserved across all domains of life with homologs relating structurally and functionally (Gunning et al., 2015; Pollard, 2016).

Actin is a globular protein (G-actin) that polymerizes spontaneously and reversibly into twisted polar helical filaments (F-actin) with so-called pointed and barbed ends (Pollard, 2016; Pollard & Borisy, 2003). Both ends have different polymerization and depolymerization kinetics giving the filament a polarity. The barbed or so called (+) end polymerizes more quickly than the pointed (–) end. During polymerization, the subunits at the barbed end flatten promoting the interaction with and addition of actin monomers (Chou & Pollard, 2019; Fujii et al., 2010). However, the nucleation of a *de novo* actin filament, i.e. the dimerization and the subsequent addition of a third actin monomer, is kinetically unfavorable (Pollard & Borisy, 2003; Sept & McCammon, 2001).

## 1.2 F-actin organization into a dendritic network is highly regulated

In order to overcome these unfavorable kinetics, the cell can make use of different proteins aiding the assembly of G-actin into filaments. For instance, the formin family of proteins can assemble into donut shaped dimers which bind energetically unstable actin dimers and trimers to establish a stable filament nucleus. Continuously, formins associate with the barbed end of F-actin in a processive fashion, thereby increasing the rate of elongation exceeding spontaneous assembly. This leads to long unbranched filaments found in protrusions like filopodia (Courtemanche, 2018; Pollard, 2007).

Furthermore, actin-related proteins (Arp) are structurally very similar to G-actin (Goley & Welch, 2006). A complex of Arp2, Arp3 and five additional subunits (Arp1–5) form the Arp2/3-complex. This complex can polymerize F-actin at the site of an existing mother filament (Rouiller et al., 2008). In order to overcome the first kinetically unfavorable step of filament polymerization, the complex binds to the mother filament whereby Arp2 and Arp3 come in close proximity mimicking an actin dimer (Pollard &

Borisy, 2003; Rouiller et al., 2008). The Arp2/3-complex nucleates the new daughter actin filament at a 70° angle relative to the mother filament thus promoting a branched actin network (Blanchoin et al., 2000; Goley & Welch, 2006).

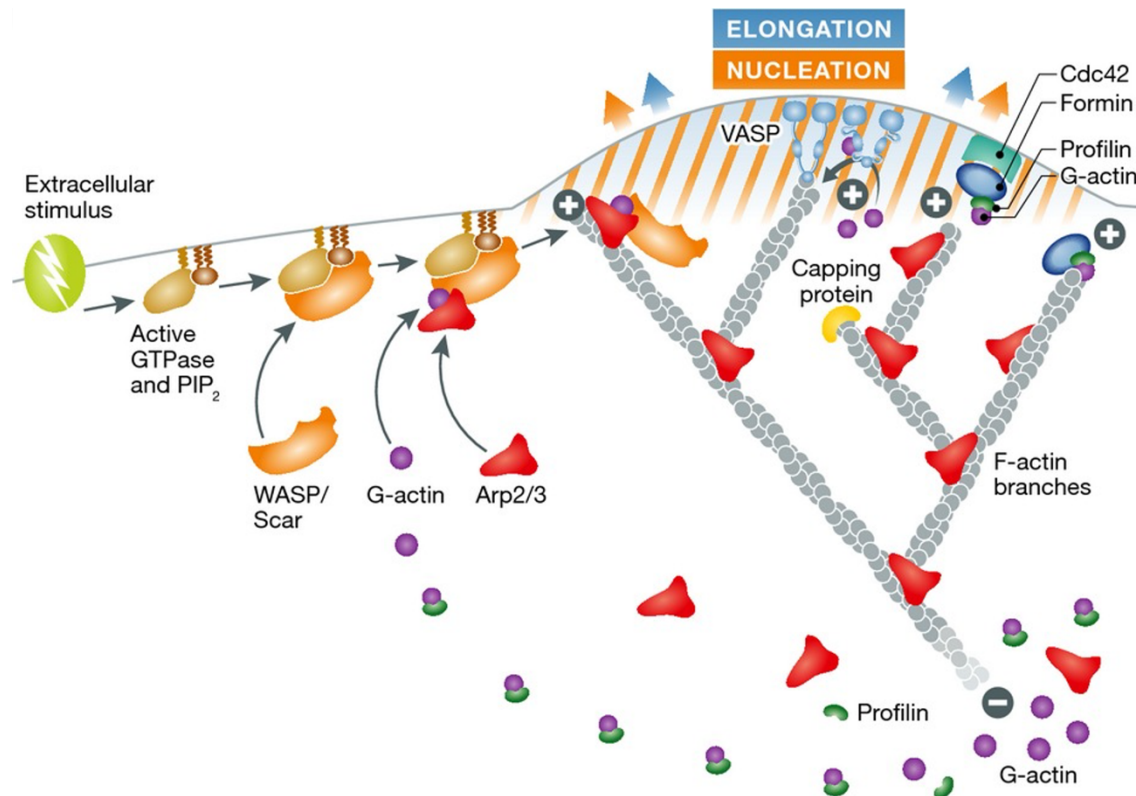


**Figure 1 – The dendritic nucleation model for protrusion of the leading edge from Pilo Boyl & Witke (2014).** Upon an extracellular stimulus small Rho GTPases are activated. These subsequently activate NPFs such as WASP/Scar. Therefore, this promotes Arp2/3-complex activation and a new daughter filament is assembled. The growing filaments push the plasma membrane forward until elongation is seized by capping proteins. The actin filaments age by hydrolysis of bound ATP and release of phosphate. Proteins of the ADF/cofilin family sever the filaments leading to ADP-bound G-actin monomers. The exchange of ADP to ATP is catalyzed by profilin making the monomers available for filament polymerization. Reprinted with permission granted by John Wiley and Sons under license number: 5316410033214

The dendritic nucleation hypothesis (Blanchoin et al., 2000; Pollard & Borisy, 2003) explains the establishment of an broad actin network and the observed actin treadmilling caused by faster polymerization at the barbed end than at the pointed end of a filament (Figure 1). The model takes into account different actin binding proteins (ABP) that modulate the concentration of free actin monomers available for polymerization as well as F-actin depolymerizing factors.

Upon an extracellular stimulus, signal pathways including Rho GTPases are activated. These lead to activation of nucleation promoting factors (NPF) such as the WASP and SCAR/WAVE family proteins at the cell membrane that can in turn activate the Arp2/3-complex (Blanchoin et al., 2000; Welch et al., 1997). Profilin-bound G-actin is supplied

to polymerize the new daughter filament, which can be stabilized by cortactin (Pollard, 2007). Growth of an actin filament is terminated by capping proteins and eventually filaments are disassembled through severing and debranching by cofilin. Severing exposes barbed ends that can continue growing and the dissociated actin monomers will be recycled and bound by profilin again to be added to growing filaments (Pollard & Borisy, 2003).

In protrusions, the barbed end is oriented towards the plasma membrane (Figure 1), therefore, net adding of new monomers from the profilin-actin pool leads to pushing of the cell cortex (Peskin et al., 1993; Pollard & Borisy, 2003; Svitkina, 2018). Simultaneously, the underlying actin network, called lamellum (Figure 2), is pushed back towards the cell center resulting in a retrograde flow of actin from the cell periphery to the center (Pollard & Borisy, 2003). This cycle of distal assembly and proximal disassembly of F-actin, called treadmilling, leads to a dynamic dendritic actin network allowing a cell to change shape and interact with its environment.

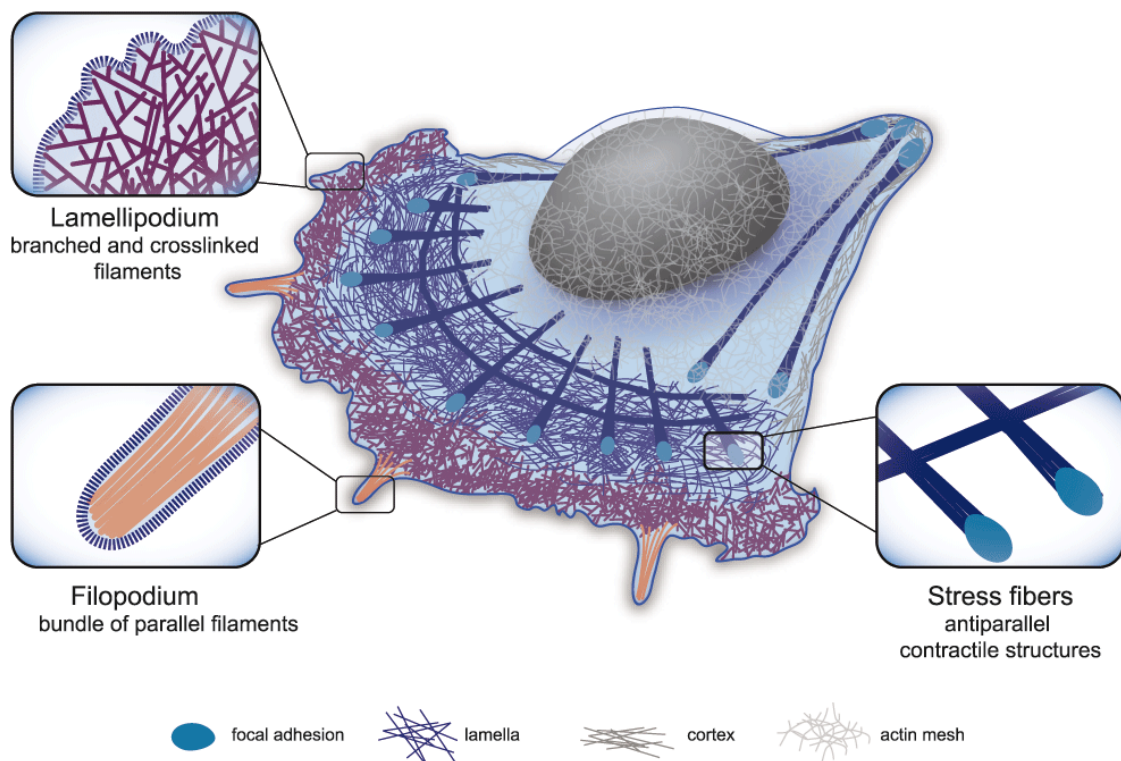


**Figure 2 – Scheme of the cellular actin organization from Letort et al. (2015).** Actin is mainly organized into three different structures. The dense, branched network of the lamellipodium, the finger-like filopodium of parallel actin bundles and the dynamic contractile structures of antiparallel or mixed-polarity actin filaments that associate with myosin such as stress fibers in the lamella. Reprint licensed under Creative Commons Attribution License.

Moreover, the molecular polarity of F-actin is crucial for the formation and function of actin structures such as stress fibers (anti-parallel filaments), filopodia (parallel F-actin bundles) or lamellipodia (branched F-actin network) (Figure 2; Blanchoin et al., 2014). To achieve these different structures, the assembly of F-actin needs to be highly regulated. Aforementioned Rho GTPases can alter a cell's protrusion behavior by specifically activating pathways resulting in different assembly patterns.

The three most important Rho GTPases are Rac, Cdc42 and RhoA. Rac and Cdc42 are upstream of the Arp2/3-complex thus promoting lamellipodia and filopodia formation, respectively. RhoA is upstream of the formin mDia which assembles, for example, stress fibers at focal adhesions (Kühn & Geyer, 2014; Ridley et al., 2003).

Consistent with their function, these Rho GTPases also have distinct localizations within a motile cell. While Rac and Cdc42 are active at the front of the cell, RhoA is at its rear. Maintaining this distribution, Rac and RhoA suppress each other's activity antagonistically (Ridley et al., 2003). Importantly, this provides a cell polarity crucial for directed migration.

### **1.3 *Drosophila* as a model organism to study cell migration**

Mesenchymal cell migration is defined by a cell's dynamic change of morphology, polarization and interaction with its environment. This efficient migration is a highly coordinated stepwise process of protrusion, adhesion, traction force generation to move the cell body and finally release of the cell rear (Lauffenburger & Horwitz, 1996). To study these processes *in vivo*, *Drosophila melanogaster* immune cells have emerged as a powerful model system.

The *Drosophila* innate immune system includes the cells of the hemolymph, called hemocytes, that exhibit conserved features of vertebrate blood cells. During *Drosophila* embryonic and larval development, these hemocytes arise from three distinct waves of hematopoiesis. The most abundant hemocyte cell lineage, about 95%, are the plasmatocytes which resemble vertebrate macrophages and are involved in developmental processes and pathogen defense mechanisms including phagocytosis and wound healing. Therefore, these macrophages need to actively migrate. Characteristically, they extend filopodia for sensing their environment and broad lamellipodial protrusions for their movement (Parsons & Foley, 2016). After pupa formation, polarized and highly motile *Drosophila* pupal macrophages can be easily isolated or imaged *in vivo*. Through site-specific single-cell laser-ablation, the directed

migration towards a wound site can be analyzed. Furthermore, *Drosophila* offers the advantage of easy genetic manipulations. Therefore, morphology analysis of the pupal macrophages permits insights into proteins involved in the establishment and regulation of protrusions, specifically the lamellipodium.

#### **1.4 The lamellipodium at the front of cell motility**

The broad spatially controlled planar lamellipodium (Figure 2; Pollard & Borisy, 2003; Small et al., 1998) is involved in formation of adhesions and, most importantly, its protruding leading edge is the site of the tightly regulated F-actin assembly (Geeves et al., 2005; Small et al., 2002). The leading edge is a thin compartment within the lamellipodium that is defined as the region at the plasma membrane where signaling cascades translate extracellular cues into rearrangement of the cytoskeleton thus controlling direction of movement (Figure 1; Falke & Ziemba, 2014).

In the past, there has been a debate how the lamellipodium is formed. The above-mentioned dendritic nucleation hypothesis assumes F-actin network assembly mainly via Arp2/3-complex-mediated branching (Figure 1). This would provide mechanical integrity through short actin branches which is necessary for cell motility (Blanchoin et al., 2000; Pollard & Borisy, 2003). On the other hand, a different model assumes F-actin nucleation only takes place at the leading edge and the lamellipodium actually consists of long, unbranched filaments (Koestler et al., 2008; Urban et al., 2010). However, the authors of the latter theory themselves mentioned later that the studies overlooked branching points distributed across the entire lamellipodial actin network (Vinzenz et al., 2012). They then concluded, the lamellipodium is a network of various filament lengths but decreased stiffness compared to a dense network of short, branched and persistent filaments (Vinzenz et al., 2012). Yet, for effective migration a cell needs a stable lamellipodium with filaments that withstand contractile forces. Therefore, the actin network needs to be anchored to a substrate via adhesion sites and overlapping actin filaments need to be reversibly linked (Svitkina, 2018; Ydenberg et al., 2011). The dynamic cross-linking of F-actin by different proteins and protein combinations can effectively adjust the mechanical properties of the F-actin network of the lamellipodium (Lieleg et al., 2010).

## 1.5 Cross-linking proteins provide connectivity to F-actin structures

For the mechanical integrity of cellular protrusions (Ydenberg et al., 2011), F-actin can be arranged into different higher order structures: from loosely cross-linked networks to tight and highly organized bundles (Figure 3A). While bundles are found in fine protrusions such as filopodia, cross-linked networks are important for the broad lamellipodium of a migrating cell. Several ABPs are known to bundle or cross-link actin filaments and although there seems to be a functional redundancy between different actin cross-linking proteins, it is interesting to analyze their synergistic behavior to alter the mechanical properties of the F-actin network. In the following, some examples of actin cross-linkers and their function will be given.

$\alpha$ -Actinin belongs to the highly conserved spectrin superfamily that forms rod-shaped proteins with spectrin repeats in the center, an actin binding site (ABS) at its N-terminus and a calmodulin-like domain composed of four EF-hands at its C-terminus. It forms antiparallel dimers to cross-link actin filaments. Alternative splicing of a single gene results in  $\alpha$ -actinin variants localizing in either muscle or non-muscle tissue. The isoforms can further be classified as calcium-insensitive (muscle) and calcium-sensitive (non-muscle) in which binding of calcium ions ( $\text{Ca}^{2+}$ ) to the EF-hand motifs regulate actin binding activity (Sjöblom et al., 2008). The non-muscle cytoskeletal isoform localizes to stress fibers and adhesion sites.  $\alpha$ -Actinin has been shown to synergistically act with the actin bundling protein fascin to enhance the mechanical resilience but also elasticity of F-actin networks *in vitro* (Tseng et al., 2002).

Fascin is a small monomeric protein that has one ABS at either terminus bundling F-actin into tight parallel bundles (Jayo & Parsons, 2010; Svitkina, 2018). It mainly localizes to stress fibers, filopodia, microspikes and invadopodia (Jayo & Parsons, 2010; Yamashiro et al., 1998). The *Drosophila* homolog *singed* has been shown to be specifically expressed in embryonic macrophages and loss of *fascin* impairs both their developmental dispersal in the embryo and the directed migration as a response to epithelial wounding (Zanet et al., 2009).

As another example of actin cross-linker cooperation, fascin and L-plastin act together in filopodia and invadopodia formation. Here, fascin offers the necessary structural rigidity while L-plastin promotes the elongation of the F-actin bundles (Van Audenhove et al., 2016). L-plastin is one of three distinct plastin isoforms (L-, T- and I-plastin) each encoded by a distinct gene. Plastins have two ABS and two N-terminal EF-hand motifs,



however, their  $\text{Ca}^{2+}$ -dependency for actin binding and bundling is variable and differs across species (Delanote et al., 2005; Giganti et al., 2005).

Noteworthy, overexpression of either L- or T-plastin in fibroblast-like cells leads to a reduced number and size of focal contacts (Arpin et al., 1994). Further highlighting their importance for cell migration, fascin and plastins are often associated with the invasiveness of cancer cells (Adams, 2004; Delanote et al., 2005; Sjöblom et al., 2008). Also, at high concentrations cross-linkers can arrange F-actin into bundles instead of an orthogonal network (Lieleg et al., 2010; Yamashiro et al., 1998). Different F-actin arrangements have an impact on the contractility of the network.

*In vitro* experiments have shown that the contractility is a function of actin organization and its connectivity provided by cross-linking proteins (Figure 3B). Ordered anti-parallel actin bundles show the highest, F-actin networks intermediate and disordered bundles of mixed polarity the lowest contractility. However, addition of cross-linkers reduced contractility of ordered bundles and networks while increasing it of disordered bundles (Ennomani et al., 2016).

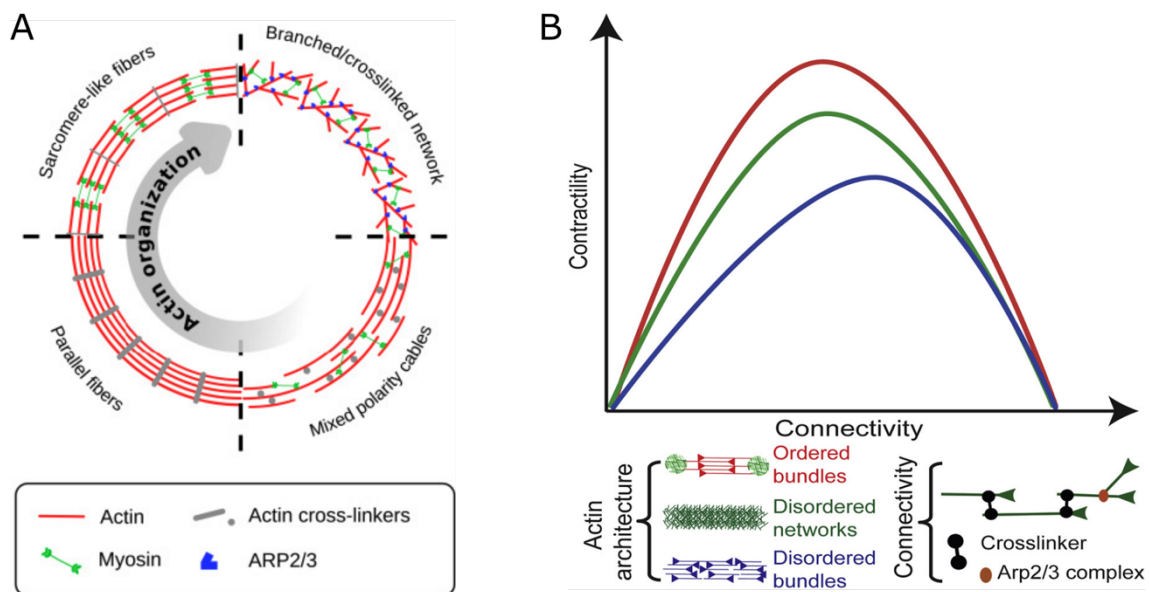


**Figure 3 – Actin network organization and the relationship of its connectivity to contractility.** (A) F-actin can be arranged into distinct actin network structures. (1) Arp2/3-complex generated networks can be cross-linked. F-actin can be linked into (2) cables of mixed filament polarity or (3) in parallel bundles with same direction. (4) Lastly, a high level of organization are sarcomere-like structures of repeating regular arrays of parallel F-actin. Contractile forces are generated by myosin motors. Reprinted from Schwayer et al. (2016) with permission from Elsevier. (B) The contractility of an actin structure is a function of its connectivity. There is an optimal number of cross-linkers present for maximal network contractility. Deviations from this leads to reduced contractility. Reprinted from Ennomani et al. (2016) with permission from Elsevier.

But not only the appropriate cross-linking of actin filaments is necessary for effective force generation and migration. Besides the pushing forces elicited by actin polymerization, contractile forces in the lamella are necessary (Figure 2). Organizing F-actin into bundles or networks through cross-linking proteins that have spacers between their ABS, allow motor proteins to bind and increase the efficiency of contraction (Svitkina, 2018).

## 1.6 Actomyosin generates forces necessary for cell shape changes

For the cellular integrity, actin acts together with myosin forming the actomyosin network that e.g. forms the contractile lamella or stabilizes the cell cortex (Agarwal & Zaidel-Bar, 2019; Blanchoin et al., 2014; Laevsky & Knecht, 2003). The contractile force of the actomyosin network is established by ATP-dependent sliding of myosin along actin filaments.

The myosin superfamily contains over 30 classes, the largest of which is class II, also considered the conventional myosins (Brito & Sousa, 2020). It is essential for the contraction that is best described in skeletal muscle cells where actin and myosin arrange into highly ordered contractile units called sarcomeres (Figure 3A; Sweeney & Hammers, 2018).

In non-muscle cells the respective counterpart for exerting contractile forces is non-muscle myosin II (NMII). It consists of a heavy chain (MHC) that harbors a catalytic  $Mg^{2+}$ -ATPase, an ABS at its highly conserved N-terminus called head or motor domain and a long more variable C-terminal tail that facilitates dimerization through a coiled-coil domain (Figure 4A). Between the head and the tail of the MHC is a neck region that serves as a lever arm, amplifying even small conformational changes within the motor domain into movement at the distal end of the protein (Geeves et al., 2005). The neck also connects to a regulatory and an essential light chain (MRLC and MELC, respectively) (Brito & Sousa, 2020; Vicente-Manzanares et al., 2009). In an inactive state the motor and tail region interact, folding the protein dimer to a compact conformation, disallowing actin binding (Figure 4B). Upon phosphorylation of the MRLC at S19, the head domain is released changing the conformation of the protein to a linear state, increasing the ATPase activity but not the affinity to actin (Vicente-Manzanares et al., 2009). Once activated, ATP is hydrolyzed at the head and thereby its chemical energy converted to mechanical force moving the myosin head. Activated NMII dimers assemble into bipolar mini-filaments through interaction of the coiled-coil domains. Due to their

simultaneous actin binding, NMII filaments cross-link F-actin pulling the filaments together (Svitkina, 2018).

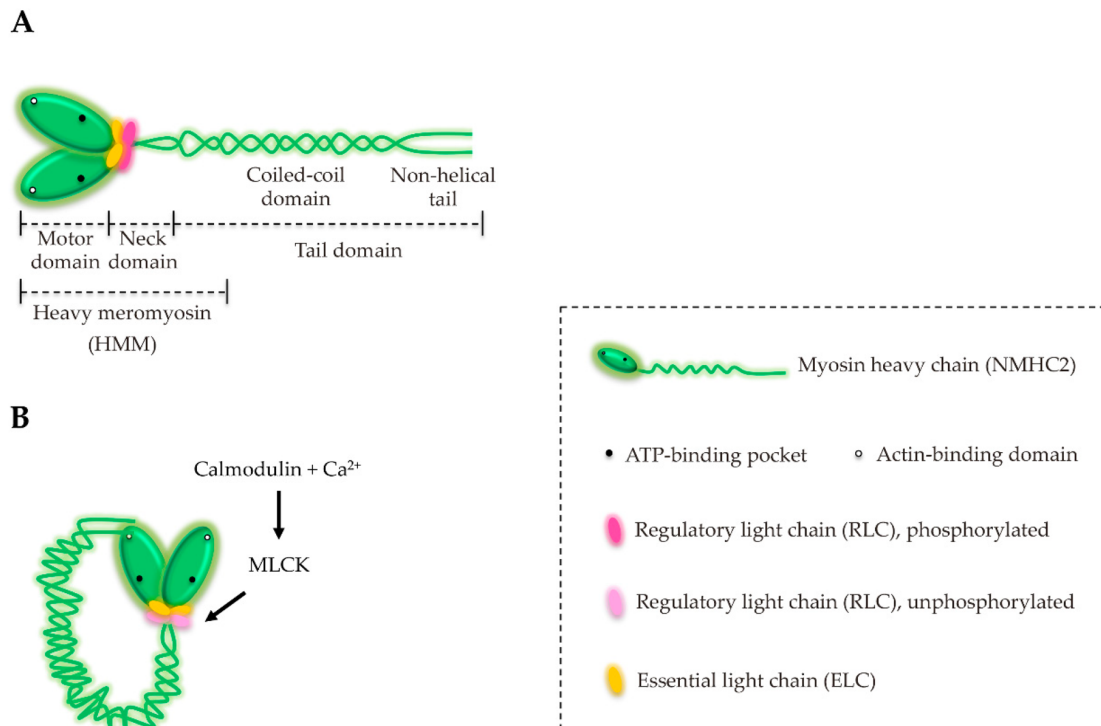


**Figure 4 – The structure of non-muscle myosin II from Brito & Sousa (2020).** (A) Myosin is composed of a heavy and two light chains (regulatory and essential). Domains of the heavy chain are indicated. Heavy meromyosin is a fragment that maintains structure and biochemical properties of the full-length protein. (B) Inactive myosin folds by interaction of the motor and tail domain. Upon phosphorylation of the regulatory light chain at S19 by MLCK (or ROCK) this autoinhibition is released. Reprint licensed under Creative Commons Attribution License.

The aforementioned necessary phosphorylation to activate NMII can be achieved through several known kinases (Vicente-Manzanares et al., 2009). Most notably are the myosin light chain kinase (MLCK) that is calmodulin-dependent, hence activated by  $\text{Ca}^{2+}$ , and the Rho-associated kinase (ROCK) which is downstream of the GTPase RhoA (Brito & Sousa, 2020). ROCK can also phosphorylate the myosin light chain phosphatase (MLCP) rendering it inactive to inhibit NMII (Schwayer et al., 2016). Interestingly, in some cells MLCK and ROCK display different localization patterns. While MLCK localizes in the periphery where the cytoskeleton is constantly rearranged in response to stimuli, ROCK is mostly found in the cell center where more stable structures such as stress fibers and mature focal adhesions are present (Totsukawa et al., 2004; Vicente-Manzanares et al., 2009). Therefore, NMII can be locally regulated resulting in distinct functions of actomyosin contraction in the cell.

Importantly, to generate directed forces, the actomyosin network needs traction. Therefore, it is anchored at either cell-matrix (e.g. focal adhesions) or cell-cell junctions (e.g. adherens junctions) (Agarwal & Zaidel-Bar, 2019; Brito & Sousa, 2020). Concomitantly, the maturation of focal adhesions from nascent adhesions in the lamellipodium depend on the tension generated by actomyosin contraction (Heuzé et al., 2019; Vicente-Manzanares et al., 2009).

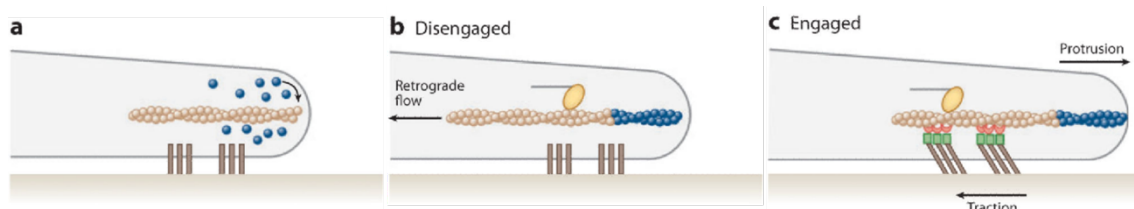


**Figure 5 – Scheme of the molecular clutch at the leading edge of a migrating cell from Gardel et al. (2010).** (a) F-actin polymerization at the leading edge is shown. The blue spheres represent actin monomers and the dark brown bars transmembrane integrins. (b) A disengaged clutch drives the actin filament to the cell center in retrograde flow. A myosin motor protein is depicted in yellow increasing the rearward motion. (c) Engagement of the clutch immobilizes the F-actin limiting retrograde flow and transmitting the contractile forces through the adhesion into traction on the extracellular matrix (ECM). Therefore, the cell cortex is pushed forward in a protrusion. Republished with permission of Annual Reviews, Inc.; permission conveyed through Copyright Clearance Center, Inc.

Although protrusion dynamics of migrating cells are predominantly regulated by actin polymerization, there is a link between protrusion, actin retrograde flow and adhesion which is influenced by NMII activity termed the molecular clutch hypothesis (Figure 5). The clutch are adhesion sites linking the F-actin network to the extracellular matrix (ECM). If the clutch is disengaged, actin polymerization at the barbed end and myosin contraction along the actin filament push F-actin rearward to the cell center in retrograde flow. An engaged clutch, however, immobilizes the F-actin, therefore the contractile forces are transmitted to the ECM as traction and the leading edge protrudes, moving the cell forward (Gardel et al., 2010; Z. Sun et al., 2016; Vicente-Manzanares et al., 2007). Importantly, adhesions activate a feed-back loop initiated by increased tension. Hereby, Rho GTPases are activated and consequently also NMII activity increases, resulting in stability and maturation of focal adhesions (Vicente-Manzanares et al., 2007).

### 1.7 *Drosophila* as model organism to study wound closure

As described above, at the single cell level contractile forces of actomyosin and synergy of actin bundling proteins are important for cell motility. At a multi-cellular level, coordination of migration and force generation are necessary for tissue remodeling

(Schwayer et al., 2016). These remodeling processes are important for development and also coping with tissue damage. The underlying molecular mechanisms are conserved processes (Belacortu & Paricio, 2011). Therefore, even the fruit fly is a powerful model organism to study tissue remodeling and repair.

One such well-studied developmental process is *Drosophila* dorsal closure which is mechanistically similar to closing of an epithelial wound (Figure 6). The embryo is covered on its dorsal side by the amnioserosa. This is an extra-embryonic sheet of cells which bridges the gap in the epidermis after germ band retraction. Dorsal closure is the process of the epidermal cells closing this gap by moving over and displacing the amnioserosa (Jacinto et al., 2001). The cells of the amnioserosa display NMII-dependent pulsatile contractions providing the main pulling forces to move the lateral epidermis cells together. At the same time, a supracellular actomyosin cable at the leading edge of the epidermis cells surrounding the tissue hole aids to pull the cells further together. This purse-string mechanism is also important to restrain the cells and ensure a uniform movement. The contractile ring is mainly composed of F-actin, myosin and  $\alpha$ -actinin, is regulated by the Rho GTPase RhoA and anchored intracellularly to adherens junctions (Schwayer et al., 2016; Wood et al., 2002). Upon contact of opposing cell fronts, Cdc42-dependent filopodia protrusions are necessary for the final zippering of the tissue (Jacinto et al., 2001; Wood et al., 2002). Although this morphogenetic movement is not an active migration of the epidermis cells, dorsal closure exhibits high similarities to single cell and multicellular tissue wounding.

During early stages of development, *Drosophila* embryos form a syncytium and can therefore be viewed, in a simplified manner, as a single multinucleated cell. Wounding the plasma membrane of these embryos (Figure 6) by laser ablation leads to a repair process that can be summarized in three phases: expansion, contraction and final closure of the wound (Abreu-Blanco et al., 2011). Like in dorsal closure, the contraction relies on a contractile actomyosin ring which, nevertheless, is dispensable for successful closure. *RhoA* mutant embryos cannot assemble the actomyosin cable at the wound edge but still close, though slower, through filopodia protrusions. In contrast to dorsal closure, the leading edge moves actively to regain cellular integrity. To assemble the protrusions there needs to be a directed actin cortical flow to supply G-actin to the wound edge. This actin recruitment is Rac dependent. Likely, there is a cross-talk of the Rho GTPases because each display a distinct localization pattern around the wound (Abreu-Blanco et al., 2014). Interestingly, also Rho guanine nucleotide exchange factors (GEF) that

activate Rho GTPases by exchanging bound GDP to GTP (Ridley et al., 2003), localize in a specific pattern around the wound. This suggests a role for the spatial regulation of Rho GTPase activation (Nakamura et al., 2017). Taken together, this results in two “actin zones” around the wound: one at the wound margin that is highly contractile and enriched with NMII and a second distal to the first, with low contractility where actin can assemble (Abreu-Blanco et al., 2014).

Lastly, multicellular wounding of embryonic and post-embryonic epidermis (Figure 6) has also been subject of many studies in *Drosophila*. It resembles more the wounding of adult mammalian tissues as it also triggers an immune response. Upon wounding, *Drosophila* macrophages from the circulating hemolymph are recruited to the wound site to phagocytose cell debris and potentially invading pathogens (Razzell et al., 2011). Like in dorsal closure and syncytial embryo wounding, the purse-string mechanism of an actin cable surrounding the wound does not play a major role in this wound closure model. Rather the directed cell migration of the epidermis cells across the wounded area using the cell debris as substrate, is important for re-epithelialization (Razzell et al., 2011; Wu et al., 2009). But not only the cells adjacent to the wound margin, also cells more distal can migrate actively to close the wound (Baek et al., 2010; Belacortu & Paricio, 2011; Y. C. Kwon et al., 2010; Lesch et al., 2010). However, how and when a wound is induced in the epidermal sheet triggers slightly different migratory responses.

In the larval epidermis pinch-wounded by forceps, cells move into the wound by forming broad lamellipodia which is therefore Arp2/3-complex-dependent. It also requires the active Rho GTPases Rac and Cdc42 but not RhoA (Lesch et al., 2010). It was shown that NMII is recruited to the rear end of more distal cells in the pinch-wounded epithelial sheet (S. H. Park et al., 2018). This re-localization is dependent on active c-Jun N-terminal kinase (JNK), a downstream effector of Rho GTPases (Y. C. Kwon et al., 2010; Lesch et al., 2010). This shows, in multicellular tissue wounding, Rho GTPases are also required for the polarization and thus directional sensing of a wound (Baek et al., 2010).

Different to pinch wounds, it was shown that laser-induced wounding of pupal notum epidermis is dependent on ROCK which is a downstream target of RhoA, but not Arp2/3-complex-mediated actin polymerization. Again, an actomyosin ring is established that acts in cooperation with lamellipodia and filopodia protrusions to close the wound. The initial wounding was also shown to cause an intracellular increase of  $Ca^{2+}$  activating the actin severing protein gelsolin. This provides G-actin and barbed ends for formin-mediated actin polymerization (Antunes et al., 2013).

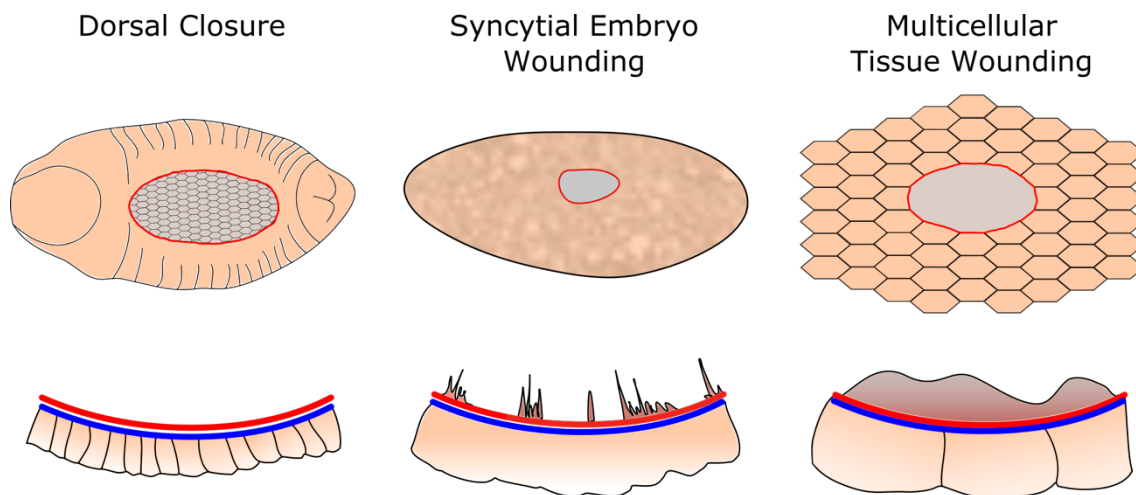


**Figure 6 – Scheme of different *Drosophila* wound closure models.** *Top panel* from left to right shows schemes of dorsal closure, single cell wounding of a syncytial embryo and multicellular wounding in the embryonic or post-embryonic epidermis. Depicted in grey is the extra-embryonic amnioserosa (dorsal closure) or the wound sites. **Bottom panel** shows the mode of closure. Contractile actomyosin rings at the wound edge are depicted as red and blue bands. Dorsal closure (left) is mainly dependent on actomyosin contraction. Syncytial embryo and embryonic/post-embryonic epidermis cells (middle/right) additionally show active filopodia-based movement at the wound leading edge. However, in a tissue context, cells at the edge of epidermis wounds (right) show lamellipodia more frequently.

Taken together, there is some diversity in how wounds are closed in different tissue contexts (Gurtner et al., 2008) and seemingly also a difference of the response in respect to wound size (Y. C. Kwon et al., 2010; Nakamura et al., 2018). For example, in laser-induced wounding of pupal epidermis it was shown that the magnitude of the  $\text{Ca}^{2+}$  influx seems to correlate with the wound size. The bigger the induced wound, the greater is the  $\text{Ca}^{2+}$  influx and signal propagation within the tissue (Antunes et al., 2013). Increase of the cytoplasmic  $\text{Ca}^{2+}$  concentration in the cells surrounding a wound site is one of the most important fast, transcription-independent signals to trigger the inflammatory response and wound healing process (Razzell et al., 2013).

## 1.8 Calcium is a regulator for actin dynamics

$\text{Ca}^{2+}$  is a second messenger, whose change in concentration induces and controls spatiotemporally pathways of many physiological processes such as proliferation or cell death and many processes dependent on cell migration such as development, immune response or cancer metastases (Clapham, 2007; Evans & Falke, 2007; Tsai et al., 2015). Therefore, the concentration of  $\text{Ca}^{2+}$  ions in cells must be tightly controlled. For the effectiveness of  $\text{Ca}^{2+}$  flux into the cytoplasm, an approximately 20.000-fold gradient

between intracellular and extracellular  $\text{Ca}^{2+}$  concentration must be maintained (Clapham, 2007). Special pumps like the plasma membrane  $\text{Ca}^{2+}$  ATPases (PMCA) or the sarcoendoplasmic reticular  $\text{Ca}^{2+}$  ATPases (SERCA) constantly remove  $\text{Ca}^{2+}$  ions under energy expenditure from the cytoplasm to the extracellular space or the endoplasmic reticulum (ER) that acts as the cell's  $\text{Ca}^{2+}$  storage (Clapham, 2007).

In migrating cells there is a tightly controlled gradient of  $\text{Ca}^{2+}$  from low at the leading edge to high at the cell rear (Tsai et al., 2015). The low background level at the front of the cell permits even small changes in  $\text{Ca}^{2+}$  concentration to relay signals efficiently (Brundage et al., 1991; Wei et al., 2009). Furthermore, tissue damage in a continuous epithelial sheet will cause an efflux of  $\text{Ca}^{2+}$  ions from the damaged cells into the extracellular environment which are rapidly transported by mechanosensitive ion channels into the cells surrounding the wound site (Nakamura et al., 2018). This signal is then propagated by gap junctions to neighboring cells (Razzell et al., 2013). The immediate increase of intracellular  $\text{Ca}^{2+}$  concentration leads to massive cytoskeletal remodeling, resulting in contractile ring and protrusion formation at the wound margin (Antunes et al., 2013).

Notably,  $\text{Ca}^{2+}$  activates actin severing proteins like gelsolin to remodel the actin cytoskeleton; it inhibits actin cross-linkers like  $\alpha$ -actinin thus relaxing the F-actin network in the lamellipodia; it activates NMII through activation of MLCK and, lastly, also establishes the Rho GTPase activity zones around a wound therefore affecting Rho GTPase effectors like ROCK and JNK (Antunes et al., 2013; Cordeiro & Jacinto, 2013; Dekraker et al., 2018; Schwyayer et al., 2016; Tsai et al., 2015). But for the initiation of these signaling cascades, the transient  $\text{Ca}^{2+}$  signal first needs to be deciphered by  $\text{Ca}^{2+}$  sensor proteins.

Calmodulin is such a highly conserved  $\text{Ca}^{2+}$  sensor protein. Upon  $\text{Ca}^{2+}$  binding to its EF-hand domains, calmodulin interacts and activates target proteins (Chin & Means, 2000; Nakayama & Kretsinger, 1994). There is a plethora of proteins which have calmodulin binding sites such as above mentioned MLCK. Likewise, there are many EF-hand domain or calmodulin-like domain containing proteins such as  $\alpha$ -actinin that can directly bind  $\text{Ca}^{2+}$  and induce specific  $\text{Ca}^{2+}$ -dependent processes. On such well-studied process is muscle contraction.

In striated muscles, actomyosin contraction is regulated by the actin-binding troponin-tropomyosin complex. This complex can inhibit contraction at low  $\text{Ca}^{2+}$  concentrations causing muscle relaxation (Chalovich et al., 1981). The EF-hand containing troponin-C



subunit binds  $\text{Ca}^{2+}$ , which leads to a conformational change in the inhibitory troponin-I subunit that is also bound to actin. This results in the release of tropomyosin blocking the binding of the myosin head to actin. Their strong binding then allows hydrolyzation of ATP and therefore contraction (Sweeney & Hammers, 2018).

This shows,  $\text{Ca}^{2+}$  is crucial for dynamic actin rearrangements necessary for many vital processes like muscle contraction, migration and wound closure. Therefore, the study of  $\text{Ca}^{2+}$  binding proteins in the context of actin cytoskeleton regulation is detrimental for our understanding of how these processes are controlled.

### **1.9 Swiprosin-1/EFHD2 is a calcium- and F-actin-binding protein**

Swiprosin-1/EFHD2 is a highly conserved actin binding protein that contains two EF-hand domains. However, its precise function and regulation are still unknown. Most studies so far have analyzed the human homolog, hereinafter referred to as EFHD2.

EFHD2 is evolutionary and structurally closely related to EFHD1 (Figure 7) but both differ in their site of expression and therefore also their function (Dütting et al., 2011). While EFHD1 is expressed in mitochondria (Dütting et al., 2011), EFHD2 is found in several tissues with high expression in the central nervous system and cells of the innate and adaptive immune systems (Avramidou et al., 2007; Vuadens et al., 2004).

The protein structure of EFHD2 (Figure 7) is a disordered region at the N-terminus that varies across species (Avramidou et al., 2007; Ferrer-Acosta et al., 2013; Hagen et al., 2012), two functional EF-hand domains, a connecting short  $\alpha$ -helix called ligand mimic (LM) helix and a coiled-coil (CC-) domain at its C-terminus allowing self-dimerization. EFHD2 has been shown to directly bind F-actin (Huh et al., 2013; M.-S. Kwon et al., 2013; Tu et al., 2018) and three binding regions have been suggested (M.-S. Kwon et al., 2013; K. R. Park et al., 2016). Most probable, an ABS is located within the first EF-hand domain because deletion of it has been shown to sufficiently diminish F-actin binding (Moreno-Layseca et al., 2021).

Through parallel self-dimerization of the CC-domain, EFHD2 has been shown to bundle F-actin (M.-S. Kwon et al., 2013; K. R. Park et al., 2016). This bundling activity is  $\text{Ca}^{2+}$ -dependent (M.-S. Kwon et al., 2013), believed that upon depletion of  $\text{Ca}^{2+}$  the local conformation at the EF-hand domains and LM helix becomes more flexible thereby reducing the bundling activity (K. R. Park et al., 2016). Binding of  $\text{Ca}^{2+}$  ions at the two EF-hands (Vega et al., 2008), however, was found to not alter the overall secondary structure nor the actin-binding properties of the protein (Ferrer-Acosta et al., 2013).

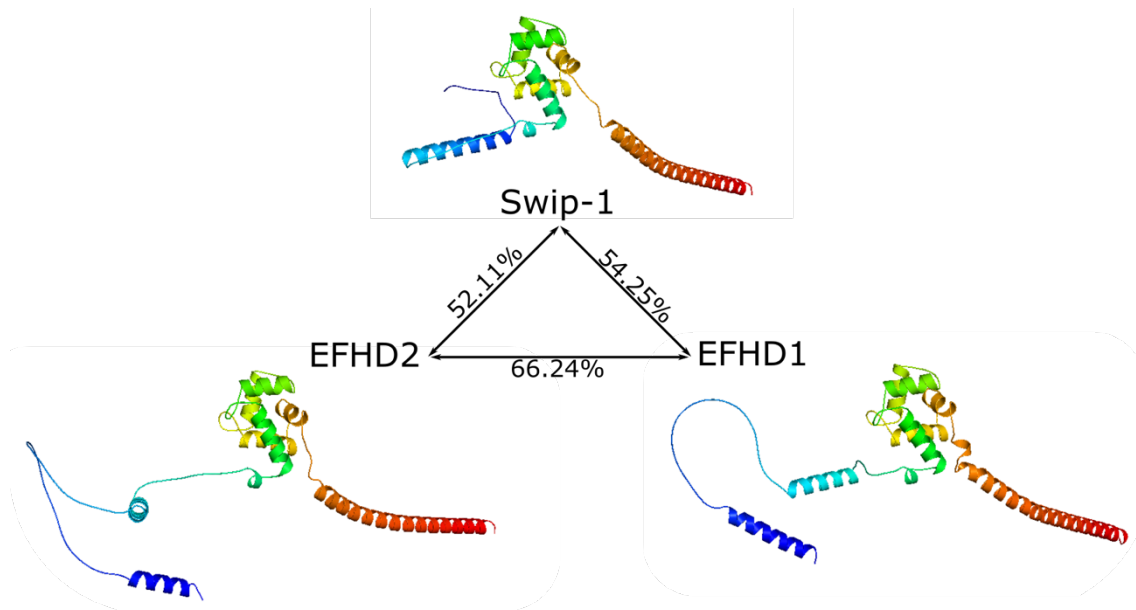


**Figure 7 – Comparison of *Drosophila* Swip-1, human EFHD2 and human EFHD1.** Each protein is represented with the predicted structure by AlphaFold (DeepMind & EMBL). Structures are shown in a color spectrum with the N-terminus depicted in blue, EF-hands in green and yellow, LM in orange, CC in red. Percent identity matrix of all three proteins by alignment of the amino acid sequences created by Clustal 2.1 (Waterhouse et al., 2009). Values as shown on arrows connecting the respective proteins. Accession numbers for structure and amino acid sequence: Q9VJ26 (EFHD2\_DROME), Q96C19 (EFHD2\_HUMAN) and Q9BUP0 (EFHD1\_HUMAN).

Overexpressed GFP-tagged EFHD2 in Chinese hamster ovary (CHO)-K1 cell line has been shown to localize in the lamellipodium. Overexpression variants lacking either the EF-hands or the CC-domain displayed mostly cytoplasmic localization and led to a disrupted lamellipodia formation and less cell spreading (M.-S. Kwon et al., 2013). Concurrently, in B16F10 melanoma cells, overexpression of EFHD2 led to increased lamellipodia formation and membrane ruffles (Huh et al., 2013, 2015).

Physiologically, EFHD2 has been associated with a plethora of pathologies such as Alzheimer's disease, schizophrenia, acute and chronic inflammation and cancer (Dütting et al., 2011; Mielenz & Gunn-Moore, 2016; Thylur et al., 2018). More precisely, it was found upregulated in various cancer cell lines and tissues, especially invasive stages of malignant melanoma. It has also been linked to tauopathies due to association to tau protein and enrichment in brain lysates of tauopathy model mice and human Alzheimer's disease brain (Vega et al., 2008). In the immature murine B-cell line WEHI231, it has been shown that ectopic overexpression of EFHD2 augmented spontaneous and B-cell receptor (BCR)-induced apoptosis (Avramidou et al., 2007). Moreover, EFHD2 deficiency led to a decreased production of cytokines resulting in increased sepsis-associated mortality due to immune deficiency (Zhang et al., 2018). It has further been implicated to modulate mast cell activation through actin regulation due to its high

concentration in microvilli-like membrane structures. This implied a potential role in forming signaling complexes in the plasma membrane dependent on actin reorganization (Ramesh et al., 2009).

Altogether, EFHD2 has been shown to be involved in cytoskeletal rearrangements and migration in different cell types and its overactivation can lead to respective diseases. However, how EFHD2 modulates the F-actin network in response to a  $\text{Ca}^{2+}$  stimulus in an *in vivo* model has not been addressed and is therefore still largely unknown.

### 1.10 Aim of this work

The present work aims to decipher the calcium-mediated changes of F-actin network organization through EFHD2 *in vivo* using *Drosophila melanogaster* as a model organism.

An advantage of *Drosophila* is that many genes and signaling pathways are conserved but it has less genetic redundancy than vertebrates (Belacortu & Paricio, 2011). EFHD2 in *Drosophila* is encoded by a single gene whose product is referred to as Swip-1. It has been previously shown that Swip-1 is highly expressed in embryonic macrophages (Hornbruch-Freitag et al., 2011). Further, survey of expression profiles showed high expression of Swip-1 in more tissues including the larval and adult central nervous system and salivary glands (Leader et al., 2018).

Migration of pupal *Drosophila* macrophages as well as the wound closure of larval epidermis are known calcium-regulated processes that both rely on lamellipodia protrusions. Because EFHD2 has been shown to play a role in lamellipodia formation, these processes will be further investigated *in vivo*. In order to reproducibly investigate wound closure, a novel single cell wounding model of the larval epidermis omitting forceps pinching is established. Knock out and rescue experiments shall shed light on Swip-1's function and the relevance of its  $\text{Ca}^{2+}$  binding and dimerization capabilities in each process.

Furthermore, it has been hypothesized that in *Drosophila* embryos Swip-1 regulates  $\text{Ca}^{2+}$ -dependent exocytosis of electron dense vesicles during myoblast fusion (Hornbruch-Freitag et al., 2011). Because of its high expression in salivary glands, a putative function of Swip-1 in the regulated exocytosis of glue granules will be examined.

Altogether, this may also allow to hypothesize about pathways and downstream effectors of Swip-1 and possible underlying mechanisms of Swip-1-linked pathologies.

## 2 Publications

### 2.1 Publication 1

Nature Communications 2022, 13(1), 2492.

Calcium bursts allow rapid reorganization of EFhD2/Swip-1 cross-linked actin networks in epithelial wound closure.




Franziska Lehne, Thomas Pokrant, Sabnam Parbin, Gabriela Salinas, Jörg Großhans, Katja Rust, Jan Faix & Sven Bogdan

## ARTICLE

<https://doi.org/10.1038/s41467-022-30167-0>

OPEN

# Calcium bursts allow rapid reorganization of EFhD2/Swip-1 cross-linked actin networks in epithelial wound closure

Franziska Lehne <sup>1</sup>, Thomas Pokrant<sup>2</sup>, Sabnam Parbin<sup>3</sup>, Gabriela Salinas<sup>3</sup>, Jörg Großhans<sup>4</sup>, Katja Rust<sup>1</sup>, Jan Faix <sup>2</sup> & Sven Bogdan <sup>1</sup>✉

Changes in cell morphology require the dynamic remodeling of the actin cytoskeleton. Calcium fluxes have been suggested as an important signal to rapidly relay information to the actin cytoskeleton, but the underlying mechanisms remain poorly understood. Here, we identify the EF-hand domain containing protein EFhD2/Swip-1 as a conserved lamellipodial protein strongly upregulated in *Drosophila* macrophages at the onset of metamorphosis when macrophage behavior shifts from quiescent to migratory state. Loss- and gain-of-function analysis confirm a critical function of EFhD2/Swip-1 in lamellipodial cell migration in fly and mouse melanoma cells. Contrary to previous assumptions, TIRF-analyses unambiguously demonstrate that EFhD2/Swip-1 proteins efficiently cross-link actin filaments in a calcium-dependent manner. Using a single-cell wounding model, we show that EFhD2/Swip-1 promotes wound closure in a calcium-dependent manner. Mechanistically, our data suggest that transient calcium bursts reduce EFhD2/Swip-1 cross-linking activity and thereby promote rapid reorganization of existing actin networks to drive epithelial wound closure.

<sup>1</sup>Institute of Physiology and Pathophysiology, Department of Molecular Cell Physiology, Philipps-University Marburg, Marburg, Germany. <sup>2</sup>Institute for Biophysical Chemistry, Hannover Medical School, Hannover, Germany. <sup>3</sup>NGS-Integrative Genomics Core Unit, Department of Human Genetics, University Medical Center Göttingen, Göttingen, Germany. <sup>4</sup>Department of Biology, Philipps-University Marburg, Marburg, Germany. ✉email: [sven.bogdan@staff.uni-marburg.de](mailto:sven.bogdan@staff.uni-marburg.de)

The actin cytoskeleton provides the mechanical forces driving cell shape changes and cell migration<sup>1</sup>. Cells have evolved more than 60 families of actin-binding proteins (ABPs) that maintain the pool of actin monomers and promote actin nucleation, elongation, severing, and cross-linking of filaments<sup>2</sup>. At the leading edge of migrating cells (the so-called lamellipodium), a dense network of actin filaments is nucleated and organized in branched arrays by the Arp2/3 complex, which is activated by nucleation-promoting factors<sup>3</sup> such as WASP and WAVE proteins<sup>3–7</sup>. Arp2/3-mediated actin polymerization is referred to as dendritic nucleation by which branched actin networks generate actin pushing forces against the membrane surface<sup>8</sup>. Force generation in lamellipodia further depends on FMNL 2/3 formins and Ena/VASP family actin polymerases<sup>7–9</sup>.

3D-electron tomography analysis further suggested an additional important role of cross-linking proteins as mechanical elements that stabilize the actin network in the lamellipodium<sup>10–12</sup>. In response to mechanical or biochemical cues, dynamic changes in cross-linked filaments might further allow the migrating cell to rapidly alter its mechanics by converting highly cross-linked, elastic networks into weakly cross-linked, viscous networks<sup>13</sup>. Different classes of actin-binding proteins such as filamin, plastins,  $\alpha$ -actinin, or fascin present in Arp2/3-dependent lamellipodia contribute to the stabilization of lamellipodium architecture and embedded actin bundles<sup>14–21</sup>. These proteins frequently exhibit a dual activity by either cross-linking filaments into loose networks or laterally into tight bundles of filaments in vitro, often depending on protein concentration. In vivo, actin bundles might be preferentially induced by a short actin cross-linker, such as fascin, whereas long cross-linkers with a long spacer between the actin-binding sites, such as filamin, rather cross-link the actin networks<sup>2,22</sup>.

Some of these actin-binding proteins additionally contain calcium-binding EF-hands<sup>23,24</sup>. Although the role of calcium in regulating cell shape and cell migration has been long recognized, it remained largely elusive, how EF-hand domain-containing actin-binding proteins regulate protrusion dynamics and cell motility by reorganization of the actin cytoskeleton in a Ca<sup>2+</sup>-dependent manner<sup>24,25</sup>. The EF-hand domain-containing EFhD2/Swip-1 protein has been previously described as a prime candidate for controlling calcium-depending actin bundling in different tissues across species<sup>26–32</sup>. EFhD2/Swip-1 was found significantly upregulated in a number of pathological conditions of inflammation, immune response, and cancer suggesting an important role of EFhD2/Swip-1 in cell migration and cell adhesion during immune cell response and cancer invasion<sup>30,32–35</sup>.

Here we identify EFhD2/Swip-1 as a calcium-dependent actin cross-linker required for lamellipodial protrusions in cell migration and epithelial wound response. Our data mechanically explain how calcium bursts allow a rapid reorganization of existing actin networks to drive epithelial wound closure.

## Results

**Swip-1 is upregulated in activated *Drosophila* macrophages.** *Drosophila* macrophages undergo a remarkable shift from a quiescent sessile state to highly polarized migratory cells at the onset of metamorphosis<sup>36,37</sup>. Comparative RNA-seq gene expression analysis revealed 1542 differentially regulated genes, from which 804 genes are up-regulated in highly motile pupal macrophages compared to quiescent larval macrophages (Supplementary Fig. 1a). Among the top 50 cytoskeletal/motility candidates upregulated in pupal macrophages, we identified genes encoding known pro-migratory proteins such as FHOD1/Fhos<sup>38</sup>, different subunits of the Arp2/3 complex, and the WAVE

Regulatory Complex (WRC) as well as several actin filament-binding proteins including the EF-hand domain-containing Swip-1 protein (Supplementary Fig. 1b). We focused our attention on Swip-1, which was significantly enriched in prepupal macrophages with a fold change<sup>28</sup> of 2.46 (Supplementary Fig. 1b). In variance to mammalian cells, *Drosophila* only contains a single gene encoding Swip-1 (Supplementary Fig. 1c). The domain structure of *Drosophila* Swip-1 protein resembles its mammalian orthologs, EFhD1 (also termed Swip-2) and EFhD2 (also termed Swip-1) bearing two highly conserved EF-hands and a C-terminal coiled-coil domain (ref. <sup>39</sup> and Supplementary Fig. 1c).

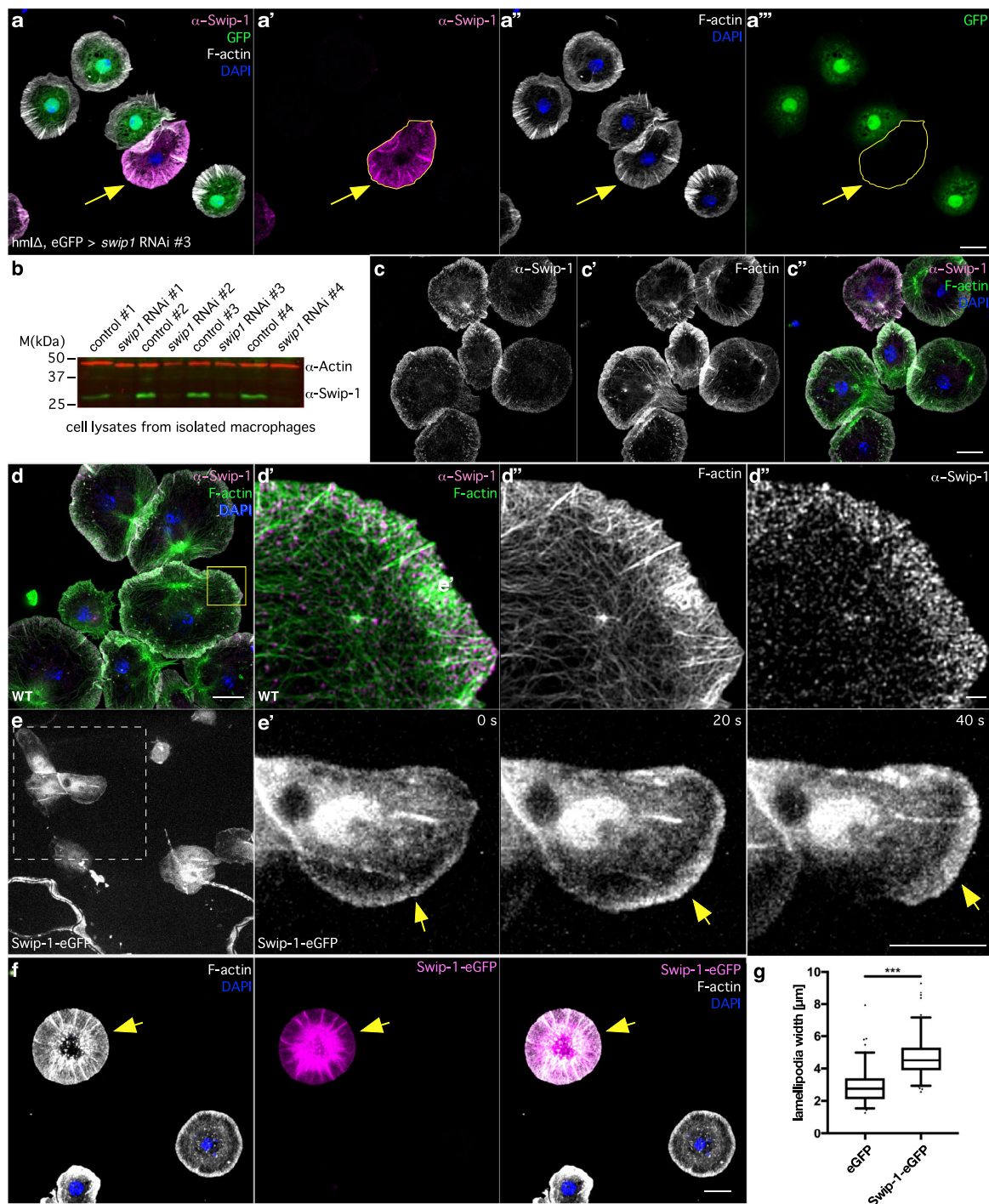
### Swip-1 localizes to protruding lamellipodia of macrophages.

Ectopically expressed human EFhD2 has been found to localize to lamellipodial protrusions in motile cultured cells<sup>30,40,41</sup>. Consistently, we found that endogenous Swip-1 is highly abundant in protruding lamellipodia of *Drosophila* macrophages (Fig. 1a, a', c). A complete loss of immunostaining in RNAi-depleted cells confirmed the high specificity of the anti-Swip-1 antibody (Fig. 1a', b). Swip-1 displayed a prominent colocalization with F-actin in the lamellipodia (Pearson's correlation coefficient:  $0.68 \pm 0.05$ ; Manders' colocalization coefficient: 85.3%). High-resolution structured illumination microscopy (SIM) analysis further revealed a striking localization of Swip-1 in a punctate pattern along actin filament bundles and cross-links (Fig. 1c, d). To visualize the dynamic localization of Swip-1 in protruding lamellipodia we generated transgenic flies expressing an eGFP-tagged protein. Spinning disk microscopy imaging of transgenic prepupae revealed a dynamic and broad localization of Swip-1-eGFP in protruding lamellipodia of crawling macrophages (Fig. 1e, e' and Supplementary Movie 1). A localization in lamellipodia was also found in macrophage-like *Drosophila* S2R+ cells<sup>42</sup>, transiently expressing eGFP-tagged Swip-1 (Fig. 1f). Interestingly, forced strong overexpression of Swip-1 even promoted lamellipodia formation as confirmed by quantification of increased lamellipodial width of transfected S2R+ cells compared to cells only transfected with eGFP control plasmids (Fig. 1g). Thus, Swip-1 localizes to protruding lamellipodia comparable to mammalian cells.

### Swip-1 promotes lamellipodia formation and controls macrophage migration.

Since overexpression of Swip-1 promoted lamellipodia formation, we next sought to analyze the consequences of loss of *swip-1* function, which has yet not been addressed in *Drosophila*. The *Drosophila swip-1* gene is located on the second chromosome corresponding to the cytological location 37B8 (Fig. 2a). It consists of two exons encoding a 25 kDa protein. We took advantage of CRISPR/Cas9-mediated genome editing to introduce small deletions within the first exon of the *swip-1* gene locus (Fig. 2a). We isolated several viable frame-shift mutants resulting in a complete loss of Swip-1 protein (Fig. 2a, b). Macrophages isolated from mutant pupae showed an impaired spread morphology with a reduced lamellipodia width and a reduced circularity compared to wild type (Fig. 2c, d; quantification in Fig. 2e, f). Re-expression of Swip-1 substantially rescued defects in the spread morphology of mutant macrophages (Fig. 2f, g).

Noticeable differences were also seen in the motility of mutant cells in vivo. Macrophages initiate random cell migration in the 3D environment of a 2–4 h old prepupae<sup>43</sup>. Remarkably, automatic tracking of individual migrating mutant cells revealed a significant increase in cell speed, displacement from origin, and straightness of movement (Fig. 2j, quantification in Fig. 2m, and Supplementary Fig. 2a, b). Control cells migrated with an average track speed mean of  $2.3 \pm 0.9 \mu\text{m}/\text{min}$  whereas *swip-1* mutant cells migrated considerably faster with an average track speed



mean of  $3.9 \pm 0.7 \mu\text{m}/\text{min}$  (Fig. 2m and Supplementary Movie 2). The increased migration speed of mutant cells was rescued by re-expressing Swip-1 (Fig. 2k and quantification in Fig. 2m). By contrast, the overexpression of the same Swip-1 transgene in a wild-type background resulted in subtle but significant reduced migration speed (Fig. 2i and quantification in Fig. 2m). Cells overexpressing Swip-1 formed enlarged but often depolarized lamellipodia protrusions, which is expected to reduce cell

migration speed (Supplementary Movie 2). Thus, these results highlight a conserved role of EFhd2/Swip-1 in lamellipodial protrusions and immune cell migration in vivo.

We next analyzed the functional relevance of calcium binding of Swip-1 in macrophage migration. Based on sequence alignment, *Drosophila* Swip-1 has two predicted EF-hand motifs, EF-loop 1, 82aa DTARDGFLDLQE 93aa (corresponding to human EFhd2 105-116aa), and EF-loop 2, 118aa DEDNDGKISFRE 129aa

**Fig. 1 Swip-1 localizes to protruding lamellipodia.** **a** Maximum intensity projection of confocal images of the actin cytoskeleton in prepupal macrophages expressing *swip-1* dsRNA marked by eGFP co-expression. Scale bars represent 10  $\mu\text{m}$ . Cells were co-stained with anti-Swip-1 antibody (magenta), DAPI (blue), and phalloidin (white). The arrow marks an eGFP-negative wild-type cell with high Swip-1 expression. **b** Western blot analysis of lysates of macrophages cells expressing different *swip-1* dsRNA transgenes as indicated under the control of the *hemolectin*-Gal4 driver. The expression of dsRNA transgenes without the Gal4 driver serves as a control. Knock-down efficiency was validated with an anti-Swip-1 specific antibody. Actin served as loading control. **c, d** Structured illumination microscopic (SIM) images of wild-type prepupal macrophages co-stained for endogenous Swip-1 (magenta), phalloidin (green) and DAPI (blue). Scale bars 10  $\mu\text{m}$ . **e** Frames of spinning disk microscopic video of a migrating macrophage expressing an Swip-1-eGFP fusion. The arrow marks the localization of Swip-1 in the protruding lamellipodium. Images were taken every 20 s for 30 min (see also Supplementary Movie 1). Scale bar 10  $\mu\text{m}$ . **f** Maximum intensity projection of the confocal image of S2R+ cells transfected with Swip-1-eGFP fusion (magenta), stained with DAPI (blue) and phalloidin (white). Scale bar 10  $\mu\text{m}$ . **g** Lamellipodia width of S2R+ cells either transfected with cytoplasmic eGFP or Swip-1-eGFP fusion was measured at five regions using Image J and averaged. Boxes indicate 50% (25–75%) and whiskers (5–95%) of all measurements, with black lines depicting the medians.  $n = \text{eGFP WT: } 20, \text{ Swip-1-eGFP: } 21$  cells each from one representative transfection. Two-sided Mann-Whitney test was used,  $P$  value:  $<0.001$  (\*\*\*)). All images shown are representative of at least three independent experiments.

(corresponding to human EFhD2 141–152aa). Mutations in the first highly conserved aspartate residues of both EF-loops (D82A/D118A; Supplementary Fig. S1c, marked by red boxes) have been shown to abolish calcium-binding capacity<sup>29,44</sup>. Interestingly, re-expression of such mutant Swip-1-D82A/D118A transgene failed to rescue migration defects of *swip-1*-deficient macrophages (Fig. 2I). Remarkably, Swip-1-D82A/D118A mutant protein was no longer enriched in actively protruding lamellipodia, but rather re-localized to the cell cortex suggesting that calcium or full activity might be critical for lamellipodial localization of Swip-1 (Fig. 2n and Supplementary Movie 3). Moreover, mutant macrophages re-expressing Swip-1-D82A/D118A often attached together and formed clusters (Fig. 2n). Cell cluster formation was also prominent in isolated mutant macrophages re-expressing Swip-1-D82A/D118A plated on surfaces coated with the ECM protein vitronectin and correlated with an increased  $\beta$ -integrin accumulation at cell-cell contacts (Supplementary Fig. 2d). Compared to wild type, mutant cells showed an enhanced spreading and exhibited increased  $\beta$ -integrin-marked focal adhesion sites along the leading edge (Supplementary Fig. 2e, f) suggesting a possible conserved role of Swip-1 in regulating integrin adhesion dynamics as recently reported in human breast cancer cell line<sup>32</sup>.

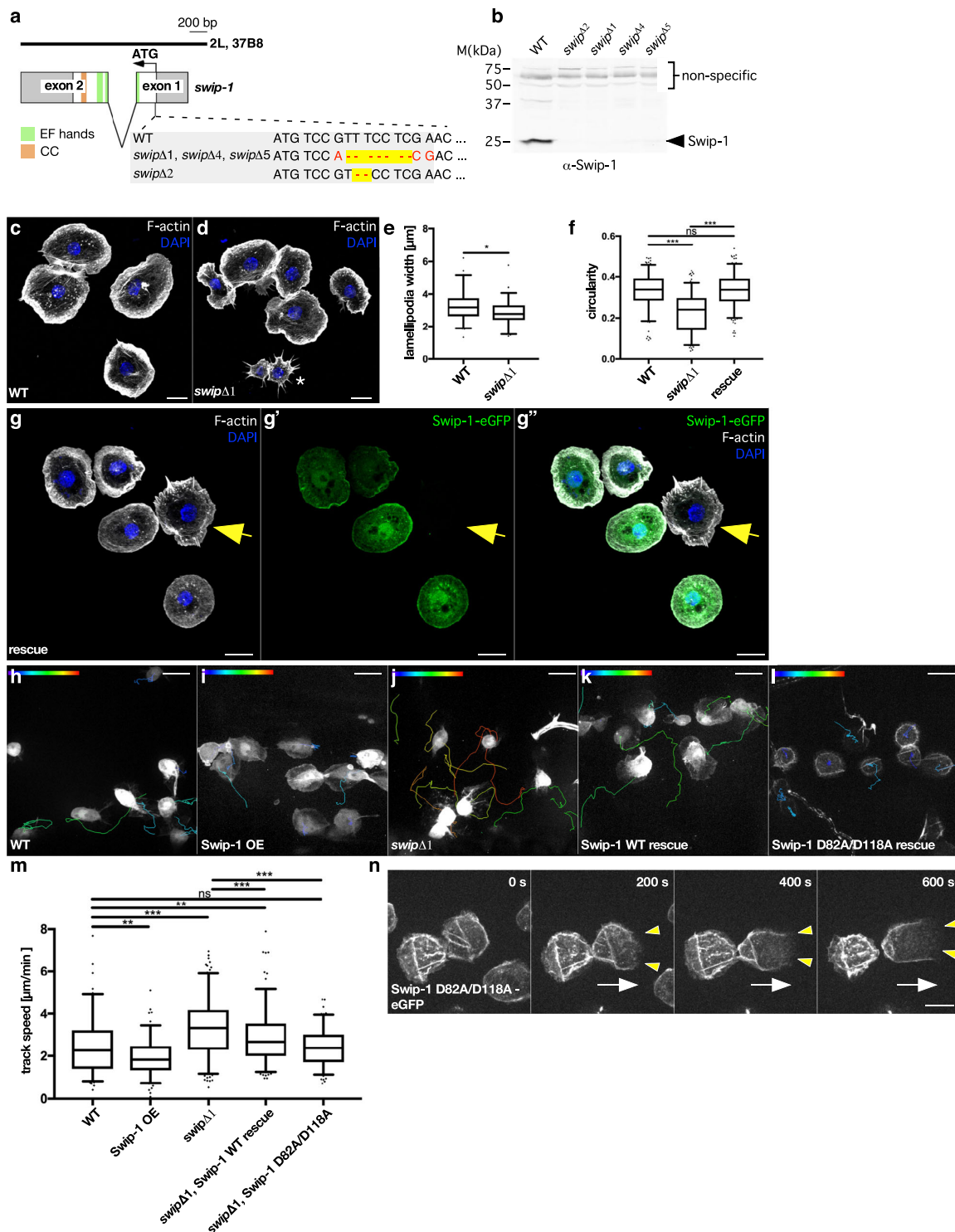
**Calcium promotes transient F-actin cross-links by EFhD2/Swip-1.** We reasoned that impaired lamellipodia formation in *swip-1* mutant cells could reflect a direct effect of Swip-1 on the structure of the actin cytoskeleton network. Published work suggested that human EFhD2 induces actin bundling in the presence of calcium. This notwithstanding, in this study very high and thus rather non-physiological concentrations of recombinant human EFhD2 protein (up to 15  $\mu\text{M}$ ) have been used in in vitro co-sedimentation assays<sup>30</sup>. Moreover, previous binding assays were performed with GST-tagged fusion proteins that noticeably increased F-actin bundling activity of EFhD2<sup>30</sup>. Thus, we first determined the cellular concentration of endogenous Swip-1 in *Drosophila* cells by titrating defined amounts of recombinant protein with total cell lysates from *Drosophila* S2 and S2R+ cells in immunoblots. From densitometric intensities, we calculated a cytoplasmic concentration of Swip-1 of about 0.3  $\mu\text{M}$ . We next tested the actin-binding activity of purified recombinant Swip-1 protein in vitro. To exclude artificial oligomerization by the GST moiety, we removed the tag by proteolytic cleavage followed by a final polishing step of the Swip-1 protein. Then, we used high-speed sedimentation to determine the affinity and stoichiometry of Swip-1 to actin (Fig. 3a–d). In the absence of calcium, Swip-1 bound to F-actin with an estimated  $K_D$  of  $4.3 \pm 1.3 \mu\text{M}$  with a  $\sim 1:1$  (Swip-1: actin) stoichiometry at saturation (Fig. 3a, b). Remarkably, in the presence of calcium, the binding affinity of Swip-1 to F-actin increased approximately five-fold ( $K_D$  of

$0.9 \pm 0.1 \mu\text{M}$ ; Fig. 3c, d). Interestingly, however, the binding stoichiometry changed to  $\sim 0.5:1$  (Swip-1: actin) in the presence of calcium supporting the notion that Swip-1 undergoes conformational changes upon  $\text{Ca}^{2+}$  binding<sup>45</sup>. Furthermore, we found in low-speed pelleting assays that in the absence of calcium Swip-1 significantly increased the amount of bundled/cross-linked actin filaments compared to low-speed pelleting assays in the presence of 1 mM  $\text{Ca}^{2+}$  (Fig. 3e, f and quantification in Fig. 3g).

To explore the effect of Swip-1 on actin filament architecture in more detail, we performed total internal reflection fluorescence (TIRF) microscopy that allows direct visualization of the assembly of single actin filaments and higher-order structures in real time<sup>46</sup>. We first compared actin assembly in the presence of either *Drosophila* Swip-1, human EFhD2, human  $\alpha$ -actinin4, or human fascin in the absence of calcium to assess the general behavior of the proteins in vitro (Supplementary Movie 4). In contrast to human proteins, which induced the formation of prominent bundles at 0.5  $\mu\text{M}$  concentrations, we could not observe any formation of actin bundles in the presence of 1.0  $\mu\text{M}$  Swip-1 (Supplementary Movie 5). Rather, under all tested conditions ranging from 0.1–1.0  $\mu\text{M}$  Swip-1 induced exclusively the formation of prominent actin cross-links in the absence of calcium (Fig. 3h and Supplementary Movie 5). Interestingly, we found that human EFhD2 protein exhibited a dual activity in vitro by preferentially cross-linking filaments into loose networks at lower concentration (100 nM) or laterally into loose bundles of filaments at higher concentration (1  $\mu\text{M}$ ). Notably, the bundling activity of human EFhD2 was calcium-insensitive but was dominated at higher protein concentrations (Supplementary Movie 6). In stark contrast, the actin filament cross-linking activity of *Drosophila* Swip-1 (Supplementary Movie 7) and human EFhD2 (Supplementary Movie 8) is regulated by calcium. Quantitative analysis of cross-link events revealed that in the absence of calcium even at 0.1  $\mu\text{M}$ , Swip-1 induced stable, perpendicular cross-links between elongating actin filaments, creating a stable and highly cross-linked network over time (Fig. 3h and Supplementary Movie 5). However, cross-links between actin filaments were rare or nearly absent in the presence of calcium at the low Swip-1 concentration of 0.1  $\mu\text{M}$ . At 1.0  $\mu\text{M}$  Swip-1, the cross-links were more frequent, but still highly dynamic and short-lived as assessed by quantification of attachment versus detachment events of cross-linked filaments from time-lapse TIRF movies (Fig. 3h, i and Supplementary Movie 7). Similarly, we observed that human EFhD2/Swip-1 frequently induced stable cross-links in the absence of calcium, while it only bundled actin filaments in the presence of calcium (Supplementary Movie 8).

To assess the functional relevance of calcium binding of Swip-1 on actin filament architecture in vitro, we purified a recombinant





calcium-binding deficient Swip-1 mutant protein D82A/D118A in which the highly conserved first coordinating aspartic acid of both EF-loops was replaced with an alanine. Subsequent TIRF analysis revealed that this mutant protein still induced stable, perpendicular cross-links, albeit in a calcium-independent manner (Supplementary Fig. 3 and Supplementary Movie 9).

Unexpectedly, however, this mutant Swip-1 protein additionally acquired prominent actin-bundling activity (Supplementary Movie 9), suggesting a conformational change in the protein, caused by the exchange of the two negatively charged aspartic acid residues with alanine. Notably, conformational changes in the EF-hand triggered by calcium binding have been previously

**Fig. 2 Loss of Swip-1 impairs lamellipodia formation and cell migration of macrophages.** **a** Schematic overview of the *swip-1* gene locus. Exons encoding parts of distinct domains are indicated, EF domains in green and coiled-coil region in orange. The target sequence for CRISPR/Cas9 gene modification and generated *swip-1* deletions are depicted. **b** Loss of *swip-1* mutants were validated by Western blot analysis. Lysates from ten fly heads of wild-type and different mutant flies were analyzed. Non-specific bands (upper bands) serve as a loading control. All obtained mutants were validated once, hereinafter used *swip-1* mutant flies were checked regularly in Western blot analysis of head lysates. **c, d** Confocal images of **c** wild-type and **d** *swip-1* mutant macrophages were co-stained with phalloidin (white) and DAPI (blue). Scale bars 10  $\mu\text{m}$ . **e** Quantification of lamellipodia width at the leading edge,  $n = \text{WT}: 64$ , *swip-1* mutant: 61 cells of two independent experiments ( $P$  value: 0.012). **f** Circularity was measured using Image J shape descriptors,  $n = \text{WT}: 180$ , mutant: 192 ( $P$  value:  $>0.001$ ), rescue: 209 cells ( $P$  value: 0.892). **g** Rescue of *swip-1* mutant macrophages re-expressing a Swip-1-eGFP fusion were co-stained with phalloidin (white) and DAPI (blue). The arrow marks mutant cells lacking Swip-1-eGFP that still show an irregular cell shape. **h, i** Spinning disk microscopy live imaging of randomly migrating macrophages in prepupae with indicated genotypes were tracked by using Imaris 9.3. Track speed mean is color-coded (0.06 to 6  $\mu\text{m}/\text{min}$ ) (**h**) wild type and (**i**) overexpression of a Swip-1-eGFP (OE) in a wild-type background, **j** *swip-1* mutant, (**k**) rescue with a Swip-1-eGFP, and **l** rescue with a Swip-1-D82A/D118A-eGFP, respectively. **m** Quantification of track speed mean, WT:  $n = 114$  tracks, OE:  $n = 133$  tracks ( $P$  value: 0.006), *swip-1* mutant:  $n = 206$  tracks ( $P$  value:  $<0.001$ ), rescue WT:  $n = 166$  tracks ( $P$  values: 0.002 to WT and  $<0.001$  to mutant), rescue Swip1D82A/D118A:  $n = 136$  tracks ( $P$  values: 0.594 to WT and  $<0.001$  to mutant). **e, f, m** Boxes indicate 50% (25–75%) and whiskers (5–95%) of all measurements, with black lines depicting the medians. For statistical analysis, two values indicated by connecting black lines were compared with two-sided Mann-Whitney test,  $P$  value: 0.12 (ns), 0.033 (\*), 0.002 (\*\*),  $<0.001$  (\*\*\*). **n** Frames of spinning disk microscopy video of migrating *swip-1* mutant macrophages re-expressing Swip-1-D82A/D118A-eGFP. Images were taken every 20 s for 30 min. A white arrow indicates the direction of movement; yellow arrowheads mark the lamellipodium. Swip-1-D82A/D118A-eGFP localizes to the cell cortex but not to the protruding lamellipodium (see also Supplementary Video M3). Scale bar 10  $\mu\text{m}$ . All images shown are representative of at least three independent experiments unless otherwise specified.

also shown to modulate F-actin binding in both human  $\alpha$ -actinin and EFhD2<sup>45,47</sup>. Taken together, our data uncover a calcium-regulated actin cross-linking activity of EFhD2/Swip-1, conserved between humans and flies, which might be relevant in diverse cellular processes depending on calcium-induced rapid reorganization of dynamic actin networks.

**Swip-1 localizes to lamellipodial protrusions in a calcium-dependent manner during epithelial wound closure.** To better understand the physiological relevance of Swip-1 function within a calcium-dependent *in vivo* tissue context, we established a single-cell wounding model system using larval epidermal cells (LECs) in the early pupal stages of *Drosophila* development. LECs are up to 70  $\mu\text{m}$  in diameter cells and form a polarized epithelial monolayer. During mid-metamorphosis LECs undergo apoptosis and are replaced by epidermal histoblast cells forming the new adult epidermal sheet<sup>48</sup>.

Spinning disk, live-cell imaging microscopy of the dorsal side of the abdomen of 18 h APF old pupae ubiquitously expressing a LifeAct-eGFP transgene revealed a tight epidermal sheet consisting of large polygonal epithelial cells (Fig. 4a, b). Epithelial cells showed an overall stationary cell behavior with only very small membrane protrusions formed along their cell–cell contacts (Fig. 4b; unwounded). This was dramatically changed upon laser-induced single-cell wounding. In the first minutes, F-actin assembled into broad lamellipodial protrusions within cells at the wound edge (front row; Fig. 4c and Supplementary Movie 10). Time-lapse movies further demonstrated that lamellipodial protrusions reached a maximum size between 5–10 min after wounding. Thereafter, lamellipodia formation decreased and coexisted with an increasing number of contractile actin bundles, which were formed at the leading edge of the wound, contracted laterally to pull cells forward, and increasingly contributed to wound closure (Fig. 4c and Supplementary Movie 10).

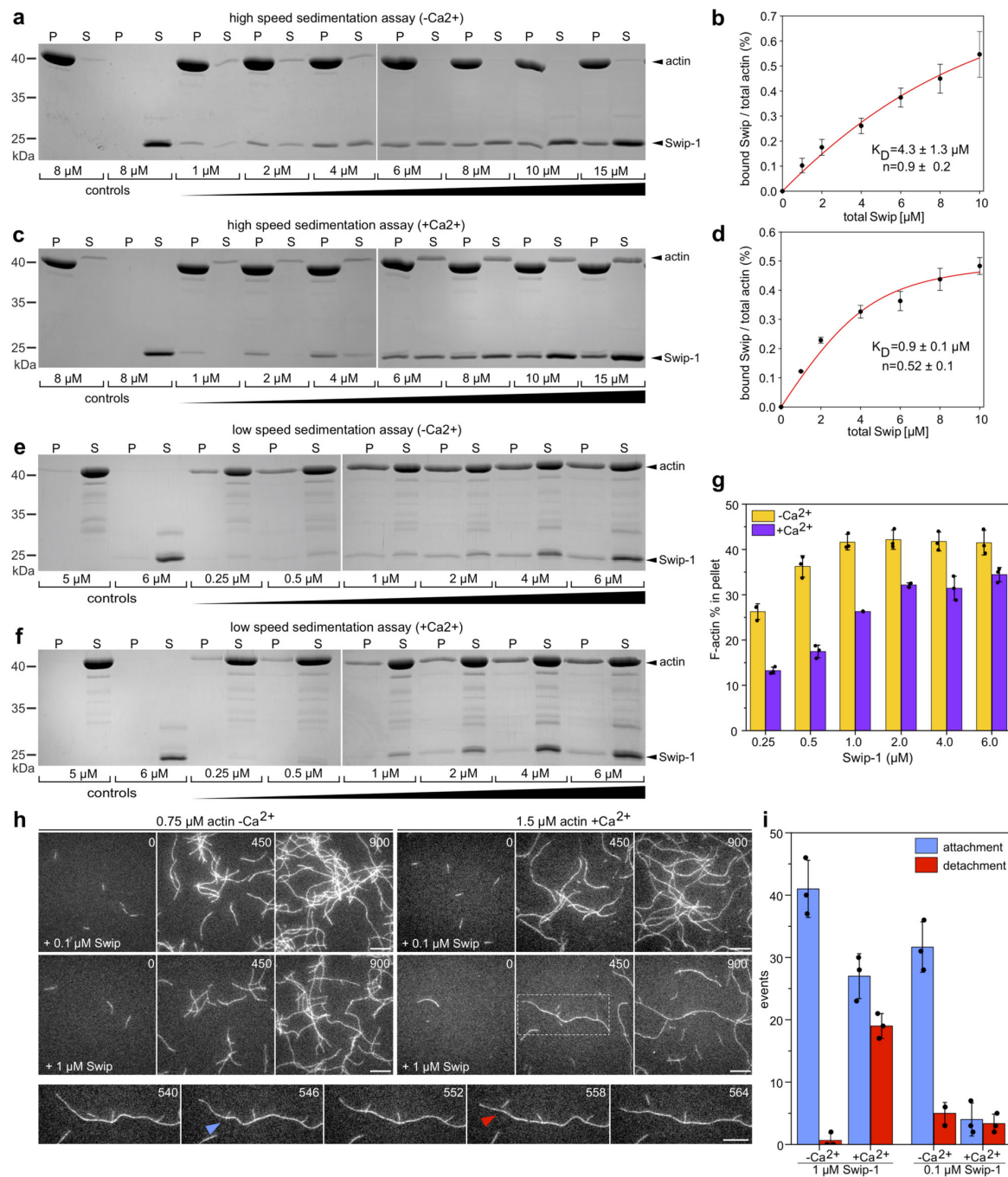
Imaging of a Swip-1-eGFP tagged transgene immediately after laser cell ablation revealed prominent recruitment of Swip-1 from the cell periphery into newly formed lamellipodial protrusions oriented towards the wound area (Fig. 4d and Supplementary Movie 11). Remarkably, we observed that after some time, even epithelial cells several rows back from the wound site exhibited a delayed response by extending lamellipodia marked by EFhD2/Swip-1-eGFP along intact cell–cell contacts (marked by white arrows in Fig. 4d and Supplementary Movie 11). This could also

be observed in epithelial wounds using the Lifeact-eGFP transgene (Supplementary Movie 10).

This suggests that the initial wound signal is transmitted to undamaged cells, possibly by a rapid influx of calcium into the cells as previously observed in embryonic and pupal wound models<sup>49,50</sup>. To test this hypothesis, we took advantage of an mRuby-based RCaMP1, a genetically encoded calcium reporter<sup>51</sup>. Expression of RCaMP1 under the control of *da*-GAL4 did not reveal significant changes in calcium levels before wounding (Fig. 4e and Supplementary Movie 12). However, immediately after wounding, a dramatic increase of intracellular calcium was observed as a bright fluorescence signal, first observed in front-row cells, but then rapidly spreading to more distal cell rows within 20 s (Fig. 4e and Supplementary Movie 12). After initial calcium wave propagation, the levels of intracellular calcium decreased from the periphery to the margin of the wound within a minute (Supplementary Movie 12). Combined, these data strongly suggest that wound-induced cytosolic calcium increase might promote transient remodeling of the cortical actin cytoskeleton to allow subsequent lamellipodial protrusion and cell constriction driving wound closure (Fig. 4f).

**Swip-1 function is required for epithelial wound closure *in vivo*.**

We then explored the physiological function of Swip-1 in epithelial wound closure in more detail. Epithelial cells deficient for Swip-1 showed prominent wound closure defects (Fig. 5b, c). Mutant cells at the wound edge still formed cell protrusions (Fig. 5b, yellow arrowheads). However, the size and the sheet-like shape of these protrusions were reduced with more prominent irregular, highly unstable spike-like filopodia unlike wild-type cells (Supplementary Movie 13). To better quantify wound closure defects, we measured the wound area over 60 min, normalized to the initial wound size at time zero (Fig. 5c). In the wild type, in the first 90 s after ablation, the wound area first expanded as a possible consequence of tissue tension release as previously reported in embryonic wound closure<sup>49,50</sup>. Thereafter, wild-type cells immediately initiated the formation of lamellipodial protrusions (see Figs. 4c and 5c). By contrast, in *swip-1* deficient cells the initial expansion phase was prolonged and the formation of protrusions was markedly delayed (Fig. 5b, c). Even greater differences were observed in the subsequent contraction of cells at the wound margin, which already started after five minutes after ablation in the wild type. In contrast, in *swip-1* mutants wounds either completely failed to constrict or showed a dramatic delay



up to 25 min. Accordingly, mutant wounds remained nearly open even at 60 min after ablation, whereas wild-type wounds were generally already closed up to 70% of the initial wound size (Fig. 5d). Re-expression of a full-length Swip-1 protein, but not deletion constructs lacking either the EF-hands ( $\Delta\text{EF}$ ), deficient for calcium binding (EFhD2/Swip-1-D82A/D118A) or the coiled-coil domain ( $\Delta\text{CC}$ ) could substantially rescue wound closure defects (Fig. 5c, d). Taken together, these data indicate that appropriate wound closure requires both functional calcium-binding and dimerization of Swip-1. Mechanistically, these data provide a mechanism for how elevated calcium levels result in

rapid reorganization of actin networks driving epithelial wound closure. Given the cryptic lamellipodia formed at the mutant epithelial wound edge, Swip-1 seems to be not only essential for the initial calcium-dependent remodeling of actin filaments, but also later for stabilizing lamellipodia protrusions when calcium has been decreased to basal levels.

**EFhD2/Swip-1 stabilizes lamellipodial protrusions for efficient force transmission in adhesive 2D cell migration.** To experimentally test the relevance of EFhD2/Swip-1 in lamellipodium

**Fig. 3 EFhD2/Swip-1 is a calcium ( $\text{Ca}^{2+}$ )-regulated cross-linking protein. a, c** Co-sedimentation of *Drosophila* Swip-1 with F-actin in high-speed pelleting assays in the absence or presence of 1 mM  $\text{Ca}^{2+}$ . Increasing concentrations of *Drosophila* Swip-1 as indicated were incubated with 8  $\mu\text{M}$  G-actin in polymerization buffer, and the proteins recovered in the pellet (P) and the supernatant (S) fractions after the centrifugation at  $200,000 \times g$  were stained with Coomassie blue. **b, d** Quantification of equilibrium constants and binding sites ( $n$ ) on F-actin in the absence or presence of  $\text{Ca}^{2+}$  from experiments as shown in **a, c**. Points represent mean  $\pm$  SD of increasing concentrations from three independent co-sedimentation experiments ( $n = 3$ ). Solid red lines represent calculated binding isotherms. **e, f** Co-sedimentation of *Drosophila* Swip-1 with F-actin in low-speed pelleting assays at  $20,000 \times g$  in the absence or presence of 1 mM  $\text{Ca}^{2+}$ . Increasing concentrations of Swip-1 as indicated were incubated with 5  $\mu\text{M}$  G-actin in polymerization buffer, and the proteins in the pellet (P) and the supernatant (S) fractions were stained with Coomassie blue. **g** Quantification of F-actin in pellet fractions from experiments as shown in **e, f**. Bars represent mean  $\pm$  SD of three independent co-sedimentation experiments ( $n = 3$ ). Data points show the measured values of the experiments. **h**  $\text{Ca}^{2+}$  prevents stable cross-linking of actin filaments caused by *Drosophila* Swip-1. Time-lapse micrographs of TIRFM assays, used for the analysis of cross-linking behavior of Swip-1 in the absence or presence of 1 mM  $\text{Ca}^{2+}$ . Polymerization of 0.75 or 1.5  $\mu\text{M}$  G-actin (10% ATTO488-labeled) with 0.1  $\mu\text{M}$  (top) and 1.0  $\mu\text{M}$  *Drosophila* Swip-1 (middle) in the absence and presence of  $\text{Ca}^{2+}$ . Note significantly cross-linked networks in the absence of  $\text{Ca}^{2+}$  as compared to assay conditions in the presence of  $\text{Ca}^{2+}$ . The enlarged gallery of inset (dashed box) at the bottom displays dynamic cross-linking behavior of 1.0  $\mu\text{M}$  *Drosophila* Swip-1 in the presence of  $\text{Ca}^{2+}$  at higher temporal resolution. The blue arrowhead marks an attachment event of a short filament with the longer filament and the red arrowhead depicts the detachment of the short filament after 12 s. Time is given in seconds in the upper right corner of each frame. Scale bars 10  $\mu\text{m}$ . **i** Quantification of attachment and detachment events in the absence or presence of  $\text{Ca}^{2+}$ . Bars represent mean  $\pm$  SD from three movies each ( $n = 3$ ). Data points show the measured values of the experiments.

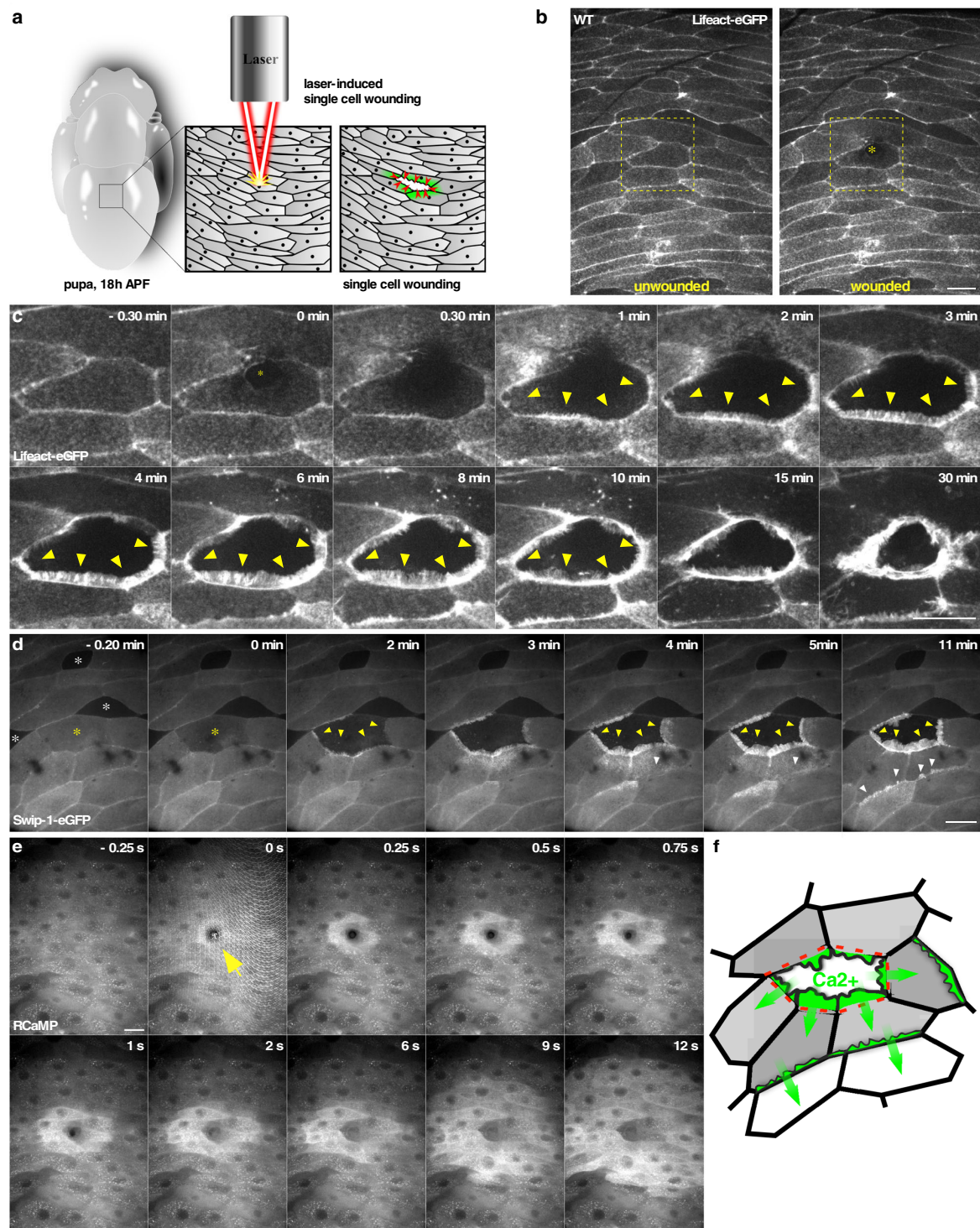
formation and protrusion in the absence of calcium gradients, we analyzed the function of EFhD2 in the highly polarized B16-F1 mouse melanoma cells forming prominent lamellipodia when migrating on laminin on a 2D surface. Subcellular localization of human EFhD2 in transiently transfected B16-F1 mouse melanoma cells confirmed its conserved localization in lamellipodial protrusions (ref. <sup>30</sup> and Fig. 6a). Human EFhD2 fused to EGFP could readily be observed in F-actin enriched lamellipodial protrusions and on intracellular vesicles (Fig. 6a). Co-immunostaining with antibodies directed against the WRC subunit WAVE2, the actin polymerase VASP, and the F-actin binding protein cortactin, which is highly reminiscent of Arp2/3 localization, revealed that EFhD2 localizes broadly within lamellipodia but not to the tip of the leading edge of B16-F1 cells (Fig. 6a). The siRNA or shRNA-mediated knockdowns of EFhD2 in HeLa, NIH 3T3, and B16-F10 cells have been previously reported to diminish cell spreading and wound healing in the scratch assay<sup>30,41</sup>. The latter study additionally observed diminished cell speed of EFhD2-depleted B16-F10 cells stably transduced with shRNA EFhD2 and shRNA-control in 2D assays. To thoroughly examine the function of EFhD2 in lamellipodium formation, protrusion, and 2D-cell migration on the single-cell level in a genetic knockout, we inactivated EFhD2 by CRISPR/Cas9 in B16-F1 cells. Disruption of the *EFhD2* gene in two independent clonal cell lines (KO #10 and #33) was verified by sequencing of genomic target sites and loss of protein was additionally confirmed by immunoblotting (Fig. 6b). Migration rates of B16-F1 wild-type cells and both mutants were then analyzed on laminin by phase-contrast time-lapse microscopy (Supplementary Movie 14). In line with the previous work<sup>41</sup>, loss of EFhD2 in B16-F1 cells caused a significant reduction in cell speed (Fig. 6c). Moreover, effective migration as assessed by quantification of mean square displacement (MSD) was substantially diminished (Fig. 6d). Since 2D migration on flat surfaces is largely driven by actin assembly in the lamellipodium, we then analyzed actin filament (F-actin) content in B16-F1 and EFhD2-KO cells after phalloidin staining. Notably, quantitative analysis of lamellipodia revealed no changes in F-actin intensity (Fig. 6f). Interestingly, however, lamellipodia widths in EFhD2 knockout cells on 2D substrates were reduced by almost 40% as compared to control (Fig. 6g). The number of microspikes in mutant cells though, remained unchanged as compared to control (Fig. 6h). Finally, we asked whether or to which extent lamellipodia protrusion was affected. To this end, we recorded the wild type and EFhD2-deficient cells randomly migrating on laminin by time-lapse, phase-contrast microscopy and determined the respective protrusion rates by kymograph analyses (Fig. 6i, j). Quantification

revealed lamellipodia protrusion to be reduced by about 30% in both mutants compared to the B16-F1 control (Fig. 6k). Combined these data strongly suggest that cross-linking of adjacent actin filaments within dendritic arrays by EFhD2 significantly contributes to the mechanical stability of lamellipodia to drive efficient protrusion.

## Discussion

**EFHD2/Swip-1 has a conserved function in lamellipodia-based protrusion and cell migration.** Previous studies have implicated EFHD2/Swip-1 in a number of cellular processes ranging from adhesion turnover, cell spreading and migration, B cell receptor signaling, and cancer invasion<sup>52</sup>. In this study, we identified an important role of EFHD2/Swip-1 in controlling lamellipodial protrusions and cell migration of *Drosophila* immune cells and B16-F1 mouse melanoma cells. How does EFhD2/Swip-1 act on lamellipodia-based protrusion? In variance with previous work, we found that human EFhD2 not only bundles actin filaments but also efficiently cross-link actin networks in vitro comparable to *Drosophila* Swip-1. The actin cross-linking activity of EFhD2 synergizes with WRC-Arp2/3-branched actin nucleation promoting the generation of a stable and densely branched actin filament network (Supplementary Movie 15). Supporting this notion, we found that loss of EFhD2/Swip-1 in both flies and B16-F1 cells decreases lamellipodia widths associated with markedly diminished protrusion rates, whereas forced over-expression of EFhD2/Swip-1 increases lamellipodia widths when plated on 2D surfaces. Given that cross-linking proteins largely determine the structure and viscoelastic properties of F-actin networks<sup>53</sup>, our findings strongly suggest that EFhD2/Swip-1 tunes mechanical force generation in protruding lamellipodia.

However, different from migrating B16-F1 cells in vitro, *Drosophila* macrophages deficient for Swip-1 show a significantly increased migratory speed in vivo. Notably, a similar observation was recently made in EFhD2-depleted mice in which B-cells were also shown to migrate faster in vivo<sup>35</sup>. This could be due to different protein requirements as well as different physical requirements for the distinct migration modes. The architecture of the actin cytoskeleton also depends on substrate rigidity and cells adapt to different extracellular resistance by reorganizing their actin network<sup>54,55</sup>. Thus, without cross-linking activity upon loss of EFhD2, the Arp2/3 complex might be insufficient for maintaining the mechanical stability of the branched actin network at the leading edge of B16-F1 cells. As a consequence, loss of EFhD2 in B16-F1 cells caused a significant reduction in



lamellipodial protrusion, cell speed, and effective migration. By contrast, immune cells migrate across a complex 3D environment with highly varying extracellular resistance that requires more dynamic protrusions. Thus, the loss of Swip-1 in *Drosophila* macrophages could result in a reduced actin network density that could lead to faster but less persistent migration in vivo.

Supporting this notion, we found that forced overexpression of Swip-1 stabilizes protrusions at the expense of migration speed in vivo. Thus, the assembly of cross-linking proteins such as EFhD2/Swip-1 into the branched actin network might contribute to a resistance-adaptive behavior of migrating cells as recently proposed<sup>56</sup>.

**Fig. 4 Swip-1 is recruited to lamellipodial protrusions during epithelial wound closure in vivo.** **a** Schematic of the in vivo model to study calcium-dependent wound healing in early *Drosophila* pupal stages. **b, c** Single-cell ablation in the abdominal epidermis of a wild-type 18 h APF old pupa ubiquitously expressing a Lifeact-eGFP transgene under the control of the *da-Gal4* driver. Images were taken every 30 s for 30 min, ablation starts at  $t = 0$  min. **b** Overview of the imaged area of the monolayered epithelium, an asterisk indicates ablated cell. Scale bar 25  $\mu\text{m}$ . **c** Magnification of the ablated cell of **b** at the indicated times. Arrows show forming lamellipodial protrusions at the wound margin. Scale bar 25  $\mu\text{m}$ . **d** Single-cell ablation in the abdominal epithelium of a 18 h APF old pupa ubiquitously expressing Swip-1-eGFP transgene; yellow asterisk indicates the position of the ablated cell. White asterisks mark specialized epidermal cells, so-called tendon cells providing attachment sides to the muscles. These tendon cells lack Swip-1-eGFP expression driven by the *da-Gal4* driver. Yellow arrows mark lamellipodial protrusions at the wound margin, whereas white arrows mark induced lamellipodia of cells several rows back from the wound site exhibited a delayed response. Scale bar 25  $\mu\text{m}$ . **e** Single-cell ablation in the abdominal epidermis of a 18 h APF old pupa ubiquitously expressing the calcium indicator RCaMP. Changes of intracellular calcium are visible as increasing fluorescence intensity. The calcium wave is propagated in a circular fashion with a velocity of  $2.2 \pm 0.7 \mu\text{m/s}$ . Scale bar 25  $\mu\text{m}$ . **c–e** Images shown are representative of **a** nine and **b, c** at least three independent experiments. **f** Schematic of the calcium wave-inducing membrane protrusions after wounding.

In addition, EFHD2/Swip-1 has been recently identified as a cargo-specific adapter for CG-endocytosis controlling integrin adhesion turnover<sup>32</sup>. This function might be also conserved and could further contribute to the changed migratory behavior of macrophages in vivo. Interestingly, we found that *swip-1*-deficient macrophages and those re-expressing the calcium-binding mutant Swip-1-D82A/D118A variant showed an increase in integrin-marked adhesions on vitronectin-coated surfaces. Enlarged focal adhesion caused by slower integrin turnover might further contribute to an increase in the migration speed as similarly observed for *zyxin*-deficient macrophages in *Drosophila*<sup>43</sup>. Interestingly, such a prominent inverse relationship between focal adhesion size and cell migration speed has been shown in numerous motile cell types<sup>57</sup>. The coordinated disassembly of integrin-mediated focal adhesions requires  $\text{Ca}^{2+}$  influx<sup>58,59</sup>; however, whether the function of EFHD2/Swip-1 in integrin traffic depends on its calcium-binding activity has not yet been addressed<sup>32</sup>.

**Calcium bursts allow a rapid reorganization of the actin cytoskeleton through Swip-1.** The mechanical properties of the actin cytoskeleton can not only adapt in response to extracellular resistance but also in response to intracellular calcium changes. Closure of wounds entails complex 3D movements of epithelial cells that are orchestrated by calcium signaling<sup>49,60,61</sup>. Laser-induced wounding immediately triggers a rapid calcium flash extending outward from the point of wounding as a wave<sup>49</sup>. Epithelial cells at the wound margin respond by polarizing their actin cytoskeleton to drive both protrusive structures and supracellular contractile actin cables, both contributing to efficient wound closure. During embryonic wound healing, lamellipodial and filopodial protrusions are often induced in later stages promoting the final sealing of the wound<sup>60,62</sup>. In our single-cell wounding model, wound closure starts with the formation of remarkably broad lamellipodial protrusions that depend on Swip-1 function. Swip-1 is immediately recruited to those lamellipodial protrusions not only directly adjacent to the wound but also in cells several rows back from the wound edge. Thus, Swip-1 resides at the heart of the first most prominent morphological changes in wound closure that require dynamic remodeling of the actin filament meshwork. How does Swip-1 contribute to this initial process? Previous in vitro studies reported that calcium promotes the bundling activity of EFHD2<sup>45</sup>. In this study, we could confirm the bundling activity of human EFHD2 protein by TIRF imaging. Contrary to previous assumptions, however, EFHD2-induced actin bundling was found to be calcium-insensitive. More importantly, we identified a conserved cross-linking activity that is regulated by calcium. As increased calcium levels promote the release of existing actin cross-links formed by EFHD2/Swip-1, we suggest a model in which elevated calcium concentrations reduce

EFHD2/Swip-1 cross-linking activity to promote rapid reorganization of existing actin networks, e.g. the cortical actin layer in pupa epithelia, allowing to drive fast and efficient epithelial wound closure by extension of newly formed lamellipodia (Fig. 7). Consistently, re-expression of calcium-binding deficient Swip-1 mutant did not rescue wound closure defects in *swip-1* deficient epidermal cells. As expected, this calcium-binding mutant still induced stable cross-links in a calcium-independent manner. Unexpectedly, however, this mutant protein additionally induced prominent actin bundles, an activity exclusively observed with human EFHD2. Of note, the determined X-ray structure of human EFHD2<sup>45</sup> and the predicted 3D structure of *Drosophila* Swip-1 computed by AlphaFold<sup>63</sup> could be precisely superimposed, thus excluding major conformational differences as the underlying reason explaining differential bundling or cross-linking of actin filament in the absence of calcium. On the other hand, conformational changes in EF-hands triggered by calcium binding, as previously shown for human EFHD2<sup>45</sup>, are likely to be responsible for the dissociation of cross-links formed by EFHD2 and Swip-1. We further hypothesize, that the acquired bundling activity of the Swip-1 mutant could also be driven by enhanced electrostatic interactions of the negative actin molecule with Swip-1, in which two negative residues were replaced by alanine (D82A/D118A). High-resolution X-ray structures of wild-type and mutant Swip-1 proteins will be necessary to resolve this important issue in future work.

Defective and delayed constriction of the wound margin in mutant epidermal cells further suggests that Swip-1 function is not only required for the formation and dynamics of lamellipodial protrusions but might also be involved in the subsequent formation of contractile actin cables forming along the wound margin. Supporting this notion, mouse EFHD2 has been recently identified as a binding partner of non-muscle myosin II heavy chain isoforms, including myosin 2a and myosin 2b<sup>64</sup>. Interestingly, non-muscle myosin II is not only a motor protein with contractile functions, but it can also cross-link actin filaments<sup>65,66</sup>. Thus, EFHD2/Swip-1 might act synergistically as a cross-linking protein together with myosin II in actomyosin-based contraction during wound closure, since myosin II has also been found to be immediately recruited to the wound edge after injury<sup>67</sup>. Given the large sizes of post-mitotic LECs, our single-cell wound system allows us to genetically dissect these different phases of wound healing at high spatial and temporal resolution in future work.

## Methods

**Bulk RNA-sequencing and bioinformatic analysis.** Total cellular RNAs from total larval hemocytes and pupal hemocytes, Hml+ larval hemocytes, and Hml+ pupal hemocytes were isolated in triplicates using the TRIzol Reagent (Thermo Fisher) following the manufacturer's protocol. The concentrations of RNA were determined using a NanoDrop ND-1000 (NanoDrop). The quality and integrity of the RNA

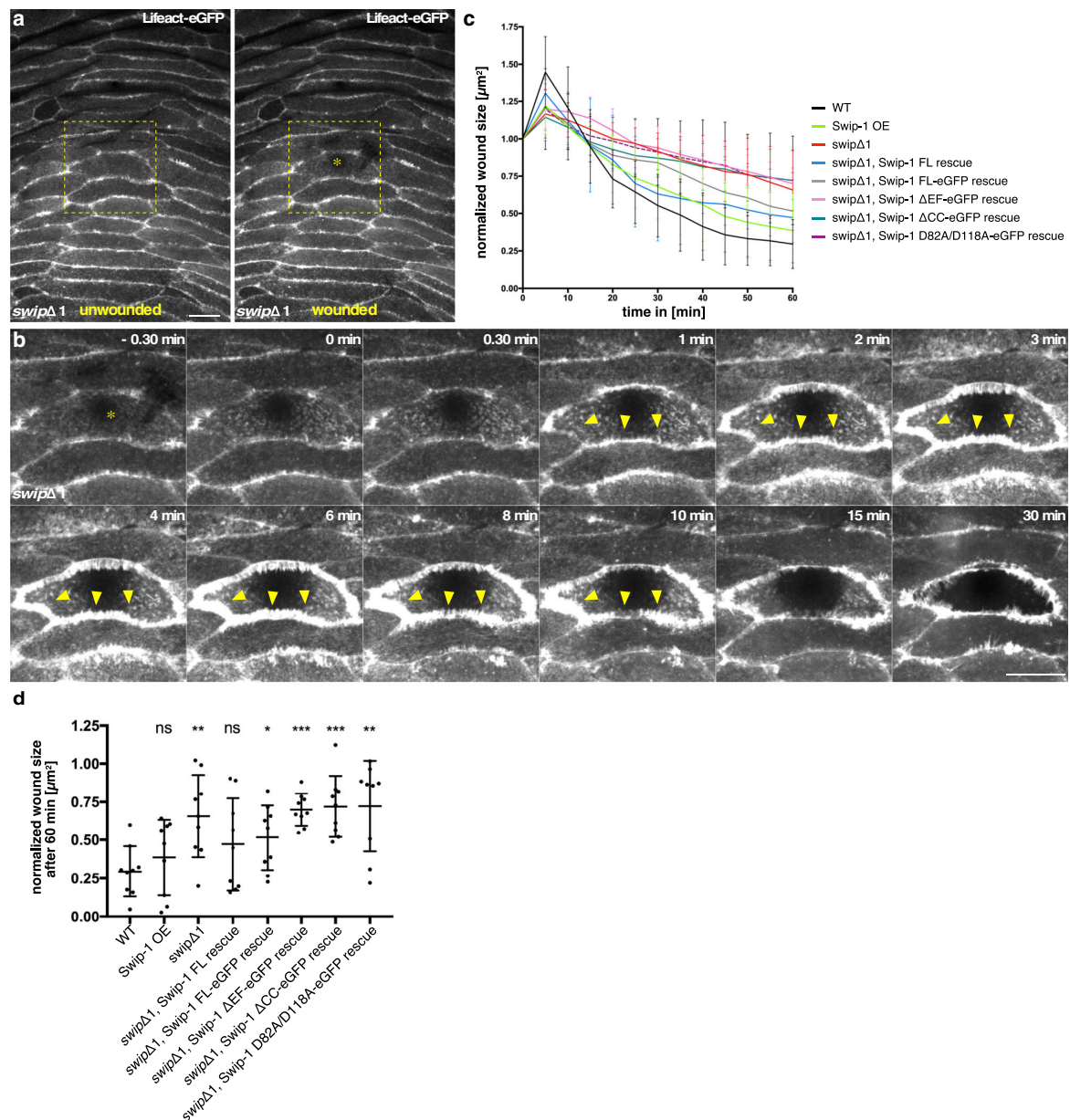
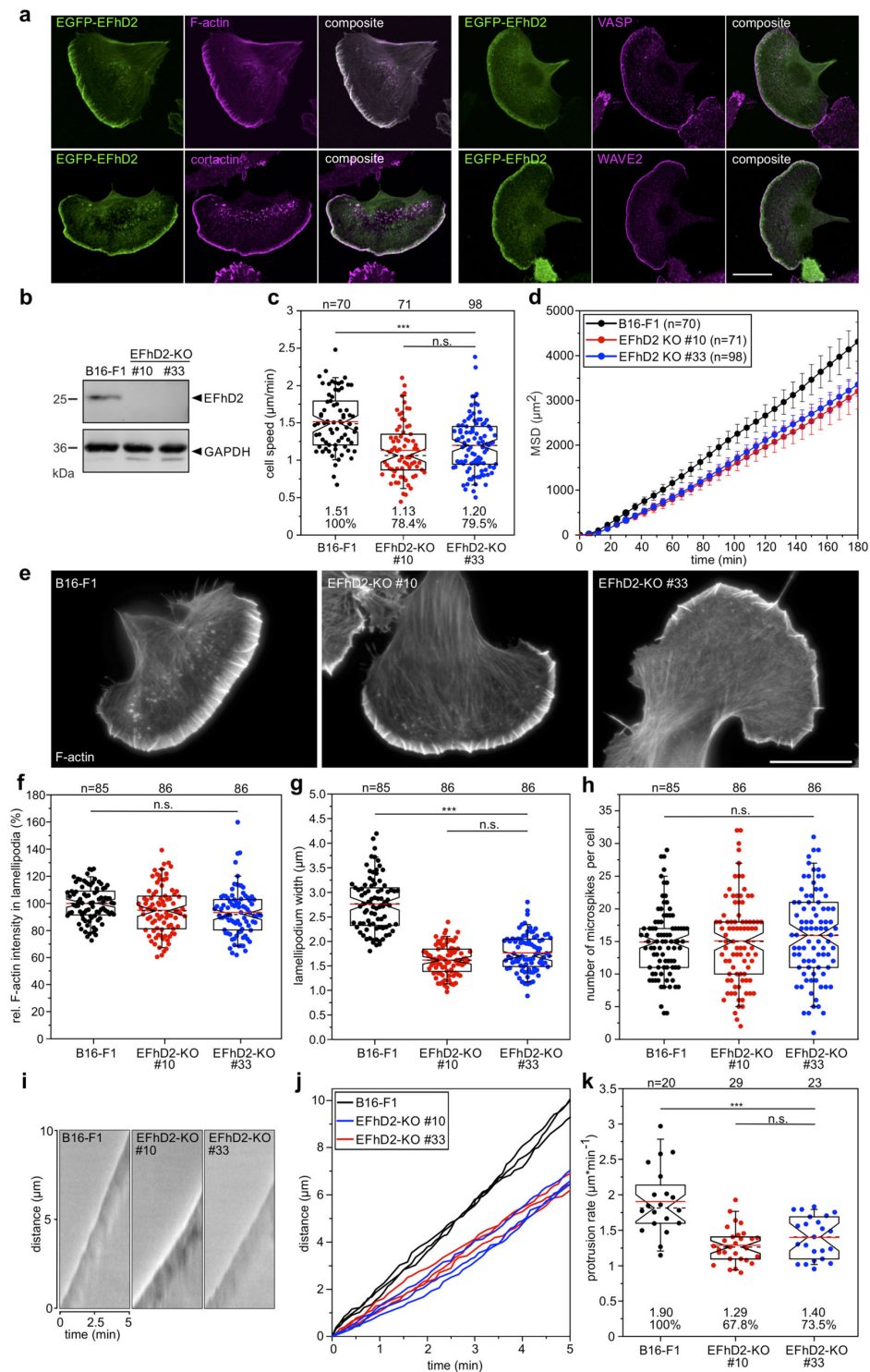


**Fig. 5 Epithelial wound closure requires Swip-1 function.** **a** Single-cell ablation in the abdominal epidermis of a *swip-1* mutant 18 h APF old pupa ubiquitously expressing a Lifeact-eGFP transgene under the control of the *da-Gal4* driver. Images were taken every 30 s for 60 min, ablation starts at  $t = 0$  min. Overview of the imaged area, an asterisk indicates the position of cell ablation. Scale bar 25  $\mu\text{m}$ . The image is representative of nine independent experiments. **b** Magnification of ablated cell shown in **a** at the indicated times, arrows indicate irregular unstable lamellipodial protrusions at the wound margin. Scale bar 25  $\mu\text{m}$ . **c** Quantification of wound closure in wild type (WT), *swip-1* mutant (*swipΔ1*), after overexpression (Swip-1 OE) and rescue by re-expressing distinct Swip-1 transgenes, FL: full-length;  $\Delta\text{EF}$ : lacks the EF hands and  $\Delta\text{CC}$ : lacks the coiled-coil region. Wound size was measured every 5 min and normalized to the initial size of the unwounded cell. **d** Excerpt of data from **c**. After 60 min, wound closure was assessed by comparing the remaining wound size normalized to unwounded cell size to wild type. Each point represents one experiment. *P* values: Swip-1 OE: 0.387, *swipΔ1*: 0.008, *swipΔ1*, Swip-1 FL rescue: 0.340, *swipΔ1*, Swip-1 FL-eGFP rescue: 0.040, *swipΔ1*, Swip-1  $\Delta\text{EF}$ -eGFP rescue: <0.001, *swipΔ1*, Swip-1  $\Delta\text{CC}$ -eGFP rescue: <0.001, *swipΔ1*, Swip-1-D82A/D118A-eGFP rescue: 0.006. **c**, **d** Bars represent the mean  $\pm$  SD of nine independent experiments for each genotype. Two-sided Mann-Whitney test was used to compare each genotype individually to WT, *P* values: 0.12 (ns), 0.033 (\*), 0.002 (\*\*), <0.001 (\*\*\*).

were assessed with the Fragment Analyzer (Advanced Analytical) by using the standard sensitivity RNA Analysis Kit (DNF-471). All samples selected for sequencing exhibited an RNA integrity number over 8. RNA-seq libraries were prepared from 100 ng total RNA using the TruSeq RNA Library Prep Kit (Illumina). For accurate quantitation of libraries, the QuantiFluor<sup>®</sup> dsDNA System (Promega)

was used. The fragment size of each library was analyzed using a Fragment Analyzer (Advanced Bioanalytical) by using the high sensitivity RNA Kit (Agilent). Libraries were pooled and sequenced on the Illumina HiSeq 4000 (SE; 1  $\times$  50 bp; 20–30 Mio reads/sample). Demultiplexing was done by using bcl2fastq v2.17.1.14. Adapter sequences were removed from demultiplexed fastq files by trimmomatic and



sequence quality was assured via FastQC. The reads were aligned to a reference *Drosophila* genome (dm6-v101) (*Drosophila\_melanogaster*.BDGP6.28.101.gtf) using STAR aligner 2.5<sup>68</sup>. Differential gene expression analysis was performed with DESeq2 v1.26.0<sup>69</sup>. The difference in expression patterns among samples was analyzed by principal component analysis (PCA). Visualization of differentially

expressed genes was performed with the heatmap package in Rstudio Version 1.4.1103.

**Drosophila genetics.** Fly husbandry and crossing were carried out according to the standard methods. All crosses were performed at 29 °C. The following fly stocks



**Fig. 6 Loss of EFhD2 impairs lamellipodia formation and adhesive 2D cell migration of mouse B16-F1 cells.** **a** EGFP-tagged EFhD2 expressed in B16-F1 cells co-localizes prominently with F-actin in the entire lamellipodium including microspikes. The other images display EGFP-EFhD2 expressing cells additionally stained for the actin polymerase VASP, cortactin, and the Arp2/3 complex activator WAVE2. Scale bar 20  $\mu\text{m}$ . **b** Elimination of EFhD2 by CRISPR/Cas9 in two independent B16-F1 mutants (#10 and #33) was confirmed by immunoblotting using specific antibodies. GAPDH was used as a loading control. **c** Elimination of EFhD2 diminishes cell migration on laminin. Three time-lapse movies from three independent experiments were analyzed for each cell line, B16-F1:  $n = 70$  cells tracked, mutant#10:  $n = 71$  cells tracked ( $P$  value:  $<0.001$  to B16-F1), mutant#33:  $n = 98$  cells tracked ( $P$  value:  $<0.001$  to B16-F1 and  $0.671$  to mutant#10). **d** Analyses of mean square displacement of wild-type and mutant cells. Respective symbols and error bars represent the means  $\pm$  SEM of three time-lapse movies from three independent experiments ( $n = 3$ ). **e** Loss of EFhD2 perturbs lamellipodia formation in B16-F1 cells. Representative examples of lamellipodia from wild-type B16-F1 and EFhD2-KO mutant cells. Cells migrating on laminin were stained for the actin cytoskeleton with phalloidin. Scale bar, 10  $\mu\text{m}$ . **f** Quantification of F-actin intensities in lamellipodia of wild-type and mutant cells after subtraction of background from three independent experiments, B16-F1:  $n = 85$  cells, mutant #10:  $n = 86$  cells ( $P$  value:  $0.061$  to B16-F1), mutant #33:  $n = 86$  cells ( $P$  value:  $0.005$  to B16-F1 and  $1$  to mutant #10). **g** Quantification of lamellipodia width in wild-type and mutant cells from three independent experiments, B16-F1:  $n = 85$  cells, mutant #10:  $n = 86$  cells ( $P$  value:  $<0.001$  to B16-F1), mutant #33:  $n = 86$  cells ( $P$  value:  $<0.001$  to B16-F1 and  $0.061$  to mutant #10). **h** Loss of EFhD2 does not impair microspike formation. Quantification of microspikes in wild-type and mutant cells from three independent experiments, B16-F1:  $n = 85$  cells, mutant #10:  $n = 86$  cells ( $P$  value:  $0.979$  to B16-F1), mutant #33:  $n = 86$  cells ( $P$  value:  $0.535$  to B16-F1 and  $0.654$  to mutant #10). **i** Loss of EFhD2 diminishes the efficacy of lamellipodium protrusion. Kymographs of representative phase-contrast movies are shown. **j** Multiple examples of lamellipodium protrusion in B16-F1 versus EFhD2-KO cells. **k** Quantification of protrusion rates from three independent experiments, B16-F1:  $n = 20$  cells, mutant #10:  $n = 29$  cells ( $P$  value:  $<0.001$  to B16-F1), mutant #33:  $n = 23$  cells ( $P$  value:  $0.535$  to B16-F1 and  $0.475$  to mutant #10). **c, f-h, k** Boxes in box plots indicate 50% (25–75%) and whiskers (5–95%) of all measurements, with dashed black lines depicting the medians, arithmetic means are highlighted in red. Non-parametric, Kruskal-Wallis test with Dunn's Multiple Comparison test (**c, f, k**) or one-way ANOVA with Tukey Multiple Comparison test (**g, h**) were used to reveal statistically significant differences between datasets.  $P$  value:  $>0.05$  (n.s.)  $<0.001$  (\*\*\*). All images shown are representative of three independent experiments unless otherwise specified.

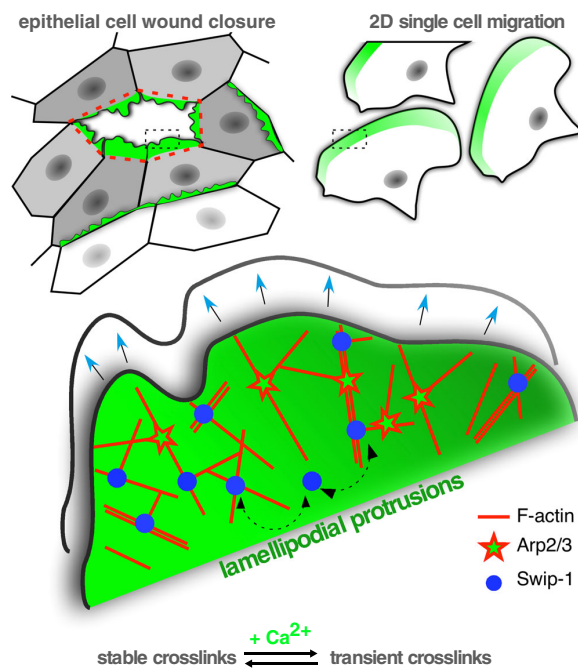


**Fig. 7 EFhD2/Swip-1 cross-linked lamellipodial actin networks drive single-cell migration and epithelial wound closure.** Schematic showing the proposed role of EFhD2/Swip-1 in regulating lamellipodial actin networks.

were obtained from the Bloomington stock center: w[1118] (BL3605), hml $\Delta$ -Gal4 (BL30139), y[ $\ast$ ] w[ $\ast$ ]; P{w[+mC]} = UAS-2xEGFP/AH3 (BL6658), w[ $\ast$ ]; P{w[+mC]} = UAS-Lifeact.GFP.W3 (BL57326), y[1] w[ $\ast$ ]; P{y[+ $\ast$ ] w[+mC]} = UAS-Lifeact-Ruby/VIE-19A (BL35545), w[ $\ast$ ]; PBac{w[+mC]} = 20XUAS-IVS-NES-jRCaMP1a-p10/VK00005 (BL63792). RNAi against EFhD2/Swip-1: w[1118]; P{GD7047}v31307 was obtained from the Vienna Drosophila RNAi Center. Transgenic UAST-Swip, UAST-Swip-eGFP, UAST-eGFP-Swip $\Delta$ EF, UAST-Swip $\Delta$ CC-eGFP and UAST-SwipD82A/D118A-eGFP flies were generated using  $\Phi$ C31-mediated transgenesis (y[1] M{vas-int.Dm}ZH2A w[ $\ast$ ]; M{3xP3-RFP.attP}ZH-86Fb (BL24749) and y[1] M{vas-int.Dm}ZH2A w[ $\ast$ ]; M{3xP3-RFP.attP}ZH-68E (BL24485)<sup>70</sup>. The swip $\Delta$  mutant was generated by CRISPR/Cas9 of the following target sequence: 5'-GGGGTCTTCGAGAAGACCT-3'. Loss of the EFhD2/

Swip-1 protein was confirmed by Western blot analysis stained against His-Swip-1 (Pineda, Berlin).

**Protein purification.** Expression of GST-tagged human EFhD2, wild type, and mutant Swip-1 in *Escherichia coli* strain Rossetta 2 (Novagen) was induced with 0.75 mM IPTG at 21  $^{\circ}\text{C}$  for 16 h. The bacteria were harvested and lysed by ultrasonication in PBS, pH 7.4 containing 5 mM benzamide, 1 mM DTT, 5% (v/v) glycerol, 0.1 mM AEBSF and 2 units/mL Benzamide (Novagen). The fusion proteins were purified from supernatants of bacterial extracts by affinity chromatography using glutathione-conjugated agarose 4B (Macherey-Nagel). The GST-tag was subsequently cleaved off by PreScission protease (GE Healthcare) and the GST tag was absorbed on fresh glutathione-conjugated agarose. Swip-1 in the flow through was further purified by size-exclusion chromatography using a preparative HiLoad 26/75 Superdex column controlled by an Äkta Purifier System (GE Healthcare). Fractions containing Swip-1 were pooled, dialyzed against 30 mM Hepes, pH 7.4 containing 150 mM NaCl, 1 mM DTT, 5% (vol/vol) glycerol, snap-frozen in liquid nitrogen, and stored at  $-80^{\circ}\text{C}$ . Actin was extracted and purified from acetone powder of rabbit skeletal muscle using standard procedures<sup>71</sup>. Fractions were labeled on Cys374 with ATTO488 maleimide (ATTO-TEC) and stored in G-Buffer (5 mM Tris/HCl pH 8, 0.2 mM ATP, 0.5 mM DTT, 0.2 mM  $\text{CaCl}_2$ , 0.1 mg/mL  $\text{NaN}_3$ ).

**Antibodies.** The rabbit anti-Swip-1 antibody was generated against the full-length *Drosophila* Swip-1 fused to a  $6 \times$  His-tag (pDEST17, ThermoFisher Scientific). The  $6 \times$  His-Swip fusion protein was expressed in *E. coli* and purified with Ni-NTA resin (GE Healthcare). Rabbits were immunized with purified proteins by Pineda Antikörper-service (Berlin, Germany).

For immunofluorescence of ex vivo *Drosophila* macrophages, the Swip (1:50,000 dilution) or  $\beta$ -integrin (1:10 dilution, CF.6G11 from DSHB) antibodies were used. Primary antibodies were visualized with polyclonal Alexa Fluor-568-conjugated goat-anti-rabbit (1:1000 dilution; #A11036, Invitrogen) or Alexa Fluor-647-conjugated goat-anti-mouse (1:1000 dilution; #A21236, Invitrogen) antibodies, respectively. F-actin was visualized using Alexa Fluor-488 or Alexa Fluor-568-conjugated Phalloidin (1:100 dilution, #A12379 #A12380, Invitrogen) and nucleus by DAPI staining (1  $\mu\text{g}/\text{mL}$ , #62248, Thermo Scientific). For immunofluorescence (B16-F1 cells) of primary polyclonal rabbit antibodies against VASP (1:1000 dilution<sup>7</sup>), cortactin (1:1000<sup>7</sup>), and WAVE2 (1:1000<sup>7</sup>) were used. Primary antibodies were visualized with polyclonal Alexa-555-conjugated (1:1000 dilution; #A21429, Invitrogen) or Alexa-488-conjugated (1:1000 dilution; #A-11034, Invitrogen) goat-anti-rabbit antibodies. The EGFP-signal of transfected cells expressing EGFP-tagged EFhD2/Swip-1 was enhanced with Alexa-488-conjugated nanobodies<sup>72</sup>. ATTO550-phalloidin (1:250 dilution, #AD550-82, Atto-Tec) was used for visualization of F-actin. For immunoblotting polyclonal rabbit anti-EFhD2/Swip-1 (from collaborator) antibody or mouse monoclonal antibody against glyceraldehyde-3-phosphate dehydrogenase (GAPDH) (1:1000; #CB1001-500UG, Merck) were used and visualized using phosphatase-coupled anti-rabbit (1:1000 dilution; #115-055-144, Dianova) or anti-mouse antibodies (1:1000 dilution; #115-055-62, Dianova). Anti-EFhD2 antibody was kindly provided by Dirk Mielenz, Erlangen.

**Validation of knock-out and knock-down of EFhD2/Swip-1.** For cell-type-specific knock-down in macrophages, EFhD2/Swip-1 RNAi lines were crossed with macrophage-specific hmlA driver line. Macrophages of 35 L3 larvae were isolated in 1 mL unsupplemented Schneider's medium, centrifuged for 5 min at 800 × g, and the supernatant carefully removed. Cells were resuspended in 10 μL 4 × SDS sample buffer and incubated at 95 °C for 10 min for SDS-PAGE. EFhD2/Swip-1 null-mutants were validated by decapitating 10 flies and squashing the heads in 30 μL 2 × SDS sample buffer and incubation at 95 °C for 10 min for SDS-PAGE. The following antibodies were used for Western Blot analysis: anti- EFhD2/Swip-1 (1:5000 dilution), Anti-Actin AB-5 (1:5000 dilution, BD Biosciences), IRDye 800CW Goat anti-Rabbit IgG and IRDye 680LT Goat anti-Mouse IgG Secondary Antibody (1:10,000 dilution, LI-COR).

**Cell culture and cell transfection.** *Drosophila* S2R+ cells were propagated as described previously<sup>73</sup>. In short, cells were propagated in 1 × Schneider's *Drosophila* medium (Gibco) supplemented with 10% FBS, 50 units/mL penicillin, and 50 μg/mL streptomycin in 25 cm<sup>2</sup> Corning cell culture flask (Thermo Fisher). S2R+ cells were cotransfected with 0.6 μg Act5c-GAL4 and 1 μg DNA of respective gene of interest with a UAS sequence<sup>74</sup>. For estimation of the EFhD2/Swip-1 content in S2 and S2R+ cells, recombinant EFhD2/Swip-1 and cell lysates were immunoblotted and band intensities were compared using LabImage 4.2.1 (Kapelan Bio-Imaging). S2 and S2R+ cells were also stained with Hoechst 33342 (Thermo Scientific) for 30 min and imaged before settling on the surface with a Leica TCS SP8 with an HC PL APO CS2 ×63/1.4 oil objective. Cell and nucleus sizes were calculated assuming a circular shape. Molarity of Swip-1 in the cytosol was calculated with the known concentration of recombinant Swip-1 and specific cell number in the cell lysates of the immune blots.

B16-F1 (ATTC, CRL-6323) and derived cells were cultured in high-glucose DMEM culture medium (Lonza) supplemented with 1% penicillin-streptomycin (Biowest), 10% FBS (Biowest), and 2 mM UltraGlutamine (Lonza) at 37 °C in a 5% CO<sub>2</sub> atmosphere. B16-F1 cells were transfected with 1 μg plasmid DNA using JetPRIME transfection reagent (PolyPlus) in 35 mm diameter wells (Sarstedt) following the manufacturer's protocol. For the expression of GFP-tagged EFhD2/Swip-1 in B16-F1 cells, a cDNA fragment encoding full-length EFhD2 was amplified from pCMV-Sport6-EFhD2 using the primers 5'-GTGAGATCTATGGCCACGGACGAGCTGGCCAC-3' and 5'-CACGTCCACCTACTTAAAGGTGGACTGCAGCTC-3' and inserted into the Bgl2-SalI sites of plasmid EGFP-C1 (Clontech). The fidelity of generated plasmids was confirmed by sequencing.

**CRISPR/Cas9-mediated genome editing.** CRISPR/Cas9 technology was used to inactivate the *EFhD2/Swip-1* gene in B16-F1 mouse melanoma cells<sup>75</sup>. DNA target sequences of exon 1 were pasted into the CRISPR/Cas9 target online predictor tool CCTop (<https://cctop.cos.uni-heidelberg.de:8043/>) to generate sgRNA of 20 nucleotides with high-efficiency scores and minimal off-target efficiency and to cover all possible splice variants of the gene. The derived targeting sequence 5'-CGGGCGCGGACCTCAACCA-3' and the corresponding reverse oligonucleotide were hybridized and inserted into BbsI site of plasmid pSpCas9(BB)-2A-Puro(PX459)V2.0 (Addgene plasmid ID: 62988)<sup>76</sup>. Validation of CRISPR construct sequences was performed using a 5'-GGACTATCATATGCTTACCG-3' sequencing primer. 24 h after transfection with the CRISPR construct, the cells were selected in a culture medium containing 2.5 μg/mL puromycin for 4 days and then cultivated for 24 h in the absence of puromycin. For isolation of clonal knockout cell lines, single cells were seeded by visual inspection into 96-well microtiter plates and expanded in pre-conditioned culture medium. Clones were analyzed by the TIDE sequence trace decomposition web tool (<https://tide.deskgen.com/>) and confirmed by immunoblotting using specific antibodies.

**TIRF microscopy.** TIRFM assays were performed in TIRF buffer (20 mM imidazole pH 7.4, 1 mM MgCl<sub>2</sub>, 50 mM KCl, 0.5 mM ATP, 20 mM β-mercaptoethanol, 2.5 mg/mL methylcellulose (4000 cP), 15 mM glucose, 100 μg/mL glucose oxidase, and 20 μg/mL catalase), either in the absence or presence of 1 mM EGTA. In reactions without EGTA, a final concentration of 1 mM CaCl<sub>2</sub> was used. Concentrations of 0.1 μM or 1 μM and of EFhD2/Swip-1 were used for the TIRF assays to investigate the concentration- and Ca<sup>2+</sup>-dependent cross-linking behavior of EFhD2/Swip-1. The reactions were initiated by the addition of G-actin (0.5, 0.75, or 1.5 μM final concentration, 10% ATTO488-labeled at Cys374) and the mixtures were subsequently flushed into mPEG-silan (Mr 2000) (Lysan Bio)-pre-coated flow chambers. Higher concentrations of G-actin were used for the TIRF assays in presence of Ca<sup>2+</sup> to account for the slower actin assembly rates under these conditions<sup>78</sup>. Images were acquired with a Nikon Eclipse TI-E inverted microscope equipped with a TIRF Apo ×100 NA 1.49 oil immersion objective at 0.5-s intervals with exposure times of 70 ms by an Ixon3 897 EMCCD camera (Andor) for at least 15 min.

**High- and low-speed sedimentation assays.** For high-speed sedimentation assays, 8 μM G-actin was polymerized in the presence of EFhD2/Swip-1 at the concentrations indicated either in 1 × KMEI (10 mM imidazole pH 7.0, 50 mM KCl, 1 mM MgCl<sub>2</sub>, 1 mM EGTA) or 1 × KMI (10 mM imidazole pH 7.0, 50 mM KCl, 1 mM MgCl<sub>2</sub>) with 1 mM CaCl<sub>2</sub> for 2 h at 4 °C. Subsequently, the samples

were centrifuged at 200,000 × g at 4 °C for 1 h and the pellets were brought to the original volume in 1 × SDS sample buffer. To quantitate co-sedimentation of EFhD2/Swip-1 with F-actin, after SDS-PAGE and Coomassie Blue staining, the amount of the proteins in the pellet and supernatant fractions was determined densitometrically using the ImageJ software. Calculations of free and bound EFhD2/Swip-1 were determined by the ratio of band intensities in respective fractions. The dissociation constants ( $K_D$ ) and the number of EFhD2/Swip-1 binding sites ( $n$ ) on actin was obtained by non-linear, least-square fitting assuming a model of independent, identical binding sites with the SOLVER plug-in in Excel (Microsoft) using the following equation:

$$[\text{Swip}_{\text{bound}}] = \frac{(n \cdot [\text{actin}_{\text{total}}] + [\text{Swip}_{\text{total}}] + K_D)}{2} - \sqrt{\left(\frac{n \cdot [\text{actin}_{\text{total}}] + [\text{Swip}_{\text{total}}] + K_D}{2}\right)^2 - n \cdot [\text{actin}_{\text{total}}] \cdot [\text{Swip}_{\text{total}}]} \quad (1)$$

For low-speed sedimentation assays, 5 μM G-actin was polymerized in the presence of various concentrations of EFhD2/Swip-1 in the same buffers and at the same conditions as described above. The samples were then centrifuged at 20,000 × g at 4 °C for 1 h and the pellets were brought to the original volume in a 1 × SDS sample buffer. To quantitate the extent of cross-linking induced by EFhD2/Swip-1, after SDS-PAGE and Coomassie Blue staining, the amount of F-actin in the pellet and supernatant fractions was determined densitometrically using Image J software.

**Immunohistochemistry and fluorescence staining.** Pupal macrophages were isolated as described previously<sup>79</sup>. In short, white to light brownish prepupae were collected and washed in 1 × PBS. The prepupae were moved to 1 × Schneider's *Drosophila* medium (Gibco) supplemented with 10% FBS, 50 units/mL penicillin, and 50 μg/mL streptomycin and opened to rinse out the hemolymph. Cells were spread on ConcanavalinA (0.5 mg/mL, Sigma) coated glass coverslips for 1 h at 25 °C and subsequently fixed for 15 min with 4% paraformaldehyde in 1 × PBS. Cells were washed once with 1 × PBS+0.1% TritonX-100 and three times with 1 × PBS. If no antibody staining was performed, the washing step with PBS-T was omitted. Cells were stained with primary antibody overnight at 4 °C and secondary antibody with Phalloidin and DAPI for 45 min at room temperature in a humidified chamber. Stained cells were mounted in Mowiol 4–88 (Carl Roth). Cell size and morphology were analyzed by using Image J shape descriptors. Circularity ranges from 0 (infinitely elongated polygon) to 1 (perfect circle) (ImageJ, NIH). The length of randomly chosen focal adhesions in the lamellipodium of macrophages was measured using Image J.

The B16-F1 cells were fixed in pre-warmed PBS, pH 7.4 containing 4% paraformaldehyde and 0.06% picric acid for 20 min and subsequently washed three times with 100 mM glycine in PBS to quench the fixative. The cells were then permeabilized with 0.1% Triton X-100 in PBS for 30 s and blocked with PBG (PBS containing 0.045% cold fish gelatin (Sigma) and 0.5% BSA) for 30 min. Fixed specimens were incubated with primary antibodies overnight followed by incubation with secondary polyclonal goat-anti-rabbit antibodies for 2 h. ATTO550-phalloidin was used for the visualization of F-actin.

**Fluorescence microscopy.** Confocal images were taken with a Leica TCS SP8 with an HC PL APO CS2 ×63/1.4 oil objective and Leica Application Suite X (LasX) software. Structure illumination microscopic images were taken with a Zeiss ELYRA PS1 Microscope with a ×63/1.4 oil objective. Live imaging of macrophages was performed using a Zeiss CellObserver Z.1 with a Yokogawa CSU-X1 spinning disk scanning unit and an AxioCam MRm CCD camera (6.45 μm × 6.45 μm) and ZenBlue 2.5 software. Laser ablation of single cells was done using the UV laser ablation system DL-355/14 from Rapp Optoelectronics. Imaging of fixed B16-F1 cells was performed with an Olympus XI-81 inverted microscope equipped with an UPlan FI ×100/1.30NA oil immersion objective or a Zeiss LSM980 confocal microscope equipped with a Plan-Neofluar ×63/1.45NA oil immersion objective using 488 nm and 561 nm laser lines. Fluorescence intensities of phalloidin-stained lamellipodia were quantified from 8-bit images captured at identical settings using ImageJ software after background subtraction. Relative mean pixel intensities in lamellipodial regions of interest are shown as whiskers-box plots including all data points. The numbers of microspikes were manually counted.

**Live-cell imaging of pupal macrophages.** Live imaging of macrophages in prepupae was performed as previously reported<sup>79</sup>. In short, white prepupae were collected and glued to a glass coverslip on their dorsal-lateral side. Spinning disk time-lapse movies were taken with images every 20 s for 30 min. For tracking, a maximum projection of the acquired z-stack was obtained. Migrating macrophages were automatically tracked and manually corrected using the Imaris 9.3 software (Bitplane). For automatic detection of the cells, estimated diameter of 5 μm was assumed. Tracks were followed using an autoregressive motion algorithm to model the motion allowing a maximum distance of 10 μm between spots and a maximum gap size of 3. With manual correction of the tracks, gap sizes were reduced to a minimum. Specific values of Track Speed Mean, Track Displacement Length, and Track Straightness were obtained from the software.

**Live-cell imaging of wound closure of pupal epithelium.** Single epithelial cells of 18–20 h APF pupal abdomen were ablated using the UV laser ablation system DL-355/14 from Rapp OptoElectronics and wound closure was observed for 1 h every 30 s on a Zeiss CellObserver Z.1 with a Yokogawa CSU-X1 spinning disk scanning unit and an AxioCam MRm CCD camera (6.45  $\mu\text{m}$   $\times$  6.45  $\mu\text{m}$ ). Wound closure was analyzed by measuring the wound size in 5 min increments using freehand selections in Image J.

**Live-cell imaging of B16-F1 cells.** B16-F1 cells and EFhd2/Swip-1 KO mutant cells were seeded in low density onto 35 mm glass-bottom dishes (Ibidi) coated with 25  $\mu\text{g}/\text{mL}$  laminin and allowed to spread for 3 h. To compensate for the lack of  $\text{CO}_2$  during imaging, 25 mM HEPES, pH 7.0 was added to the medium. After mounting the chamber into the heating system (Ibidi), the cells were recorded by time-lapse phase-contrast imaging at 60 s intervals for 3 h using Olympus XI-81 inverted microscope (Olympus) driven by Metamorph software (Molecular Devices) and equipped with an UPlan FL N  $\times 40/1.3\text{NA}$  objective (Olympus) and a CoolSnap EZ camera (Photometrics). Cells were tracked individually with the ImageJ Plugin MTrackJ. Cells that contacted each other or divided were excluded from analyses. Mean square displacements and cell speed were calculated in Excel (Microsoft) using a customized macro<sup>80</sup>. Lamellipodium protrusion was determined based on kymographs generated from time-lapse movies recording advancing lamellipodia at 5 s intervals over a time period of at least 10 min using a UPlan FI  $\times 100/1.30\text{NA}$  oil immersion objective (Olympus). Kymographs were generated using ImageJ software by drawing lines from inside the cell and across the lamellipodium. Protrusion rates were calculated from respective slopes in kymographs.

**Statistical analysis.** Quantitative experiments were performed at least in triplicates to avoid any possible bias by environmental effects or unintentional error. Raw data were processed in Excel (Microsoft). Statistical analyses were performed using GraphPad Prism 7 (GraphPad) or Origin 2021 Pro (OriginLab). All data sets were tested for normality by the Shapiro–Wilk test. Statistical differences between normally distributed datasets of two groups were revealed by the *t* test and not normally distributed datasets of two groups by the non-parametric Mann–Whitney *U* rank-sum test. The Mann–Whitney test was used and *P* value (two-tailed) was obtained (*P* value: 0.12 (ns), 0.033 (\*), 0.002 (\*\*), <0.001 (\*\*\*)). For comparison of more than two groups, the statistical significance of normally distributed data was examined by one-way ANOVA followed by Tukey Multiple Comparison. In the case of not normally distributed data, the non-parametric Kruskal–Wallis test followed by Dunn’s Multiple Comparison was used. Statistical differences are reported as \**p* < 0.05, \*\**p* < 0.01, \*\*\**p* < 0.001, and n.s.

**Reporting summary.** Further information on research design is available in the Nature Research Reporting Summary linked to this article.

### Data availability

The data that support the findings of this study are available within the article, Supplementary Information, or from the corresponding author upon reasonable request. The raw gene expression data generated in this study have been deposited in the NCBI Gene Expression Omnibus (GEO) database under accession code [GSE200966](https://www.ncbi.nlm.nih.gov/geo/query/acc.cgi?acc=GSE200966). Source Data are provided with this paper.

Received: 26 October 2021; Accepted: 19 April 2022;

Published online: 06 May 2022

### References

- Svitkina, T. The Actin Cytoskeleton and Actin-Based Motility. *Cold Spring Harb. Perspect. Biol.* **10**, <https://doi.org/10.1101/cshperspect.a018267> (2018).
- Pollard, T. D. Actin and actin-binding proteins. *Cold Spring Harb. Perspect. Biol.* <https://doi.org/10.1101/cshperspect.a018226> (2016).
- Rotty, J. D., Wu, C. & Bear, J. E. New insights into the regulation and cellular functions of the ARP2/3 complex. *Nat. Rev. Mol. Cell Biol.* **14**, 7–12 (2013).
- Papalazarou, V. & Machesky, L. M. The cell pushes back: the Arp2/3 complex is a key orchestrator of cellular responses to environmental forces. *Curr. Opin. Cell Biol.* **68**, 37–44 (2021).
- Suetsugu, S., Miki, H. & Takenawa, T. Spatial and temporal regulation of actin polymerization for cytoskeleton formation through Arp2/3 complex and WASP/WAVE proteins. *Cell Motil. Cytoskeleton* **51**, 113–122 (2002).
- Pollard, T. D. Regulation of actin filament assembly by Arp2/3 complex and formins. *Annu. Rev. Biophys. Biomol. Struct.* **36**, 451–477 (2007).
- Damiano-Guercio, J. et al. Loss of Ena/VASP interferes with lamellipodium architecture, motility and integrin-dependent adhesion. *Elife* <https://doi.org/10.7554/eLife.55351> (2020).
- Mullins, R. D., Stafford, W. F. & Pollard, T. D. Structure, subunit topology, and actin-binding activity of the Arp2/3 complex from *Acanthamoeba*. *J. Cell Biol.* **136**, 331–343 (1997).
- Kage, F. et al. FMNL formins boost lamellipodial force generation. *Nat. Commun.* **8**, 14832 (2017).
- Small, J. V., Winkler, C., Vinzenz, M. & Schmeiser, C. Reply: Visualizing branched actin filaments in lamellipodia by electron tomography. *Nat. Cell Biol.* **13**, 1013–1014 (2011).
- Vinzenz, M. et al. Actin branching in the initiation and maintenance of lamellipodia. *J. Cell Sci.* **125**, 2775–2785 (2012).
- Ydenberg, C. A., Smith, B. A., Breitsprecher, D., Gelles, J. & Goode, B. L. Cease-fire at the leading edge: new perspectives on actin filament branching, debranching, and cross-linking. *Cytoskeleton* **68**, 596–602 (2011).
- Chaubet, L., Chaudhary, A. R., Heris, H. K., Ehrlicher, A. J. & Hendricks, A. G. Dynamic actin cross-linking governs the cytoplasm’s transition to fluid-like behavior. *Mol. Biol. Cell* **31**, 1744–1752 (2020).
- Flanagan, L. A. et al. Filamin A, the Arp2/3 complex, and the morphology and function of cortical actin filaments in human melanoma cells. *J. Cell Biol.* **155**, 511–517 (2001).
- Giganti, A. et al. Actin-filament cross-linking protein T-plastin increases Arp2/3-mediated actin-based movement. *J. Cell Sci.* **118**, 1255–1265 (2005).
- Shinomiya, H. Plastin family of actin-bundling proteins: its functions in leukocytes, neurons, intestines, and cancer. *Int. J. Cell Biol.* **2012**, 213492 (2012).
- Vadlamudi, R. K. et al. Filamin is essential in actin cytoskeletal assembly mediated by p21-activated kinase 1. *Nat. Cell Biol.* **4**, 681–690 (2002).
- Harker, A. J. et al. Ena/VASP processive elongation is modulated by avidity on actin filaments bundled by the filopodia cross-linker fascin. *Mol. Biol. Cell* **30**, 851–862 (2019).
- Burton, K. M. et al. Dynamin 2 interacts with alpha-actinin 4 to drive tumor cell invasion. *Mol. Biol. Cell* **31**, 439–451 (2020).
- Meacci, G. et al. alpha-Actinin links extracellular matrix rigidity-sensing contractile units with periodic cell-edge retractions. *Mol. Biol. Cell* **27**, 3471–3479 (2016).
- Jansen, S. et al. Mechanism of actin filament bundling by fascin. *J. Biol. Chem.* **286**, 30087–30096 (2011).
- Revenu, C., Athman, R., Robine, S. & Louvard, D. The co-workers of actin filaments: from cell structures to signals. *Nat. Rev. Mol. Cell Biol.* **5**, 635–646 (2004).
- Kretsinger, R. H. & Schaffer, J. E. In *Encyclopedia of Biological Chemistry III (Third Edition)* (ed. Joseph, J.) 630–636 (Elsevier, 2021).
- Garbett, D. et al. T-Plastin reinforces membrane protrusions to bridge matrix gaps during cell migration. *Nat. Commun.* **11**, 4818 (2020).
- Giorgi, C., Marchi, S. & Pinton, P. The machineries, regulation and cellular functions of mitochondrial calcium. *Nat. Rev. Mol. Cell Biol.* **19**, 713–730 (2018).
- Vuadens, F. et al. Identification of swiprosin 1 in human lymphocytes. *Proteomics* **4**, 2216–2220 (2004).
- Vega, I. E. et al. A novel calcium-binding protein is associated with tau proteins in tauopathy. *J. Neurochem.* **106**, 96–106 (2008).
- Hornbruch-Freitag, C., Griemert, B., Buttgeriet, D. & Renkawitz-Pohl, R. Drosophila Swiprosin-1/EFHD2 accumulates at the prefusion complex stage during Drosophila myoblast fusion. *J. Cell Sci.* **124**, 3266–3278 (2011).
- Ferrer-Acosta, Y., Rodriguez Cruz, E. N., Vaquer Adel, C. & Vega, I. E. Functional and structural analysis of the conserved EFhd2 protein. *Protein Pept. Lett.* **20**, 573–583 (2013).
- Kwon, M. S. et al. Swiprosin-1 is a novel actin bundling protein that regulates cell spreading and migration. *PLoS ONE* **8**, e71626 (2013).
- Dutting, S., Brachs, S. & Mielenz, D. Fraternal twins: Swiprosin-1/EFhd2 and Swiprosin-2/EFhd1, two homologous EF-hand containing calcium binding adaptor proteins with distinct functions. *Cell Commun Signal* **9**, 2 (2011).
- Moreno-Layseca, P. et al. Cargo-specific recruitment in clathrin- and dynamin-independent endocytosis. *Nat. Cell Biol.* **23**, 1073–1084 (2021).
- Tu, Y. et al. EFhd2/swiprosin-1 regulates LPS-induced macrophage recruitment via enhancing actin polymerization and cell migration. *Int. Immunopharmacol.* **55**, 263–271 (2018).
- Zhang, S. et al. Swiprosin-1 deficiency impairs macrophage immune response of septic mice. *JCI Insight* **3**, e95396 (2018).
- Reimer, D. et al. B cell speed and B-FDC contacts in germinal centers determine plasma cell output via Swiprosin-1/EFhd2. *Cell Rep.* **32**, 108030 (2020).
- Sampson, C. J., Amin, U. & Couso, J. P. Activation of Drosophila hemocyte motility by the ecdysone hormone. *Biol. Open* **2**, 1412–1420 (2013).
- Sander, M., Squarr, A. J., Risse, B., Jiang, X. & Bogdan, S. Drosophila pupal macrophages—a versatile tool for combined ex vivo and in vivo imaging of actin dynamics at high resolution. *Eur. J. Cell Biol.* **92**, 349–354 (2013).
- Lammel, U. et al. The Drosophila FHOD1-like formin Knittrig acts through Rok to promote stress fiber formation and directed macrophage migration during the cellular immune response. *Development* **141**, 1366–U1349 (2014).

39. Mun, S. A. et al. Structural and biochemical characterization of EFhd1/Swiprosin-2, an actin-binding protein in mitochondria. *Front. Cell Dev. Biol.* **8**, 628222 (2020).
40. Huh, Y. H. et al. Swiprosin-1 modulates actin dynamics by regulating the F-actin accessibility to cofilin. *Cell. Mol. Life Sci.* **70**, 4841–4854 (2013).
41. Huh, Y. H. et al. Swiprosin-1 stimulates cancer invasion and metastasis by increasing the Rho family of GTPase signaling. *Oncotarget* **6**, 13060–13071 (2015).
42. Yanagawa, S., Lee, J. S. & Ishimoto, A. Identification and characterization of a novel line of *Drosophila* Schneider S2 cells that respond to wingless signaling. *J. Biol. Chem.* **273**, 32353–32359 (1998).
43. Moreira, C. G., Jacinto, A. & Prag, S. *Drosophila* integrin adhesion complexes are essential for hemocyte migration in vivo. *Biol. Open* **2**, 795–801 (2013).
44. Gutierrez-Ford, C. et al. Characterization of tescalcin, a novel EF-hand protein with a single Ca<sup>2+</sup>-binding site: metal-binding properties, localization in tissues and cells, and effect on calcineurin. *Biochemistry* **42**, 14553–14565 (2003).
45. Park, K. R. et al. Structural implications of Ca(2+)-dependent actin-bundling function of human EFhd2/Swiprosin-1. *Sci. Rep.* **6**, 39095 (2016).
46. Winterhoff, M., Bruhmann, S., Franke, C., Breitsprecher, D. & Faix, J. Visualization of actin assembly and filament turnover by in vitro multicolor TIRF microscopy. *Methods Mol. Biol.* **1407**, 287–306 (2016).
47. Pinotsis, N. et al. Calcium modulates the domain flexibility and function of an alpha-actinin similar to the ancestral alpha-actinin. *Proc. Natl Acad. Sci. USA* **117**, 22101–22112 (2020).
48. Madhavan, M. M. & Madhavan, K. Morphogenesis of the epidermis of adult abdomen of *Drosophila*. *J. Embryol. Exp. Morphol.* **60**, 1–31 (1980).
49. Razzell, W., Evans, I. R., Martin, P. & Wood, W. Calcium flashes orchestrate the wound inflammatory response through DUOX activation and hydrogen peroxide release. *Curr. Biol.* **23**, 424–429 (2013).
50. Antunes, M., Pereira, T., Cordeiro, J. V., Almeida, L. & Jacinto, A. Coordinated waves of actomyosin flow and apical cell constriction immediately after wounding. *J. Cell Biol.* **202**, 365–379 (2013).
51. Dana, H. et al. Sensitive red protein calcium indicators for imaging neural activity. *Elife* <https://doi.org/10.7554/eLife.12727> (2016).
52. Thylur, R. P., Gowda, R., Mishra, S. & Jun, C. D. Swiprosin-1: its expression and diverse biological functions. *J. Cell Biochem.* **119**, 150–156 (2018).
53. Lieleg, O., Schmoller, K. M., Claessens, M. M. & Bausch, A. R. Cytoskeletal polymer networks: viscoelastic properties are determined by the microscopic interaction potential of cross-links. *Biophys. J.* **96**, 4725–4732 (2009).
54. Mueller, J. et al. Load adaptation of lamellipodial actin networks. *Cell* **171**, 188–200 e116 (2017).
55. Lo, C. M., Wang, H. B., Dembo, M. & Wang, Y. L. Cell movement is guided by the rigidity of the substrate. *Biophys. J.* **79**, 144–152 (2000).
56. Chen, X. et al. Predictive assembling model reveals the self-adaptive elastic properties of lamellipodial actin networks for cell migration. *Commun. Biol.* **3**, 616 (2020).
57. Kim, D. H. & Wirtz, D. Predicting how cells spread and migrate: focal adhesion size does matter. *Cell Adh. Migr.* **7**, 293–296 (2013).
58. D'Souza, R. S. et al. Calcium-stimulated disassembly of focal adhesions mediated by an ORP3/IQSec1 complex. *Elife* <https://doi.org/10.7554/eLife.54113> (2020).
59. Machaca, K. Ca<sup>2+</sup> signaling and lipid transfer 'pas a deux' at ER-PM contact sites orchestrate cell migration. *Cell Calcium* **89**, 102226 (2020).
60. Rothenberg, K. E. & Fernandez-Gonzalez, R. Forceful closure: cytoskeletal networks in embryonic wound repair. *Mol. Biol. Cell* **30**, 1353–1358 (2019).
61. Begnaud, S., Chen, T., Delacour, D., Mege, R. M. & Ladoux, B. Mechanics of epithelial tissues during gap closure. *Curr. Opin. Cell Biol.* **42**, 52–62 (2016).
62. Wood, W. et al. Wound healing recapitulates morphogenesis in *Drosophila* embryos. *Nat. Cell Biol.* **4**, 907–912 (2002).
63. Jumper, J. et al. Highly accurate protein structure prediction with AlphaFold. *Nature* **596**, 583–589 (2021).
64. Soliman, A. S. et al. EFhd2 brain interactome reveals its association with different cellular and molecular processes. *J. Neurochem.* <https://doi.org/10.1111/jnc.15517> (2021).
65. Laevsky, G. & Knecht, D. A. Cross-linking of actin filaments by myosin II is a major contributor to cortical integrity and cell motility in restrictive environments. *J. Cell Sci.* **116**, 3761–3770 (2003).
66. Vicente-Manzanares, M., Ma, X., Adelstein, R. S. & Horwitz, A. R. Non-muscle myosin II takes centre stage in cell adhesion and migration. *Nat. Rev. Mol. Cell Biol.* **10**, 778–790 (2009).
67. Abreu-Blanco, M. T., Verboon, J. M. & Parkhurst, S. M. Cell wound repair in *Drosophila* occurs through three distinct phases of membrane and cytoskeletal remodeling. *J. Cell Biol.* **193**, 455–464 (2011).
68. Dobin, A. et al. STAR: ultrafast universal RNA-seq aligner. *Bioinformatics* **29**, 15–21 (2013).
69. Love, M. I., Huber, W. & Anders, S. Moderated estimation of fold change and dispersion for RNA-seq data with DESeq2. *Genome Biol.* **15**, 550 (2014).
70. Bischof, J., Maeda, R. K., Hediger, M., Karch, F. & Basler, K. An optimized transgenesis system for *Drosophila* using germ-line-specific phiC31 integrases. *Proc. Natl Acad. Sci. USA* **104**, 3312–3317 (2007).
71. Spudich, J. A. & Watt, S. The regulation of rabbit skeletal muscle contraction. I. Biochemical studies of the interaction of the tropomyosin-troponin complex with actin and the proteolytic fragments of myosin. *J. Biol. Chem.* **246**, 4866–4871 (1971).
72. Platonova, E. et al. Single-molecule microscopy of molecules tagged with GFP or RFP derivatives in mammalian cells using nanobody binders. *Methods* **88**, 89–97 (2015).
73. Stephan, R., Gohl, C., Fleige, A., Klambt, C. & Bogdan, S. Membrane-targeted WAVE mediates photoreceptor axon targeting in the absence of the WAVE complex in *Drosophila*. *Mol. Biol. Cell* **22**, 4079–4092 (2011).
74. Bogdan, S., Grewe, O., Strunk, M., Mertens, A. & Klambt, C. Sra-1 interacts with Kette and Wasp and is required for neuronal and bristle. *Dev. Drosoph. Dev.* **131**, 3981–3989 (2004).
75. Stemmer, M., Thumberger, T., Del Sol Keyer, M., Wittbrodt, J. & Mateo, J. L. CCTop: an intuitive, flexible and reliable CRISPR/Cas9 target prediction tool. *PLoS ONE* **10**, e0124633 (2015).
76. Ran, F. A. et al. Genome engineering using the CRISPR-Cas9 system. *Nat. Protoc.* **8**, 2281–2308 (2013).
77. Brinkman, E. K., Chen, T., Amendola, M. & van Steensel, B. Easy quantitative assessment of genome editing by sequence trace decomposition. *Nucleic Acids Res.* **42**, e168 (2014).
78. Selden, L. A., Estes, J. E. & Gershman, L. C. The tightly bound divalent cation regulates actin polymerization. *Biochem. Biophys. Res. Commun.* **116**, 478–485 (1983).
79. Ruder, M., Nagel, B. M. & Bogdan, S. Analysis of cell shape and cell migration of *drosophila* macrophages in vivo. *Methods Mol. Biol.* **1749**, 227–238 (2018).
80. Litschko, C., Damiano-Guercio, J., Bruhmann, S. & Faix, J. Analysis of random migration of *Dictyostelium* amoeba in confined and unconfined environments. *Methods Mol. Biol.* **1749**, 341–350 (2018).

### Acknowledgements

We thank the Bloomington Stock Center and VDRC for fly stocks, K. Ramlow for purifying and testing *Drosophila* anti-Swip-1 antibodies, A. Hirschhäuser for isolating the macrophages for bulk RNA seq analysis, T. Kaufmann for support in interpretation of structural data, and D. Mielenz for providing the rabbit anti-mouse EFhd2/Swip-1 antibody and human EFhd2 cDNA. The work was supported by grants to S.B. (BO1890/4-1) and J.F. (Fa330/9-2) from the Deutsche Forschungsgemeinschaft (DFG) and by J.G. from the VW Stiftung, "Big Data in den Lebenswissenschaften der Zukunft", Nr. A129197.

### Author contributions

S.B. and J.F. designed the project, made the figures, and wrote the manuscript. F.L. performed all *Drosophila* experiments. T.P. performed all B16-F1 mouse melanoma work and biochemical in vitro experiments. S.P. performed the bulk RNA seq analysis. G.S. and J.G. managed and coordinated RNA seq analysis. K.R. performed bioinformatical analyses. All authors commented on the manuscript.

### Funding

Open Access funding enabled and organized by Projekt DEAL.

### Competing interests

The authors declare no competing interests.

### Additional information

**Supplementary information** The online version contains supplementary material available at <https://doi.org/10.1038/s41467-022-30167-0>.

**Correspondence** and requests for materials should be addressed to Sven Bogdan.

**Peer review information** *Nature Communications* thanks Johanna Ivaska, George Langford, and the other anonymous reviewer(s) for their contribution to the peer review of this work. Peer reviewer reports are available.

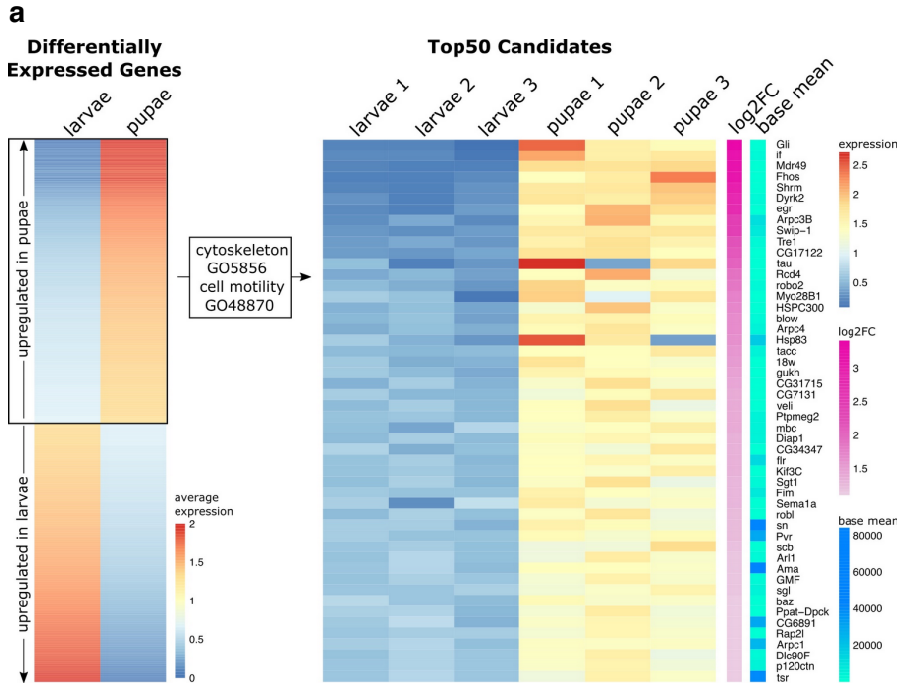
**Reprints and permission information** is available at <http://www.nature.com/reprints>

**Publisher's note** Springer Nature remains neutral with regard to jurisdictional claims in published maps and institutional affiliations.



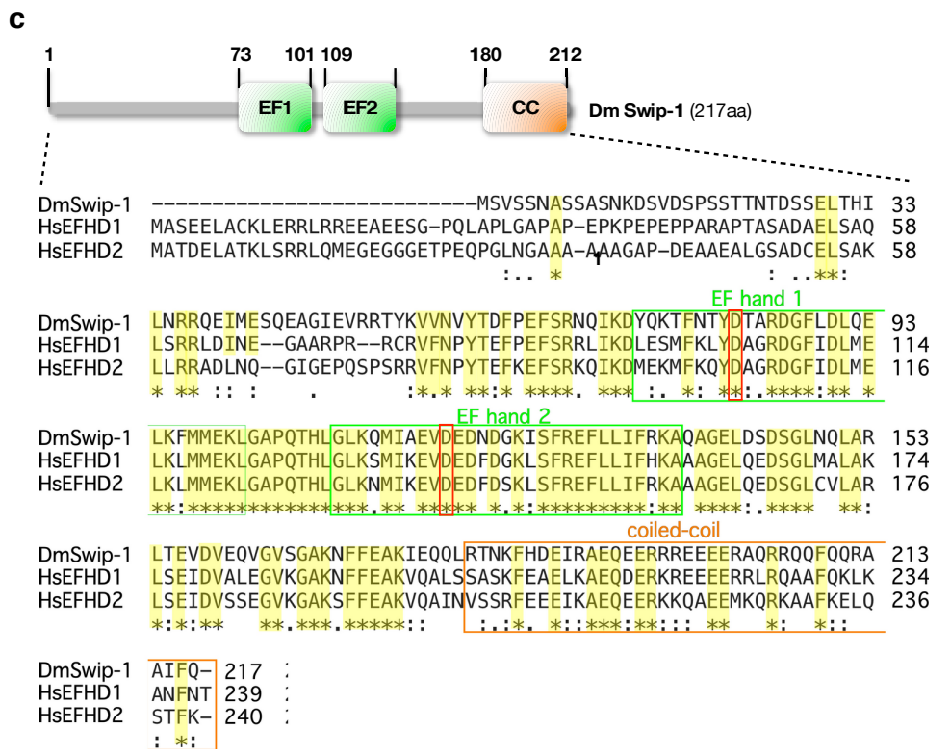
**Open Access** This article is licensed under a Creative Commons Attribution 4.0 International License, which permits use, sharing, adaptation, distribution and reproduction in any medium or format, as long as you give appropriate credit to the original author(s) and the source, provide a link to the Creative Commons license, and indicate if changes were made. The images or other third party material in this article are included in the article's Creative Commons license, unless indicated otherwise in a credit line to the material. If material is not included in the article's Creative Commons license and your intended use is not permitted by statutory regulation or exceeds the permitted use, you will need to obtain permission directly from the copyright holder. To view a copy of this license, visit <http://creativecommons.org/licenses/by/4.0/>.

© The Author(s) 2022



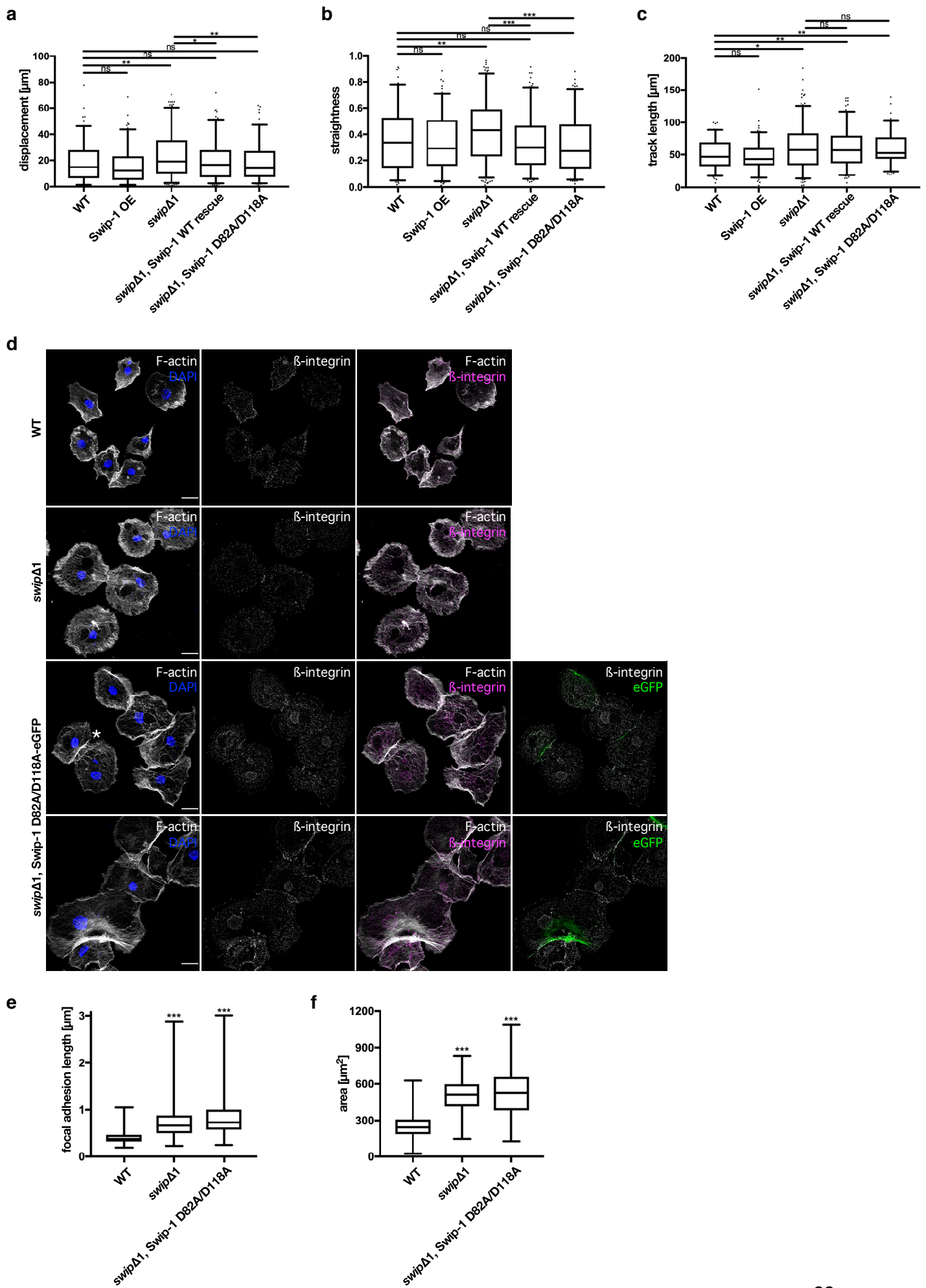
**b**

flybase gene ID	gene name	known/predicted molecular function	log2FC
FBgn0266084	<i>fhos</i>	actin filament bundling/nucleator	3.16
FBgn0085408	<i>shrm</i>	actin filament binding	2.97
FBgn0065032	<i>arpc3B</i>	Arp2/3 subunit	2.46
FBgn0032731	<i>swip-1</i>	actin filament binding	2.46
FBgn0028371	<i>jbug</i>	filamin	2.31
FBgn0040299	<i>myo28B1 (myoVIIb)</i>	motor protein	1.75
FBgn0061198	<i>HSPC300</i>	WRC subunit	1.71
FBgn0284255	<i>arpc4</i>	Arp2/3 subunit	1.65
FFBgn0051715	<i>CG31715</i>	actin filament capping	1.46
FBgn0260049	<i>Flr (aip)</i>	actin filament binding	1.33
FBgn0024238	<i>fim</i>	actin filament crosslinking	1.28
FBgn0003447	<i>sn</i>	actin filament crosslinking	1.25



**Supplementary figure S1:** Swip-1 – a pro-migratory gene conserved between flies and humans

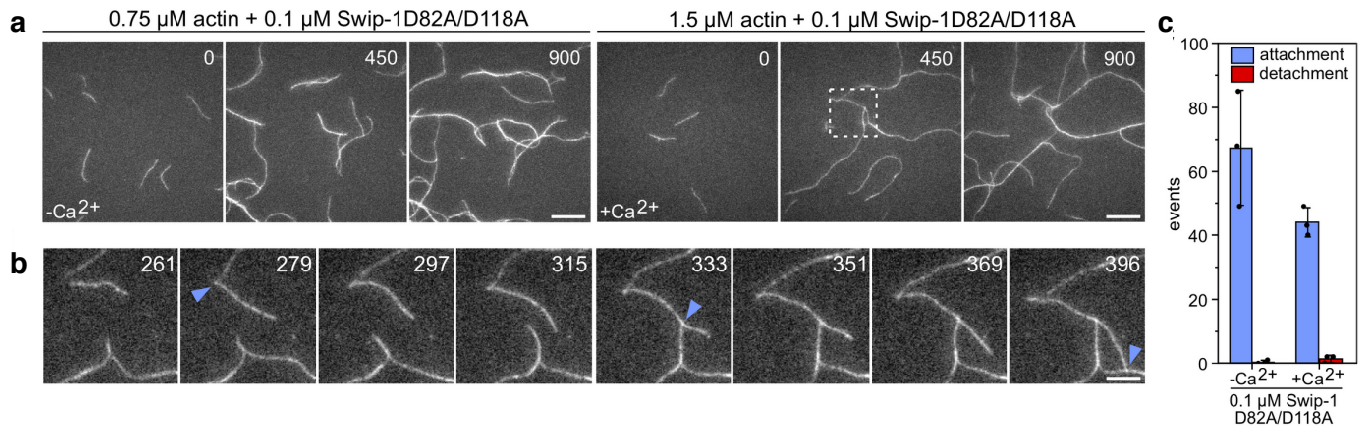
**(a)** Heatmap showing average expression of all differentially expressed genes in larval and prepupal hemocytes. We selected genes in the GO-terms cytoskeleton (GO:0005856) and cell motility (GO:0048870) in order to identify novel pro-migratory candidates. The expression per replicate, log<sub>2</sub>FoldChanges and base means of the 50 genes with the highest log<sub>2</sub>FoldChange, upregulated in prepupae are shown on the right. **(b)** Selected up-regulated cytoskeletal genes with Fold-changes of larval versus prepupal macrophages. **(c)** Schematic of the *Drosophila* EFhD2/Swip-1. A sequence alignment between *Drosophila* EFhD2/Swip-1 and the two known human homologues, EFhD1/Swip-2 and EFhD2/Swip-1 is shown. The conserved EF domains and the subsequent coiled-coil regions (orange) are highlighted. The highly conserved aspartate residues of both EF-loops mutated in EFhD1/Swip-1-D82A/D118A are marked by red boxes. Identical residues are marked by an asterisk.





**Supplementary figure S2: Loss of Swip-1 impairs cell migration and focal adhesion turnover of macrophages**

**(a)** Quantification of track displacement, **(b)** track straightness calculated as the ratio of track displacement to track length and **(c)** track length. n= WT: 114, OE: 133, swip-1 mutant: 206, rescue WT: 166, rescue Swip-1-D82A/D118A: 136 tracks. Boxes indicate 50% (25-75%) and whiskers (5-95%) of all measurements, with black lines depicting the medians. For statistical analysis, two values indicated by connecting black lines were compared with two-sided Mann-Whitney test, P value: 0.12 (ns), 0.033 (\*), 0.002 (\*\*), <0.001 (\*\*\*). **(d)** Maximum intensity projection of confocal images of pupal wild-typic, mutant and mutant macrophages re-expressing GFP-tagged calcium binding mutant Swip-1 variant under the control of the hemoelectin-Gal4 driver plated on vitronectin coated cover slips. Scale bars represent 10  $\mu$ m. Cells were co-stained with anti- $\beta$ -integrin antibody (white/magenta), DAPI (blue) and phalloidin (white). The asterisk marks a contact site of two macrophages enriched in  $\beta$ -integrin staining and Swip-1-D82A/D188A-eGFP localization. Images shown are representative of two independent experiments. **(e)** Length of randomly chosen focal adhesions (FA) marked by anti- $\beta$ -integrin staining in the lamellipodia were measured in a single z-plane using Image J. n= WT: 443 FA of 26 macrophages, swip-1 mutant: 645 FA of 41 macrophages, calcium-binding mutant Swip-1-D82A/D118A: 573 FA of 35 macrophages. **(f)** Cell size of single wild type, mutant and mutant macrophages re-expressing GFP-tagged calcium binding mutant Swip-1 variant was measured using Image J Analyze particles macro. n= WT: 65, swip-1 mutant: 60, calcium-binding mutant Swip-1-D82A/D118A: 59 macrophages. (e, f) Boxes indicate 50% (25-75%) and whiskers minimum and maximum of all measurements, with black lines depicting the medians. Two-sided Mann-Whitney test was used, P value: <0.001 (\*\*\*).



**Supplementary figure S3:** *Drosophila* Swip-1-D82A/D118A maintains stable cross-links in the presence of calcium.

**(a)** Time-lapse micrographs of TIRFM assays, used for analysis of cross-linking behavior of the Swip-1-D82A/D118A EF-hand mutant in the absence or presence of 1 mM Ca<sup>2+</sup>. Polymerization of 0.75 or 1.5  $\mu\text{M}$  G-actin (10% ATTO488-labelled) with 0.1  $\mu\text{M}$  *Drosophila* Swip-1 D82A/D118A in the absence and presence of Ca<sup>2+</sup> as indicated. Note significantly cross-linked networks in the absence of Ca<sup>2+</sup> as compared to assay conditions in the presence of Ca<sup>2+</sup>. **(b)** Enlarged gallery of inset (dashed box in a) displays stable cross-linking behavior of 0.1  $\mu\text{M}$  *Drosophila* Swip-1 D82A/D118A in the presence of Ca<sup>2+</sup> at higher temporal resolution. Blue arrowhead marks a newly formed cross-link. Time is given in seconds in the upper right corner of each frame. Scale bars, 10  $\mu\text{m}$ . **(c)** Quantification of attachment and detachment event in the absence or presence of Ca<sup>2+</sup>. Bars represent mean  $\pm$  SD from three movies each (n=3). Data points show the measured values of the experiments.

## **2.2 Publication 2 (under review)**

submitted to Development

EFhD2/Swip-1 promotes exocytosis of glue granules in the exocrine *Drosophila* salivary gland.

Franziska Lehne & Sven Bogdan

1 **EFhD2/Swip-1 promotes exocytosis of glue granules in the exocrine *Drosophila***  
2 **salivary gland**

3

4 Franziska Lehne<sup>1</sup> and Sven Bogdan<sup>1\*</sup>

5

6 <sup>1</sup> Institute of Physiology and Pathophysiology, Dept. of Molecular Cell Physiology,

7 Philipps-University Marburg, Germany

8

9

10 \*) to whom correspondence should be addressed

11 [sven.bogdan@staff.uni-marburg.de](mailto:sven.bogdan@staff.uni-marburg.de)

12

13

14 *Key words*

15 EFhD2/Swip-1, *Drosophila*, salivary gland, exocytosis, actin, cross-linker, calcium, EF-

16 hand, secretion

17 **Abstract** (167 words)

18

19 Exocytosis is a fundamental cellular process by which cells secret cargos from their  
20 apical membrane into the extracellular lumen. Cargo release proceeds in sequential  
21 steps that depend on a coordinated assembly and organization of an actin cytoskeletal  
22 network. Here, we identified the conserved actin-crosslinking protein EFhD2/Swip-1 as  
23 a novel regulator controlling exocytosis of glue granules in the *Drosophila* salivary  
24 gland. Real-time imaging revealed that EFhD2/Swip-1 is simultaneously recruited with  
25 F-actin onto secreting granules in proximity to the apical membrane. EFhD2/Swip-1 is  
26 rapidly cleared at the point of secretory vesicle fusion and colocalizes with actomyosin  
27 network around the fused vesicles. Loss of EFhD2/Swip-1 function impairs secretory  
28 cargo expulsion resulting in strongly delayed secretion. Remarkably, rescue  
29 experiments further suggest that dimerization but not calcium-binding is crucial for  
30 EFhD2/Swip-1 function in regulated exocytosis. Thus, our results uncover a novel role  
31 of EFhD2/Swip-1 in secretory vesicle compression and expulsion of cargo during  
32 regulated exocytosis. We propose that cross-linking activity contributes synergistically  
33 to actin-myosin driven coat compression by promoting actin filament sliding.

34 **Introduction** (494 words)

35

36 Regulated exocytosis is an important mechanism by which secretory cells package  
37 molecules in secretory vesicles and deliver them to the extracellular environment. It is  
38 a stepwise process that involves the biogenesis of secretory vesicles, the transport to  
39 the cell periphery, their fusion with the apical membrane and the release of vesicle  
40 content to the outside (Burgoyne and Morgan, 2003; Spiliotis and Nelson, 2003; Wu et  
41 al., 2014). These processes highly depend on a cortical actin cytoskeleton that forms  
42 a dense network associated with the plasma membrane (Nightingale et al., 2012;  
43 Porat-Shliom et al., 2013). Previous studies showed distinct functions of the actin  
44 cortex in regulated exocytosis (Nightingale et al., 2012; Trifaro et al., 2008). Secretory  
45 vesicles form an actin coat that acts as a physical barrier preventing premature vesicle  
46 fusion, but also together with myosin II providing the mechanical forces for vesicle  
47 compression and expulsion of cargo into the extracellular lumen (Masedunskas et al.,  
48 2011; Nightingale et al., 2011; Sokac et al., 2003).

49

50 The *Drosophila* salivary gland is a typical exocrine gland consisting of two  
51 interconnected monolayered tubes with columnar epithelial cells on each side that  
52 secrete high levels of glue proteins, important for the attachment of the pupa to a  
53 surface, but also release glycosylated mucin or non-digestive enzymes for lubricating  
54 food (Abrams et al., 2003; Biyasheva et al., 2001). More recent studies further  
55 established the *Drosophila* salivary gland as a powerful *ex vivo* 3D imaging model  
56 system to dissect the molecular mechanism of the actin coat formation and  
57 actomyosin-dependent vesicle compression of single exocytic events at high-  
58 resolution (Rousso et al., 2016; Tran et al., 2015). Both studies provided strong  
59 evidence for essential roles of branched actin nucleators such as the Arp2/3-complex  
60 and its activator WASP in the process of secretory cargo expulsion and integration of  
61 vesicular membranes with the apical plasma membrane (Rousso et al., 2016; Tran et  
62 al., 2015). Secretion is initiated by the clearance of apical F-actin at the plasma  
63 membrane, followed by fusion pore formation and the subsequent directional F-actin  
64 recruitment to the fused secretory vesicle membrane (Merrifield, 2016; Tran and Ten  
65 Hagen, 2017). Actin assembly on the vesicular membrane is driven by sequential  
66 recruitment of actin nucleators. It starts with the recruitment of Diaphanous and its  
67 activator Rho promoting nucleation of linear actin filaments on vesicle surface, followed

68 by Arp2/3/WASP-branched actin polymerization, first preventing premature vesicle  
69 fusion, but eventually promoting myosin II dependent vesicle compression and  
70 expulsion (Merrifield, 2016; Tran and Ten Hagen, 2017).

71 Here, we identified the conserved actin cross-linking protein EFhD2/Swip-1 as a novel  
72 regulatory component of exocytosis in *Drosophila* salivary glands. EFhD2/Swip-1 is  
73 recruited to secreting granules in proximity to the apical membrane. EFhD2/Swip-1 is  
74 rapidly cleared at the point of secretory vesicle fusion and colocalizes with the actin  
75 cytoskeleton network around the fused vesicles. Loss of EFhD2/Swip-1 function  
76 impairs secretory cargo expulsion resulting in strongly delayed secretion. Our data  
77 further suggest that dimerization but not calcium-binding is crucial for EFhD2/Swip-1's  
78 function in regulated exocytosis.

79

80 **Results** (1204 words)

81

82 **Swip-1 is highly expressed in salivary gland tissue and accumulates at fused**  
83 **secretory vesicles upon ecdysone induction**

84

85 We have recently identified the EF-hand domain containing protein EFhD2/Swip-1 as  
86 a conserved lamellipodial protein strongly upregulated in *Drosophila* macrophages at  
87 the onset of metamorphosis when macrophage behavior shifts from quiescent to  
88 migratory state by the steroid hormone (20E) ecdysone (Lehne et al., 2022). Gene  
89 expression data extracted from Fly Atlas 2 (Leader et al., 2018) and the Human Protein  
90 Atlas (Uhlen et al., 2015) further suggest an unknown conserved role of EFhD2/Swip-  
91 1 in exocrine glandular cells of the gastrointestinal tract and salivary glands. We used  
92 *ex vivo* cultured *Drosophila* third instar larval salivary glands (SG) as an excellent  
93 model system to study the role of Swip-1 in exocytosis (Figure 1A; (Loganathan et al.,  
94 2021). Exocrine salivary glands can be cultured *ex vivo* in a Petri dish and stimulated  
95 to secrete highly glycosylated mucins, so-called glue proteins by exogenous addition  
96 of 20E (Figure 1A; (Costantino et al., 2008; Tran et al., 2015). Glue proteins are stored  
97 in large secretory vesicles and are released to the salivary gland lumen upon fusion  
98 with the apical plasma membrane (Figure 1A).

99 Western blot analysis confirmed a prominent expression of Swip-1 in wild type salivary  
100 glands from third instar larvae (Figure 1B). Before secretion, SG cells become packed  
101 with numerous glue granules with a relatively homogenous diameter of around 5  $\mu\text{m}$ ,

102 leaving only little space for the cytoplasm (Figure 1C). Endogenous Swip-1 protein  
103 mainly localized in the cytoplasm that forms a reticulated pattern around large glue  
104 granules (Figure 1C’). In secretory SG cells, however, endogenous Swip-1 became  
105 dramatically enriched at fused granules and co-localized with the F-actin that forms a  
106 coat on secretory vesicles as one of the early events in the secretory process (Figure  
107 1D; (Rouso et al., 2016; Tran et al., 2015)). Similarly, an eGFP-tagged Swip-1 protein  
108 expressed by the *srp*-Gal4 driver selectively marked fused secretory vesicles co-  
109 localizing with F-actin (Figure 1F). Live-imaging of eGFP-tagged Swip-1 highlighted its  
110 dynamic localization in the early secretory process (Figure 2A; supplementary movie  
111 M1). Swip-1 first localized along the apical membrane, became cleared at the point of  
112 vesicle fusion and formed a coat on the vesicle only after fusion to the apical membrane  
113 as similarly reported for F-actin (Figure 2A’; supplementary movie M1). Live-imaging  
114 of eGFP-Swip-1 together with LifeAct-Ruby further revealed that Swip-1 and F-actin  
115 localized simultaneously on secretory vesicles (Figure 2B; supplementary movie M2).  
116 As shown in figure 2C, the average time in the detection of Swip-1 and LifeAct was -  
117  $1.3s \pm 14.4s$  and thus largely identical. Therefore, Swip-1 is seen on granules before  
118 Arp3 recruitment as previously measured (average time difference:  $29 \pm 14s$  (Tran et  
119 al., 2015)). Additional time-lapse co-labeling analyses using LifeAct with the non-  
120 muscle myosin II marker (Zip-GFP) or the WASP-like protein WHAMY (Brinkmann et  
121 al., 2016) further confirmed their later recruitment to the membrane of fused vesicles  
122 compared to Swip-1. The average time differences in the detection of F-actin relative  
123 to WHAMY and to myosin II were  $23.4s \pm 13.8s$  and  $55.2s \pm 31.4s$ , respectively (Figure  
124 2D).

125

### 126 **Loss of EFhd2/Swip-1 function impairs salivary gland secretion**

127

128 To further investigate whether Swip-1 function is required for regulated exocytosis, we  
129 next analyzed *swip-1* null mutants which have been recently described (Lehne et al.,  
130 2022; figure 1B). To evaluate exocytosis of SG cells quantitatively, we first analyzed  
131 the secretion of the chitin-binding domain of Serpentine tagged with GFP (UAS-  
132 SerpCBD-GFP), a well-established marker to measure apical secretion (Luschnig et  
133 al., 2006). Before secretion, SerpCBD-GFP was exclusively detected in SG cells, while  
134 in secretory glands increasing levels of the fluorescent marker were released into the  
135 lumen within the first four hours after 20E treatment (Figure 3A). By contrast, *swip-1*



136 null mutant salivary glands showed a striking delayed secretion, and even after eight  
137 hours post treatment only half of the mutant glands became secretory (Figure 3B).  
138 Impaired secretion of *swip-1* mutant SGs was fully rescued by re-expression of a full-  
139 length Swip-1 transgene (Figure 3B). Interestingly, calcium levels were elevated after  
140 2 hours of 20E treatment (Biyasheva et al., 2001), prompting us to test whether the  
141 function of Swip-1 depends on its calcium-binding ability. Remarkably, we found that  
142 re-expression of Swip-1 protein deficient for calcium binding (Swip-1-D82A/D118A),  
143 but not a deletion construct lacking the coiled-coil domain (Swip-1- $\Delta$ CC) could  
144 substantially rescue impaired mutant secretion (Figure 3B). Taken together, these data  
145 indicate that appropriate SG secretion requires dimerization of Swip-1 mediated by its  
146 coiled-coil domain but not functional calcium-binding.

147

#### 148 **EFhD2/Swip-1 function is not required for secretory vesicle fusion, but rather for** 149 **cargo expulsion**

150

151 EFhD2/Swip-1 has been previously found to accumulate transiently in the foci of  
152 fusion-competent myoblasts in *Drosophila* suggesting a possible role of EFhD2/Swip-  
153 1 in the breakdown of the prefusion complex during myoblast fusion (Hornbruch-  
154 Freitag et al., 2011). To assess a possible impact of EFhD2/Swip-1 in secretory vesicle  
155 fusion, we analyzed the time between membrane fusion (fusion pore formation) and  
156 actin recruitment to the secretory vesicles by infusing a small molecular weight  
157 fluorescent dextran (10 kDa) into the lumens of SGs expressing LifeAct-GFP (Tran et  
158 al., 2015). Fluorescent dextran entered the vesicle immediately upon fusion before an  
159 F-actin coat marked by LifeAct-GFP was detected on vesicle membranes (Figure 3D,  
160 E; supplementary movie M3). Comparative analysis of wild type and mutant SG cells  
161 revealed no significant differences in the time between dextran diffusion into the  
162 vesicles and F-actin coat formation (Figure 3F, G). The average time difference in the  
163 detection of dextran relative to F-actin in wild type and mutant cells were  $53.8 \pm 42.9$  s  
164 and  $49.4 \pm 42.8$  s, respectively (Figure 3H). Thus, these data imply that impaired  
165 secretion observed in mutant SGs is not accompanied with a defective vesicle fusion.  
166 Intrigued by its established cross-linking activity (Lehne et al., 2022), we further  
167 investigated whether EFhD2/Swip-1 is involved in late events in the secretory process  
168 such as cargo expulsion that requires a dense contractile actin network. To better  
169 monitor the complete process of apical vesicle secretion, we imaged salivary glands

170 expressing a GFP-fused glue protein (Sgs3-GFP) that labels vesicle cargo and allows  
171 us to better visualize the shape and dynamics of vesicles during secretion (Figure 3 I,  
172 I'). Co-labelling with LifeAct-Ruby revealed that granules properly fused with the apical  
173 plasma membrane in *swip-1* mutant SG cells, but often failed to collapse and secrete  
174 their contents into the lumen (Figure 3J) as previously observed upon knockdown of  
175 Arp2/3-branched actin nucleators (Tran et al., 2015). Quantification further confirmed  
176 that the duration of size reduction and thereby cargo release was significantly  
177 prolonged in *swip-1* mutant cells, more than twice long as compared to wild type (WT  
178 152.9 +/- 56.5s versus *swip* $\Delta$ 1: 368.0 +/- 177.6s; Figure 3J, K). Similar to previous  
179 *Arp2* knockdown studies (Roussio et al., 2016), active Myosin II (detected by an anti-  
180 phospho-MLCK antibody) was still recruited to fused vesicles in *swip* $\Delta$ 1 mutants  
181 (Figure 4A). By contrast, the level of active myosin II appeared to be rather increased  
182 compared to wild type (Figure 4A). Thus, it is unlikely that a reduced myosin II  
183 recruitment causes an inefficient vesicle compression and secretion as observed in  
184 *swip* $\Delta$ 1 mutants.

185 Taken together, our studies identified a novel function of EFhD2/Swip-1 in regulating  
186 secretory cargo expulsion during regulated exocytosis (Figure 4B, C).

187

## 188 **Discussion** (713 words)

189

190 EFhD2/Swip-1 has been described as a conserved calcium-regulated actin-binding  
191 protein, which is broadly expressed in different cells and tissues across species and  
192 involved in diverse cellular functions ranging from immune defense, cell migration and  
193 endocytosis (Huh et al., 2013; Huh et al., 2015; Kwon et al., 2013; Moreno-Layseca et  
194 al., 2021; Tu et al., 2018). However, a role of EFHD2/Swip-1 in exocytosis has not yet  
195 been reported.

196 Exocytosis is an actin-driven sequential process by which proteins are delivered in  
197 membranous secretory vesicles to the extracellular space, either constitutively or upon  
198 stimulation, called regulated exocytosis. Regulated exocytosis of salivary gland glue  
199 mucins is stimulated by a short pulse of the steroid hormone 20-hydroxyecdysone  
200 (20E) in early third instar larvae (Biyasheva et al., 2001). Glue proteins are initially  
201 stored in large secretory vesicles and then released into the lumen upon a second  
202 pulse of 20E at the end of the third larval instar. Initial experiments with Aequorin, a  
203 calcium-activated photoprotein further suggested that this premetamorphic ecdyson

204 pulse leads to an increase of calcium by a genomic mechanism and that increased  
205 calcium levels are required for salivary gland secretion (Biyasheva et al., 2001). Given  
206 that transient calcium bursts reduce EFhD2/Swip-1 cross-linking activity and thereby  
207 promote rapid reorganization of existing actin networks (Lehne et al., 2022), we initially  
208 suggested that increased calcium levels might also trigger actin remodeling during  
209 regulated exocytosis of salivary glands. By using genetically encoded calcium  
210 reporters (GCaMP6/RCaMP1), however, we could not detect any changes in  
211 intracellular calcium levels after 20E treatment (data not shown). In addition, neither  
212 induced release of intracellular stored calcium by thapsigargin treatment nor  
213 intracellular or extracellular calcium depletion by BAPTA-AM or EGTA treatment  
214 affected 20E-induced secretion of cultured salivary glands (data not shown). Thus,  
215 glue granule exocytosis into the salivary gland lumen does not simply depend on  
216 calcium changes as previously suggested (Biyasheva et al., 2001). These data are  
217 also consistent with the observation that calcium binding is not required for  
218 EFhD2/Swip-1 function in exocytosis. Different from its requirement during epithelial  
219 wound closure (Lehne et al., 2022), we found that re-expression of the Swip-1-  
220 D82A/D118A transgene substantially rescues exocytosis defects of *swip-1* deficient  
221 SGs. Our rescue experiments rather indicate that dimerization of EFhD2/Swip-1 is an  
222 essential mechanism to cross-link actin filaments around the secretory vesicles. Cross-  
223 linking of actin filaments might further stabilize the Arp2/3-branched actin network and  
224 thereby contributes to the formation of the dense actomyosin cortex (see model in  
225 figure 4C, D). Thus, we hypothesized that EFhD2/Swip-1 contributes to the formation  
226 of a dense cortical actin filament texture mediating the force for proper vesicle  
227 compression and expulsion of cargo. Consistent with this proposed function, we  
228 observed granules in *swip-1* mutant cells that fused with the apical membrane, but  
229 then failed to completely secrete cargo or only after a significant delay (see figure 3K).  
230 Destabilization of the actin cortex in *swip-1* mutant might also compromise the myosin  
231 II function that forms a "cage"-like structure on fused secretory vesicles (Rousso et al.,  
232 2016). In addition, we further suggest that Swip-1 cross-linking activity might also  
233 contribute directly to actin coat compression by promoting actin filament sliding as  
234 recently proposed for the cross-linker  $\alpha$ -actinin in surfactant secretion in primary  
235 alveolar type II cells (Miklavc et al., 2015). According to this model, actin  
236 depolymerization and cross-linking join forces with myosin II to contract actin coats on  
237 fused secretory vesicles (Miklavc et al., 2015). Consistent with this model, both

238 inhibition of myosin function (Rousso et al., 2016) or loss of cross-linking by Swip-1  
239 only result in a two-fold reduction in SG secretion.

240 In summary, we identified a novel function of the conserved cross-linker EFhD2/Swip-  
241 1 in regulated exocytosis. The function of EFhD2/Swip-1 in secretory cells might be  
242 conserved between flies to humans as previously described for immune cell migration  
243 and wound closure (Lehne et al., 2022; Tu et al., 2018). Human EFhD2/Swip-1 has  
244 been found in a number of pathophysiological conditions and has been proposed as a  
245 potential biomarker for chronic diseases, including diseases associated with synaptic  
246 dysfunction (Kogias et al., 2019; Mielenz and Gunn-Moore, 2016; Thylur et al., 2018).  
247 However, the role of EFhD2/Swip-1 in pathogenesis and the underlying molecular  
248 mechanism are not well-understood. Thus, future studies are expected to dissect the  
249 pathophysiological role of EFhD2/Swip-1 in more specialized types of exocytosis,  
250 including synaptic transmission.

251

## 252 **Experimental procedures**

253

### 254 ***Drosophila genetics***

255 Fly husbandry and crossing were carried out according to the standard methods. All  
256 crosses were performed at 29°C. The following fly stocks were obtained from the  
257 Bloomington stock center: w[1118] (BL3605), y[1] w[\*]; Mi{Trojan-Gal4.0}ptc[Mi02003-  
258 TG4.0] (BL67438), P{w[+mC]=UAS-LifeAct.GFP.W}3 (BL57326), y[1] w[\*]; P{y[+\*]  
259 w[+mC]=UAS-LifeAct-Ruby}VIE-19A (BL35545), w[\*]; P{w[+mC]=Sgs3-GFP}3  
260 (BL5885), w[\*]; P{w[+mC]=PTT-GC}zip[CC01626]/SM6a (BL51564). The srp-Gal4  
261 stock was a kind gift of the D. Siekhaus lab. The w[+];UAS-serp-CBD-GFP stock was a  
262 kind gift of the M. Brankatschk lab. Transgenic UAST-Whamy-eGFP (Brinkmann et al.,  
263 2016), UAST-Swip-1-eGFP, UAST-eGFP-Swip-1, UAST-Swip-1-D82A/D118A-eGFP  
264 and UAST-Swip-1-ΔCC-eGFP flies were generated using ΦC31- mediated  
265 transgenesis (y[1] M{vas-int.Dm}ZH2A w[\*]; M{3xP3-RFP.attP'}ZH-86Fb (BL24749)  
266 and y[1] M{vas-int.Dm}ZH2A w[\*]; M{3xP3-RFP.attP'}ZH-68E (BL24485) (Bischof et  
267 al., 2007). The *swipΔ1* mutant was generated by CRISPR/Cas9 of the following target  
268 sequence: 5'-GGGGTCTTCGAGAAGACCT-3' (Lehne et al., 2022). Loss of the  
269 EFhD2/Swip-1 protein was confirmed by Western blot analysis stained against His-  
270 Swip-1 (Pineda, Berlin).

271

272 **Antibody generation**

273 The rabbit anti-EFhD2/Swip-1 antibody was generated against the full-length  
274 *Drosophila* Swip-1 fused to a 6xHis-tag (pDEST17, ThermoFisher Scientific). The  
275 6xHis-Swip-1 fusion protein was expressed in *E. coli* and purified with Ni-NTA resin  
276 (GE Healthcare). Rabbits were immunized with purified proteins by Pineda Antikörper-  
277 service (Berlin, Germany).

278

279 **Immunohistochemistry and fluorescence staining**

280 For antibody staining, salivary glands of third instar wandering larvae were isolated in  
281 1x PBS, fixed in 4% formaldehyde in phosphate buffer pH 7.4, washed and blocked  
282 with 5mg/ml BSA in 50mM Tris-HCl pH 7.4 + 0.5% Nonidet P-40 and the EFhD2/Swip-  
283 1 antibody (1:5000 dilution) was incubated overnight. The primary antibody was  
284 visualized with polyclonal Alexa Fluor-568-conjugated goat-anti-rabbit antibody  
285 (1:1000 dilution; #A11036, Invitrogen). Active myosin II was detected by using the anti-  
286 phospho-Myosin Light Chain 2 (Ser19) Antibody (Cell Signaling #3671, 1:20 dilution).  
287 F-actin was visualized using Alexa Fluor-488-conjugated Phalloidin (1:100 dilution,  
288 #A12379, Invitrogen) and nucleus by DAPI staining (1µg/mL, #62248, Thermo  
289 Scientific). For only staining of F-actin and nucleus, dissected glands were fixed in 4%  
290 paraformaldehyde in 1xPBS, washed once with 1x PBS+0.5% TritonX-100, washed  
291 three times with 1xPBS and stained with Alexa Fluor-488-conjugated Phalloidin (1:100  
292 dilution, #A12379, Invitrogen) and DAPI (1µg/mL, #62248, Thermo Scientific). Glands  
293 were mounted in Fluoromount-G Mounting Medium (Invitrogen).

294

295 **Validation of knock-out of EFhD2/Swip-1**

296 EFhD2/Swip-1 null mutants were validated by isolating 20 salivary glands from third  
297 instar wandering larvae, removing of the fat body, squashing the glands in 15µL 2x  
298 SDS sample buffer and incubation at 95°C for 10min for SDS-PAGE. The following  
299 antibodies were used for Western Blot analysis: anti- EFhD2/Swip-1 (1:5000), Anti-  
300 Actin AB-5 (BD Biosciences), Goat anti-Rabbit IgG (H+L)-HRP and Goat anti-Mouse  
301 IgG (H+L)-HRP (Invitrogen).

302

303 **Quantification of exocytosis**

304 To quantify the onset of exocytosis, salivary glands of third instar wandering larvae  
305 expressing UAS-Serp-CBD-GFP under the control of srp-Gal4 driver were dissected

306 and placed in 100 $\mu$ L Schneider's *Drosophila* medium in a humidified chamber. Under  
307 a Leica DFC7000 T stereomicroscope equipped with a UV-Lamp (Excelitas  
308 Technologies), glands were assessed for GFP fluorescence in their lumen as a  
309 parameter for entered secretory state. Initially, salivary glands already secreting were  
310 discarded. Exocytosis was induced by adding 1mM of 20-Hydroxyecdysone (Sigma)  
311 to the medium. Glands were continuously assessed every hour for 8h post induction.  
312 Inconsistent fluorescence throughout the gland was considered as sign of apoptosis  
313 and respective glands discarded. Percentages of non-secretory and secretory glands  
314 were calculated for every time point.

315

### 316 ***Fluorescence microscopy***

317 Confocal images were taken with a Leica TCS SP8 with an HC PL APO CS2 40x/1.4  
318 oil objective. Live imaging of ex vivo larval salivary glands was performed using a Zeiss  
319 CellObserver Z.1 with a Yokogawa CSU-X1 spinning disc scanning unit and an  
320 Axiocam MRm CCD camera (6.45  $\mu$ m x 6.45  $\mu$ m).

321

### 322 ***Live-cell imaging of larval salivary glands***

323 Live imaging of larval salivary glands was performed as previously reported (Tran et  
324 al., 2015). In short, isolated glands were placed in a glass bottom imaging dish,  
325 covered with a Isopore 0.1 $\mu$ m PC membrane (Merck) and 50 $\mu$ L of Schneider's  
326 *Drosophila* medium. Dissected glands were imaged with a Zeiss CellObserver Z.1 with  
327 a Yokogawa CSU-X1 spinning disc scanning unit and an Axiocam MRm CCD camera  
328 (6.45  $\mu$ m x 6.45  $\mu$ m). For additional Dextran imaging, dissected glands were incubated  
329 for 1h with 200 $\mu$ M Dextran-Alexa568 (MW 10000, Invitrogen) in Schneider's  
330 *Drosophila* medium, washed three with medium and then placed on an imaging  
331 chamber as described above. For 4D movie reconstructions of fusing vesicles the  
332 surface module in Imaris 9.3 (Bitplane) software were used.

333 Measurement of percent fluorescent intensity of LifeAct/Swip-1, LifeAct/WHAMY,  
334 LifeAct/zip and LifeAct/Dextran was performed as previously described (Tran et al.,  
335 2015). In short, an oval region of interest was drawn around single fusing vesicles in  
336 one z-plane. The "plot z-axis profile" function in ImageJ was used to obtain  
337 fluorescence intensity values for each channel. Subsequent calculations of %  
338 fluorescence intensity and time difference of detection were carried out in Microsoft  
339 Excel according to Tran and colleagues. Accordingly, measurement of time of cargo

340 expulsion was determined by calculating the time difference between detection of  
341 LifeAct and minimal Sgs3 fluorescence in the region of interest.

342

### 343 **Statistical analysis**

344 Quantitative experiments were performed at least in four replicates to avoid any  
345 possible bias by environmental effects or unintentional error. Exact numbers of  
346 replicates are specified in figure legends. Raw data were processed in Excel  
347 (Microsoft). Statistical analyses were performed using GraphPad Prism 8 (GraphPad).  
348 The Mann-Whitney test was used and P-value (two- tailed) was obtained (P value:  
349 0.12 (ns), 0.033 (\*), 0.002 (\*\*), <0.001 (\*\*\*)).

350

### 351 **Acknowledgements**

352 We thank the Bloomington Stock Center and VDRC for fly stocks. We thank K. Ramlow  
353 for purifying and testing *Drosophila* anti-Swip-1 antibodies. We thank Katja Rust for  
354 helpful discussions and critical reading of the manuscript. The work was supported by  
355 grants to S.B. (BO1890 4-2) from the Deutsche Forschungsgemeinschaft (DFG).

356 **References**

- 357 Abrams, E.W., Vining, M.S., and Andrew, D.J. (2003). Constructing an organ: the  
358 *Drosophila* salivary gland as a model for tube formation. *Trends in Cell Biology* 13,  
359 247-254.
- 360 Bischof, J., Maeda, R.K., Hediger, M., Karch, F., and Basler, K. (2007). An optimized  
361 transgenesis system for *Drosophila* using germ-line-specific phiC31 integrases. *Proc*  
362 *Natl Acad Sci U S A* 104, 3312-3317.
- 363 Biyasheva, A., Do, T.V., Lu, Y., Vaskova, M., and Andres, A.J. (2001). Glue secretion  
364 in the *Drosophila* salivary gland: a model for steroid-regulated exocytosis. *Dev Biol*  
365 231, 234-251.
- 366 Brinkmann, K., Winterhoff, M., Onel, S.F., Schultz, J., Faix, J., and Bogdan, S. (2016).  
367 WHAMY is a novel actin polymerase promoting myoblast fusion, macrophage cell  
368 motility and sensory organ development in *Drosophila*. *J Cell Sci* 129, 604-620.
- 369 Burgoyne, R.D., and Morgan, A. (2003). Secretory granule exocytosis. *Physiol Rev* 83,  
370 581-632.
- 371 Costantino, B.F., Bricker, D.K., Alexandre, K., Shen, K., Merriam, J.R., Antoniewski,  
372 C., Callender, J.L., Henrich, V.C., Presente, A., and Andres, A.J. (2008). A novel  
373 ecdysone receptor mediates steroid-regulated developmental events during the mid-  
374 third instar of *Drosophila*. *PLoS Genet* 4, e1000102.
- 375 Hornbruch-Freitag, C., Griemert, B., Buttgereit, D., and Renkawitz-Pohl, R. (2011).  
376 *Drosophila* Swiprosin-1/EFHD2 accumulates at the pre-fusion complex stage during  
377 *Drosophila* myoblast fusion. *J Cell Sci* 124, 3266-3278.
- 378 Huh, Y.H., Kim, S.H., Chung, K.H., Oh, S., Kwon, M.S., Choi, H.W., Rhee, S., Ryu,  
379 J.H., Park, Z.Y., Jun, C.D., *et al.* (2013). Swiprosin-1 modulates actin dynamics by  
380 regulating the F-actin accessibility to cofilin. *Cellular and Molecular Life Sciences* 70,  
381 4841-4854.
- 382 Huh, Y.H., Oh, S., Yeo, Y.R., Chae, I.H., Kim, S.H., Lee, J.S., Yun, S.J., Choi, K.Y.,  
383 Ryu, J.H., Jun, C.D., *et al.* (2015). Swiprosin-1 stimulates cancer invasion and  
384 metastasis by increasing the Rho family of GTPase signaling. *Oncotarget* 6, 13060-  
385 13071.
- 386 Kogias, G., Kornhuber, J., Reimer, D., Mielenz, D., and Muller, C.P. (2019). Swiprosin-  
387 1/ EFhd2: from Immune Regulator to Personality and Brain Disorders. *Neurosignals*  
388 27, 1-19.
- 389 Kwon, M.S., Park, K.R., Kim, Y.D., Na, B.R., Kim, H.R., Choi, H.J., Piragyte, I., Jeon,  
390 H., Chung, K.H., Song, W.K., *et al.* (2013). Swiprosin-1 Is a Novel Actin Bundling  
391 Protein That Regulates Cell Spreading and Migration. *Plos One* 8.
- 392 Leader, D.P., Krause, S.A., Pandit, A., Davies, S.A., and Dow, J.A.T. (2018). FlyAtlas  
393 2: a new version of the *Drosophila melanogaster* expression atlas with RNA-Seq,  
394 miRNA-Seq and sex-specific data. *Nucleic Acids Res* 46, D809-D815.



- 395 Lehne, F., Pokrant, T., Parbin, S., Salinas-Riester, G., Rust, K., Faix, J. and Bogdan,  
396 S. (2022). Calcium bursts allow rapid reorganization of EFhd2/Swip-1 cross-linked  
397 actin networks to drive epithelial wound closure. *Nat Commun*, accepted.
- 398 Loganathan, R., Kim, J.H., Wells, M.B., and Andrew, D.J. (2021). Secrets of secretion-  
399 How studies of the *Drosophila* salivary gland have informed our understanding of the  
400 cellular networks underlying secretory organ form and function. *Curr Top Dev Biol* *143*,  
401 1-36.
- 402 Luschnig, S., Batz, T., Armbruster, K., and Krasnow, M.A. (2006). serpentine and  
403 vermiform encode matrix proteins with chitin binding and deacetylation domains that  
404 limit tracheal tube length in *Drosophila*. *Curr Biol* *16*, 186-194.
- 405 Masedunskas, A., Sramkova, M., Parente, L., Sales, K.U., Amornphimoltham, P.,  
406 Bugge, T.H., and Weigert, R. (2011). Role for the actomyosin complex in regulated  
407 exocytosis revealed by intravital microscopy. *Proc Natl Acad Sci U S A* *108*, 13552-  
408 13557.
- 409 Merrifield, C.J. (2016). Actin puts the squeeze on *Drosophila* glue secretion. *Nat Cell*  
410 *Biol* *18*, 142-144.
- 411 Mielenz, D., and Gunn-Moore, F. (2016). Physiological and pathophysiological  
412 functions of Swiprosin-1/EFhd2 in the nervous system. *Biochem J* *473*, 2429-2437.
- 413 Miklavc, P., Ehinger, K., Sultan, A., Felder, T., Paul, P., Gottschalk, K.E., and Frick, M.  
414 (2015). Actin depolymerisation and crosslinking join forces with myosin II to contract  
415 actin coats on fused secretory vesicles. *J Cell Sci* *128*, 1193-1203.
- 416 Moreno-Layseca, P., Jantti, N.Z., Godbole, R., Sommer, C., Jacquemet, G., Al-  
417 Akhrass, H., Conway, J.R.W., Kronqvist, P., Kallionpaa, R.E., Oliveira-Ferrer, L., *et al.*  
418 (2021). Cargo-specific recruitment in clathrin- and dynamin-independent endocytosis.  
419 *Nat Cell Biol* *23*, 1073-1084.
- 420 Nightingale, T.D., Cutler, D.F., and Cramer, L.P. (2012). Actin coats and rings promote  
421 regulated exocytosis. *Trends Cell Biol* *22*, 329-337.
- 422 Nightingale, T.D., White, I.J., Doyle, E.L., Turmaine, M., Harrison-Lavoie, K.J., Webb,  
423 K.F., Cramer, L.P., and Cutler, D.F. (2011). Actomyosin II contractility expels von  
424 Willebrand factor from Weibel-Palade bodies during exocytosis. *J Cell Biol* *194*, 613-  
425 629.
- 426 Porat-Shliom, N., Milberg, O., Masedunskas, A., and Weigert, R. (2013). Multiple roles  
427 for the actin cytoskeleton during regulated exocytosis. *Cell Mol Life Sci* *70*, 2099-2121.
- 428 Rousso, T., Schejter, E.D., and Shilo, B.Z. (2016). Orchestrated content release from  
429 *Drosophila* glue-protein vesicles by a contractile actomyosin network. *Nat Cell Biol* *18*,  
430 181-190.
- 431 Sokac, A.M., Co, C., Taunton, J., and Bement, W. (2003). Cdc42-dependent actin  
432 polymerization during compensatory endocytosis in *Xenopus* eggs. *Nat Cell Biol* *5*,  
433 727-732.

- 434 Spiliotis, E.T., and Nelson, W.J. (2003). Spatial control of exocytosis. *Curr Opin Cell Biol* 15, 430-437.  
435
- 436 Thylur, R.P., Gowda, R., Mishra, S., and Jun, C.D. (2018). Swiprosin-1: Its Expression and Diverse Biological Functions. *J Cell Biochem* 119, 150-156.  
437
- 438 Tran, D.T., Masedunskas, A., Weigert, R., and Ten Hagen, K.G. (2015). Arp2/3-mediated F-actin formation controls regulated exocytosis in vivo. *Nat Commun* 6, 10098.  
439  
440
- 441 Tran, D.T., and Ten Hagen, K.G. (2017). Real-time insights into regulated exocytosis. *J Cell Sci* 130, 1355-1363.  
442
- 443 Trifaro, J.M., Gasman, S., and Gutierrez, L.M. (2008). Cytoskeletal control of vesicle transport and exocytosis in chromaffin cells. *Acta Physiol (Oxf)* 192, 165-172.  
444
- 445 Tu, Y., Zhang, L., Tong, L., Wang, Y., Zhang, S., Wang, R., Li, L., and Wang, Z. (2018). EFhd2/swiprosin-1 regulates LPS-induced macrophage recruitment via enhancing actin polymerization and cell migration. *Int Immunopharmacol* 55, 263-271.  
446  
447
- 448 Uhlen, M., Fagerberg, L., Hallstrom, B.M., Lindskog, C., Oksvold, P., Mardinoglu, A., Sivertsson, A., Kampf, C., Sjostedt, E., Asplund, A., *et al.* (2015). Proteomics. Tissue-based map of the human proteome. *Science* 347, 1260419.  
449  
450
- 451 Wu, L.G., Hamid, E., Shin, W., and Chiang, H.C. (2014). Exocytosis and endocytosis: modes, functions, and coupling mechanisms. *Annu Rev Physiol* 76, 301-331.  
452

453 **Figure legends**

454

455 **Figure 1: Localization of EFhD2/Swip-1 at the apical membrane and secreting**  
456 **vesicles in salivary glands**

457 **(A)** Left: Schematic overview of imaging setup to visualize exocytosis in *ex vivo* larval  
458 salivary glands. Right: Detailed schemes of non-secretory and 20E-induced secretory  
459 epithelial cells showing F-actin localization at apical membrane and around fusing  
460 vesicles. **(B)** Western blot analysis of salivary gland lysates of wildtype and *swip-1*  
461 mutant larvae. Knock-out was validated with an anti-Swip-1-specific antibody. Actin  
462 served as loading control. **(C)** Confocal images of a fixed wild type non-secretory  
463 salivary gland stained for F-actin (Phalloidin, green) and Swip-1 (magenta). Swip-1 is  
464 located in the cytoplasm and enriched at the plasma membrane. Scale bar 25 $\mu$ m. **(D)**  
465 Confocal image of a fixed wild type secretory salivary gland stained for F-actin (green),  
466 Swip-1 (magenta) and DAPI (blue). Scale bar 25 $\mu$ m. **(D'-D''')** Detailed view of boxed  
467 area in (D). Swip-1 localizes at fusing vesicles at the apical membrane and colocalizes  
468 with F-actin. Vesicles are imaged from above with the lumen underneath (not visible).  
469 **(E)** Schematic of imaging angles. Secreting vesicles can either be imaged from above  
470 with the lumen underneath and not visible or from a lateral view, orthogonal to the  
471 apical membrane allowing visualization of a cross section of the vesicle and the lumen.  
472 PM: Plasma membrane. **(F)** Confocal image of a fixed secretory salivary gland from  
473 larvae expressing Swip-eGFP (magenta) under the control of *srp-Gal4* and stained for  
474 F-actin (green). Differences in vesicle visualization by lateral and top view are indicated  
475 by yellow and white arrowheads, respectively. Scale bar 5 $\mu$ m.

476

477 **Figure 2: Swip-1 is recruited to the membrane of fusing vesicle simultaneously**  
478 **with F-actin**

479 **(A)** Frame of spinning disc microscopy video of Swip-1-eGFP expressing salivary gland.  
480 A secreting vesicle from top view is indicated by white arrowhead. Scale bar 25 $\mu$ m.  
481 **(A')** Schematic description of (A). **(A'')** Frames of boxed area in (A). Secreting vesicle  
482 is indicated by yellow asterisk. Red arrowhead shows clearing of Swip-1-eGFP at the  
483 apical membrane and yellow arrowhead the subsequent coating of the vesicle with  
484 Swip-1-eGFP. Images were taken every 20s. **(B, B')** Detailed frames of spinning disc  
485 microscopy of LifeAct-Ruby (green) and eGFP-Swip-1 (magenta) expressing salivary  
486 gland. Green and magenta arrowheads indicate clearing at the apical membrane of

487 the respective protein for fusion pore formation. Fusing vesicle is indicated by green  
 488 and magenta asterisk. Images were taken every 10s. Scale bar 5 $\mu$ m. **(C)**  
 489 Representative graph of LifeAct and Swip-1 recruitment to the vesicle membrane. **(D)**  
 490 Quantification of Swip-1, WHAMY and zip recruitment in relation to LifeAct (red dashed  
 491 line, t=0). Swip-1 appears at the vesicle membrane simultaneously with F-actin while  
 492 WHAMY and zip appear afterwards. Fluorescence intensity was measured every 2s.  
 493 n(LifeAct/Swip-1): 5SG, 14 fusion events; n(LifeAct/WHAMY): 4SG, 10 fusion events;  
 494 n(LifeAct/zip): 4SG, 10 fusion events. Bars represent mean  $\pm$  SD.

495

496 **Figure 3: Swip-1 is not required for vesicle fusion but rather for cargo expulsion**

497 **(A)** Salivary glands expressing SerpCBD-GFP used to determine secretion status.  
 498 Secretory salivary glands display a bright green lumen (bottom image, red dashed  
 499 line). **(B)** Quantification of exocytosis of wildtype, *swip-1* mutant and rescued salivary  
 500 glands. Exocytosis was induced by addition of 1mM 20E and salivary glands assessed  
 501 for secretion for 8h. Green bars indicate secreting percentage of salivary glands. Error  
 502 bars from 4 independent experiments, total number of salivary glands: WT: 30SG,  
 503 *swip* $\Delta$ 1: 36SG, Swip-1-eGFP rescue: 39SG, Swip-1-D82A/D118A-eGFP rescue:  
 504 14SG, Swip-1- $\Delta$ CC-eGFP rescue: 31SG. **(C)** Frame of spinning disc microscopy video  
 505 of salivary gland expressing LifeAct-eGFP (green) infused with Dextran (magenta). **(D)**  
 506 Detailed frames of fusing vesicle in wildtype. **(E)** Detailed frames of fusing vesicle in  
 507 *swip-1* mutant. Images were taken every 2s. **(F, G)** Representative graphs of LifeAct  
 508 recruitment to the vesicle membrane and time of dextran entry in wildtype and *swip-1*  
 509 mutant. **(H)** Quantification of Dextran entry in relation to LifeAct (red dashed line, t=0).  
 510 There is no significant difference in time between wildtype and *swip-1* mutant salivary  
 511 glands. n(WT): 5SG, 17 fusion events; n(*swip* $\Delta$ 1): 5SG, 16 fusion events. **(I)** Confocal  
 512 image of fixed Sgs3-GFP (magenta) expressing salivary gland stained for F-actin  
 513 (green) and DAPI (blue) Scale bar 25 $\mu$ m. **(I')** Detailed view of boxed area in (I).  
 514 Vesicles are filled with glue protein and fused vesicles coated with F-actin. Scale bar  
 515 5 $\mu$ m. **(J)** Representative graphs of LifeAct recruitment and Sgs3 expulsion in wildtype  
 516 and *swip-1* mutant. **(K)** Quantification of expulsion duration. Cargo expulsion is  
 517 significantly delayed in *swip-1* mutants. n(WT): 4 SGs, 16 fusion events; n(*swip* $\Delta$ 1): 4  
 518 SGs, 16 fusion events. (H, K) Fluorescence intensity was measured every 2s, Bars  
 519 represent mean  $\pm$  SD.

520

521 **Figure 4: Swip-1 promotes effective exocytosis of glue granules in *Drosophila***  
 522 **salivary glands**

523 **(A)** Confocal images of a fixed wild type (WT) secretory salivary gland from larvae  
 524 stained for F-actin (green), active myosin (anti-phospho myosin light chain antibody,  
 525 magenta) and DAPI (blue). (A') Active myosin staining, (A'') detailed view of boxed  
 526 area in (A) showing F-actin and (A''') detail of active myosin around fused vesicles. **(B)**  
 527 Confocal images of a fixed *swip-1* mutant (*swipΔ1*) secretory salivary gland from larvae  
 528 stained for F-actin (green), active myosin (magenta) and DAPI (blue). (B') Active  
 529 myosin staining, (B'') detailed view of boxed area in (B) showing F-actin and (B''') detail  
 530 of active myosin around fused vesicles. Note that the level of active myosin II is  
 531 increased *swip-1* mutant SG compared to wild type. Images of were taken with same  
 532 excitation laser intensity and adjusted to same grey level values. For better  
 533 visualization of active myosin staining in wild type see inlet in (A'''). Scale bars 25μm  
 534 (A, B) and 5μm (A'', B''). **(C)** Schematic of the sequential events and Swip-1 localization  
 535 during regulated exocytosis in *Drosophila* SGs. **(D)** Scheme showing proposed  
 536 function of EFhD2/Swip-1 in regulated exocytosis. A fused vesicle at the apical  
 537 membrane is coated with a Arp2/3-dependent branched F-actin network which is  
 538 stabilized by Swip-1-induced actin cross-links necessary for effective exocytosis. In  
 539 addition, actin filament cross-linking by Swip-1 might also contribute to myosin II-  
 540 mediated force generation essential for actin coat compression and extrusion of  
 541 secretory vesicles.

542

543 **Supplementary Material**

544

545 **Supplementary movies**

546

547 **Supplementary movie M1:**

548 Time-lapse movie of *ex vivo* cultured salivary glands expressing UAS-Swip-1-eGFP  
 549 under the *srp*-Gal4 driver. Scale bar: 20μm.

550

551 **Supplementary movie M2:**

552 Time-lapse movie of *ex vivo* cultured salivary glands co-expressing UAS-eGFP-Swip-  
 553 1 and LifeAct-Ruby under the *srp*-Gal4 driver. Scale bar: 20μm.

554

555 **Supplementary movie M3:**

556 Time-lapse movie of *ex vivo* cultured wild type (left) and *swip-1* mutant (right) salivary  
557 glands infused with A568-dextran (magenta) and expressing LifeAct-eGFP (green)  
558 under the *srp*-Gal4 driver. Scale bar: 20µm.

559

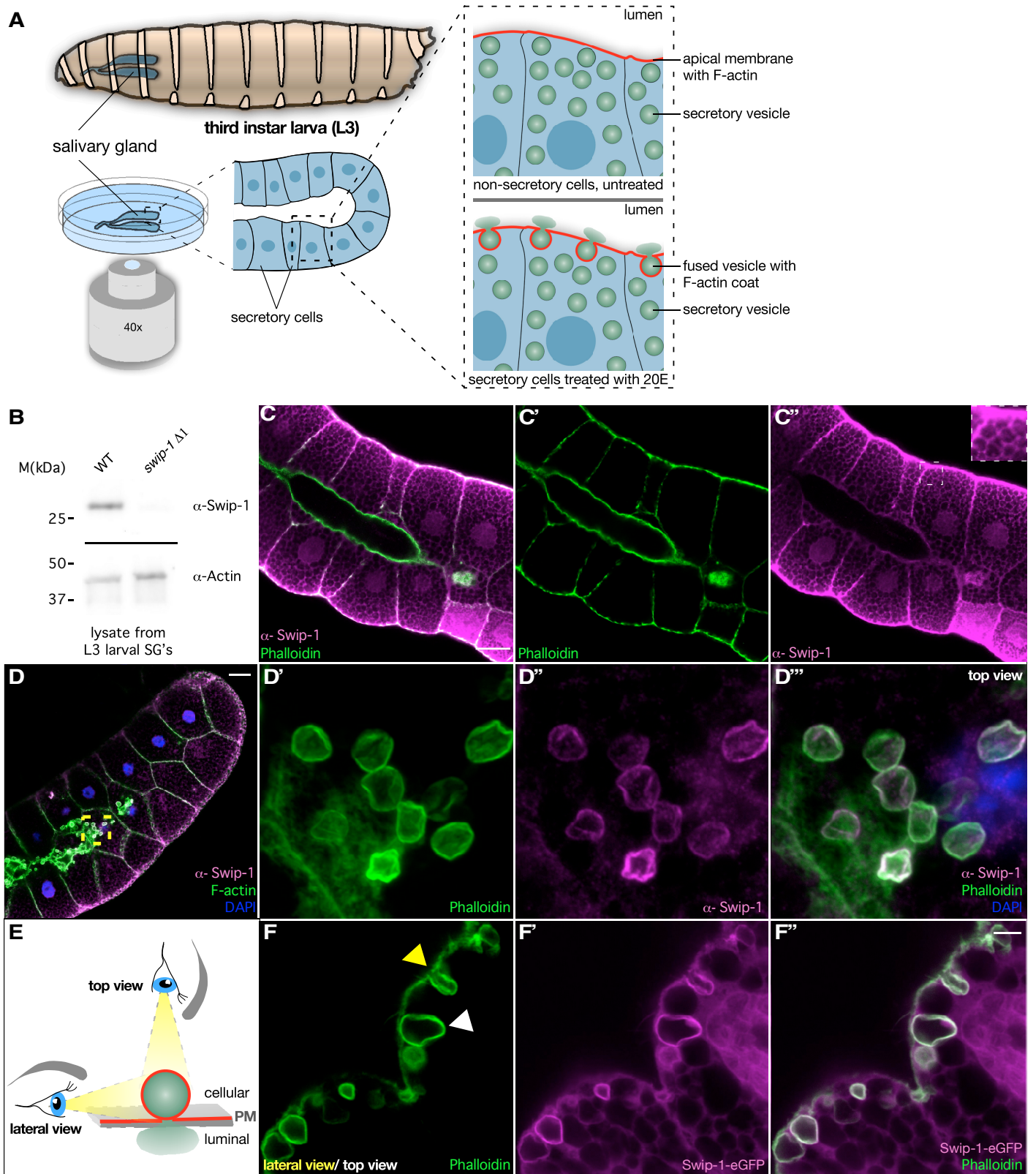


Figure 1, Lehne et al.

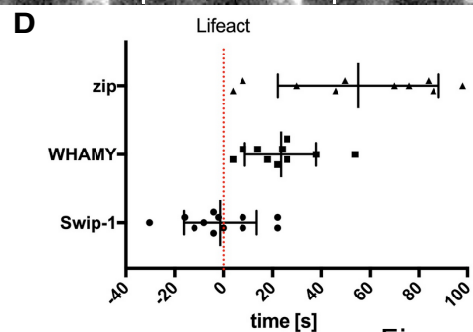
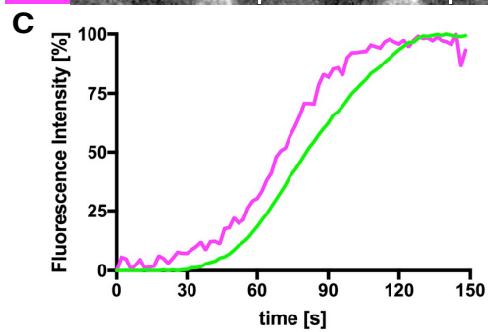
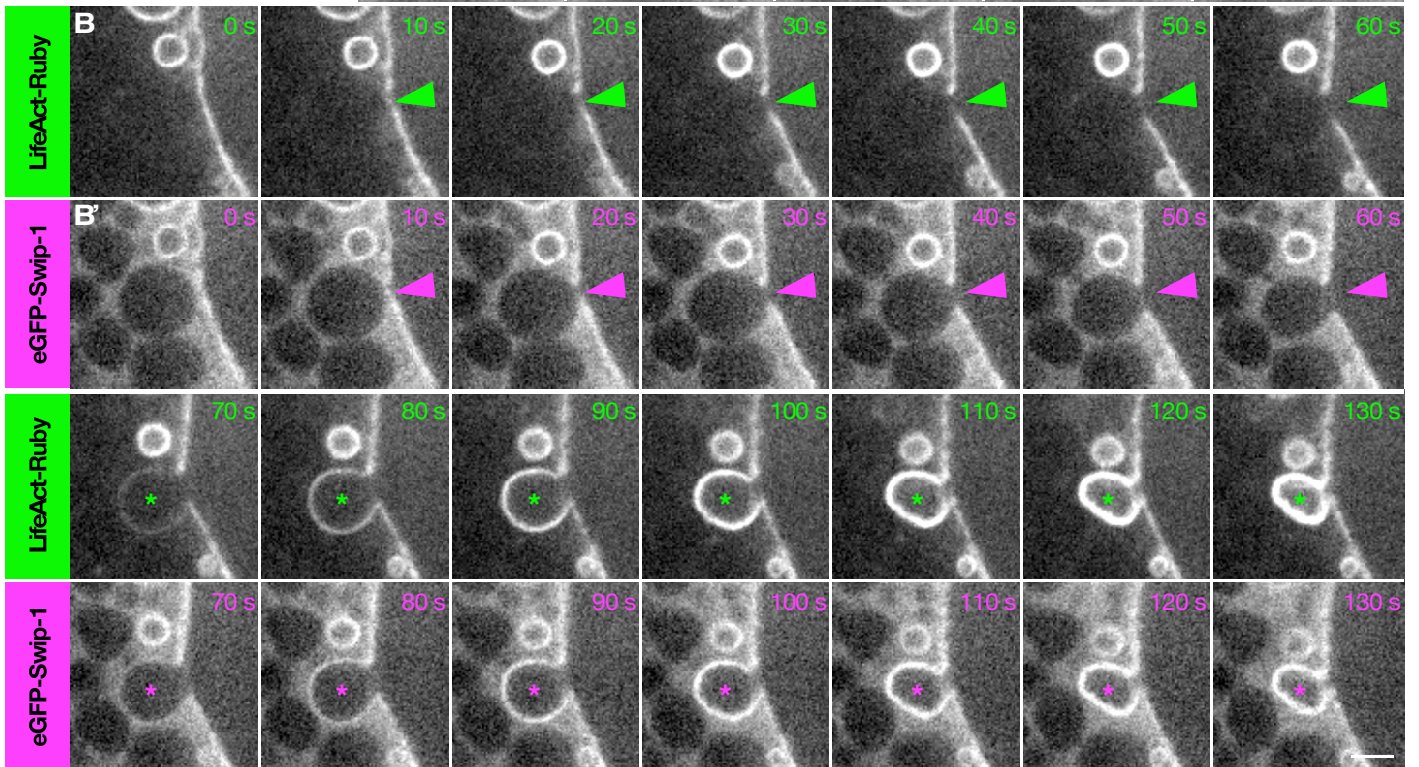
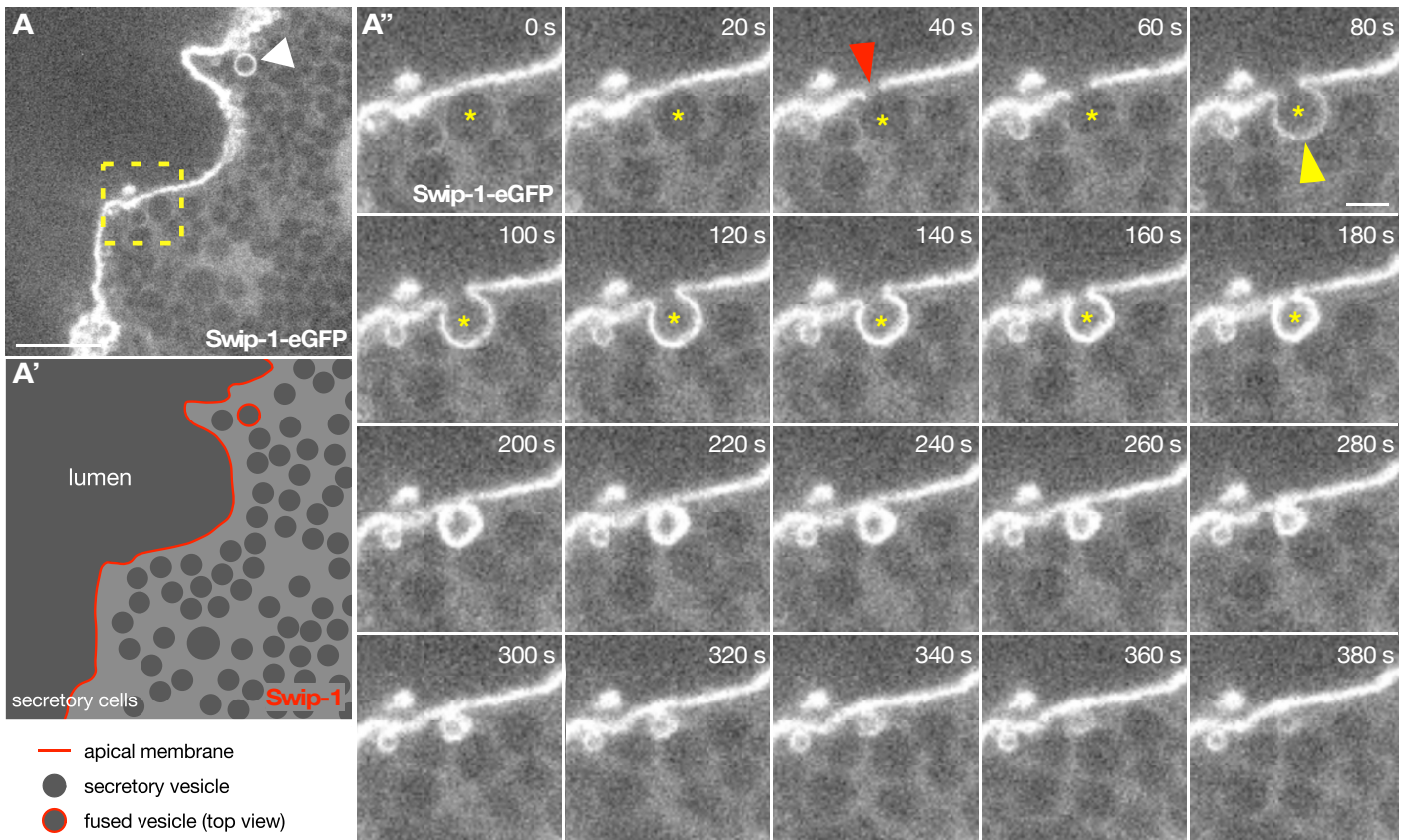


Figure 2, Lehne et al.



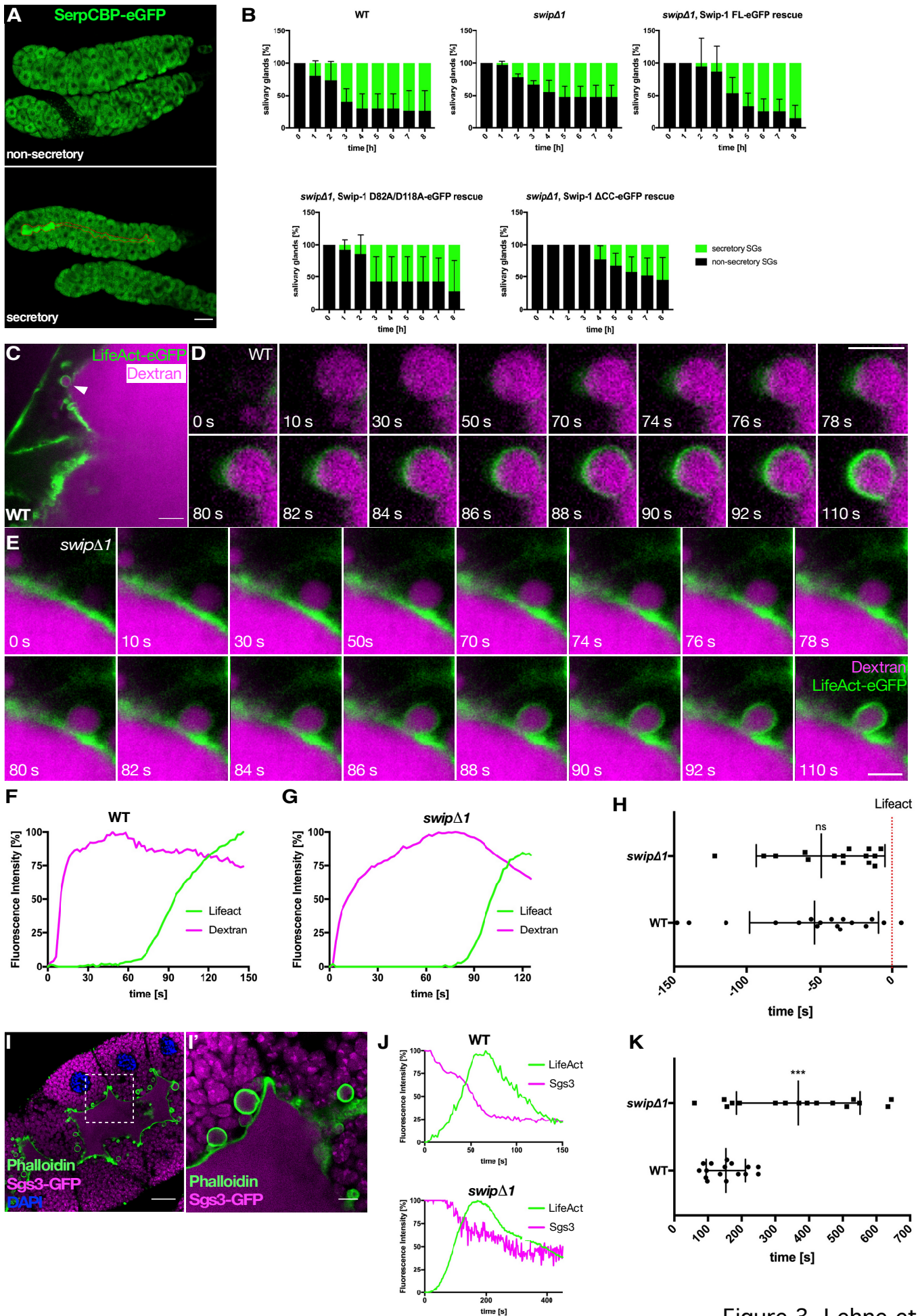


Figure 3, Lehne et al.

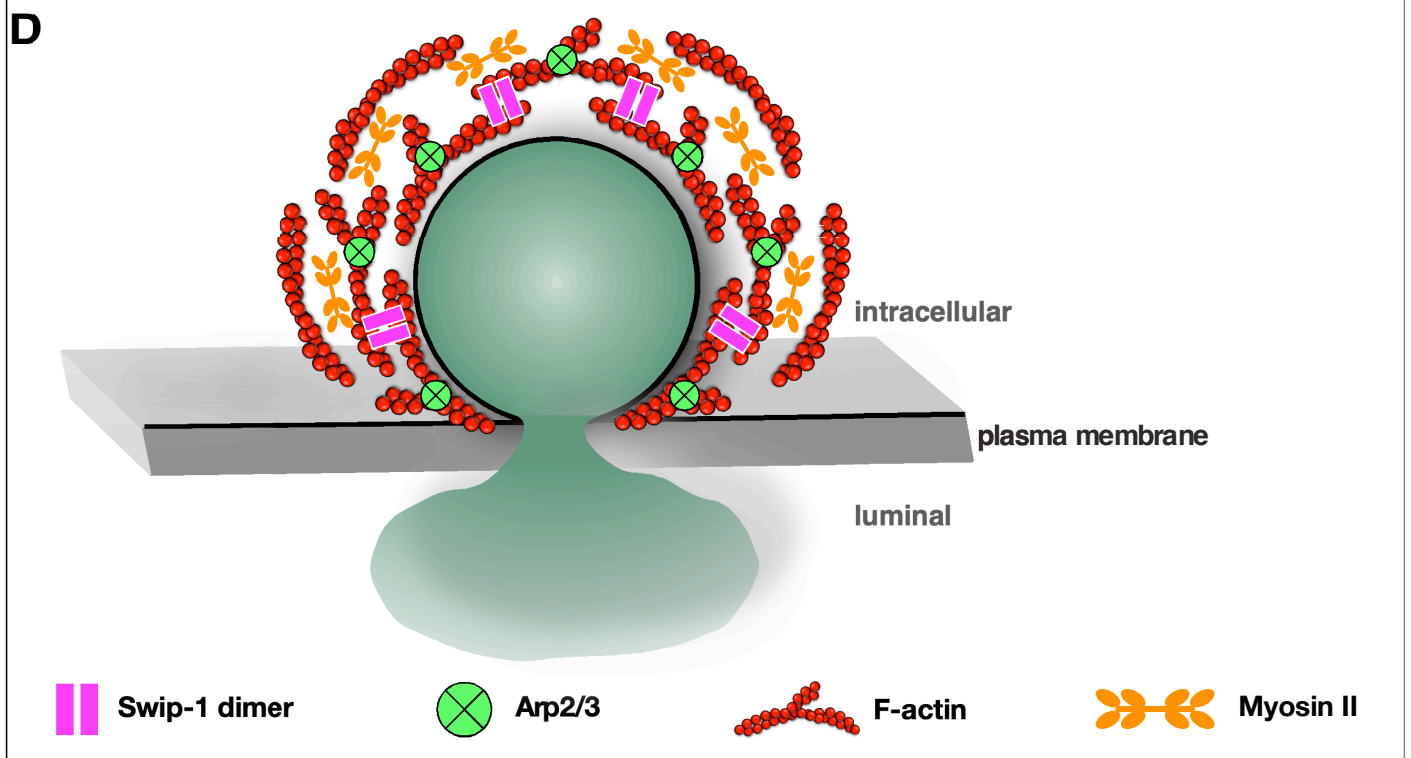
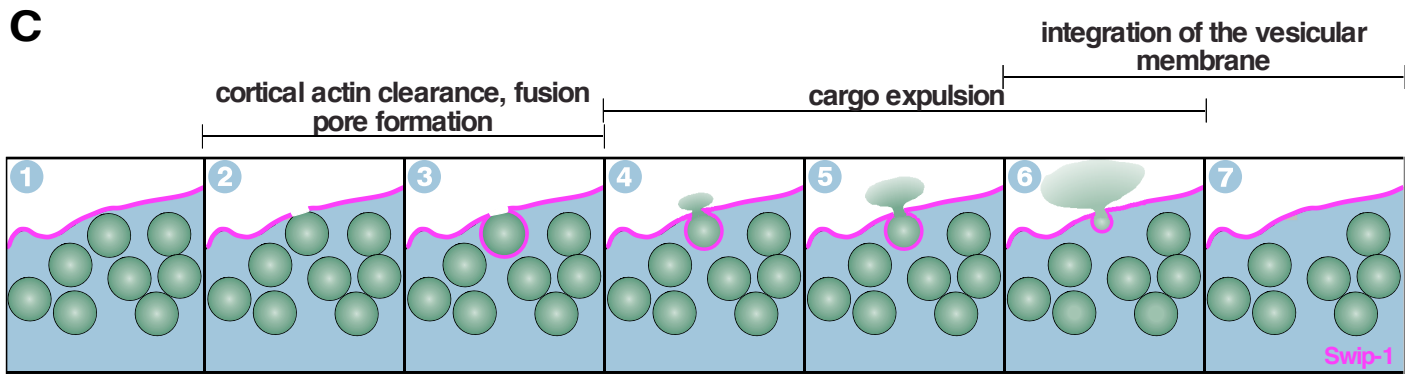
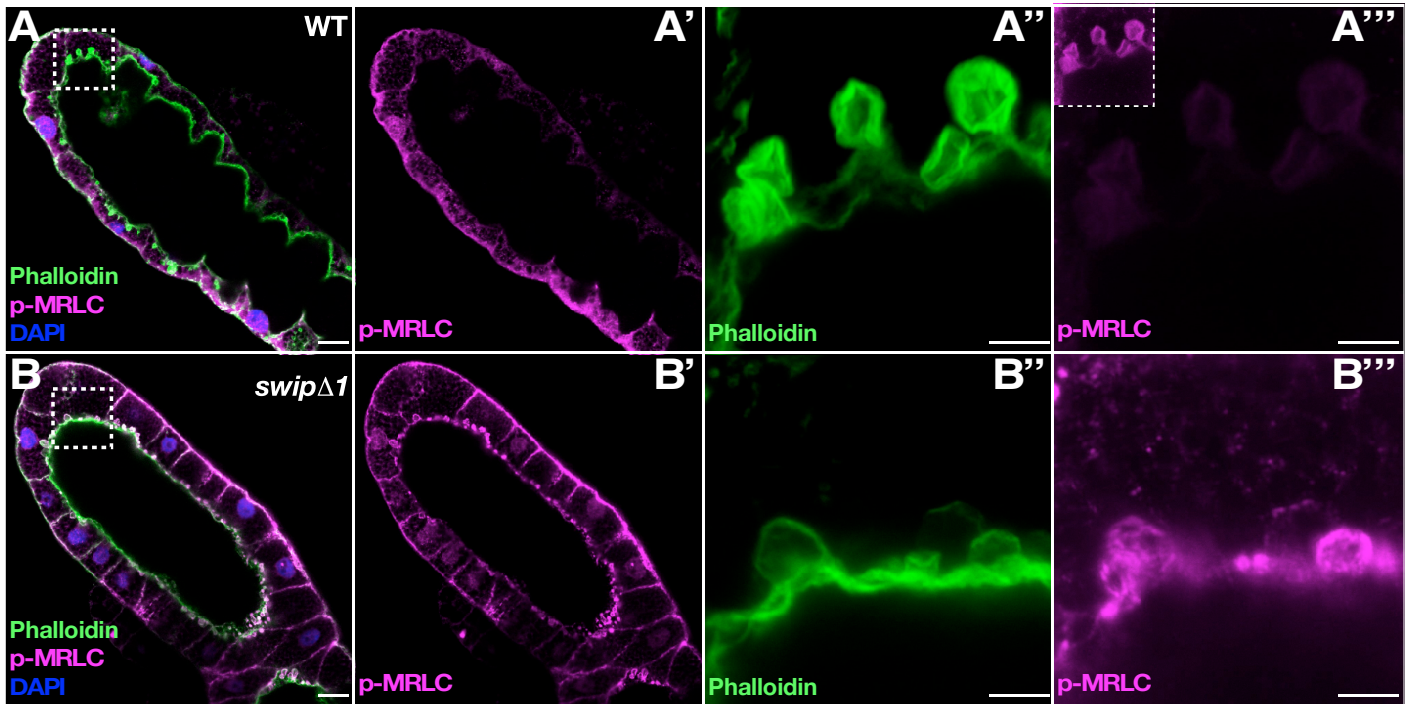


Figure 4, Lehne et al.

### 3 Additional Methods

Methods and statistical analyses are as described in Lehne et al. (2022) and Lehne & Bogdan. Additional methods are described below.

#### 3.1 Kymograph analysis of macrophages

For kymograph analysis, larval macrophages were isolated, plated on ConA-coated 8-well imaging chambers and settled for at least 20min at room temperature. Time-lapse imaging was performed with a Zeiss CellObserver Z.1 with a Yokogawa CSU-X1 spinning disc scanning unit and an Axiocam MRm CCD camera (6.45  $\mu\text{m}$  x 6.45  $\mu\text{m}$ ). To generate kymographs, ImageJ Reslice [/] function was used along a line selection in the protruding and retracting lamellipodium.

#### 3.2 Fluorescence recovery after photobleaching (FRAP)

For FRAP experiments, pupal macrophages were isolated, plated on ConA-coated glass bottom dishes and settled for 30min at room temperature. Imaging was performed on a Leica TCS SP8 with an HC PL APO CS2 63x/1.4 oil objective. The FRAP module in the Leica LAS X software was chosen. Setup was set to xyt image acquisition with 1800Hz scanning speed (bidirectional) in a single z-plane and an image size of 1024px x 1024px with line averaging of four. Three pre-bleach images were taken. Bleaching was at 100% laser power (488nm) and two scans of a  $1\mu\text{m}^2$  region in the lamellipodium. After bleaching cells were recorded for 45s in an interval of 1.15s (minimal setting). Fluorescence bleaching due to image acquisition was recorded on a  $1\mu\text{m}^2$  region in the lamellipodium with no laser bleaching and distant from the bleached region. Fluorescence intensity recording was automated by the LAS X software and exported to Microsoft Excel. Further calculations of final normalized fluorescence values were done according to Basic Protocol 2 from Hardy (2012). For plotting and calculation of recovery half time and fractional recovery GraphPad Prism 7 was used. Curves were fitted using one-phase association.

### 3.3 Automated detection and analysis of protrusions (ADAPT)

To analyze lamellipodial protrusion and retraction velocity, larval macrophages were isolated, plated on ConA-coated glass bottom dishes and settled for 30min at room temperature. Time lapse imaging of single macrophages expressing cytoplasmic GFP was performed on a Leica TCS SP8 with an HC PL APO CS2 63x/1.4 oil objective. Analysis was performed with the Adapt plugin of ImageJ. The cytoplasmic channel was chosen with signal to be correlated set to none. Thresholding was performed automatically. Further settings included a spatial resolution of 0.02  $\mu\text{m}/\text{pixel}$ ; 6fps; minimum trajectory length of 1 $\mu\text{m}$  and minimum object size of 100 $\mu\text{m}^2$  to be detected.

### 3.4 Vesicle size in larval salivary glands

Non-secreting salivary glands of wandering third instar larvae expressing Sgs3-GFP were dissected and single epithelial cells imaged using a Leica TCS SP8 with an HC PL APO CS2 63x/1.4 oil objective and the Lightning deconvolution module. Analysis of cross-section area was performed according to Ma & Brill (2021). Cross-section areas were determined using the surface module in Imaris 9.3 software (Bitplane).

### 3.5 Recruitment of protein of interest to secreting vesicle membrane

To determine the time a protein of interest is recruited to the membrane of a secreting vesicle in live *ex vivo* salivary glands, the fluorescence intensity change was measured. Time lapse image acquisition was every 2s for 10-20min. Measurement of percent fluorescent intensity of Lifeact/Swip-1, Lifeact/WHAMY, Lifeact/zip, Lifeact/sqh and Lifeact/Dextran was performed as previously described in Tran et al. (2015). In short, an oval region of interest was drawn around single fusing vesicles in one z-plane. The “plot z-axis profile” function in ImageJ was used to obtain fluorescence intensity values for each channel. Subsequent calculations of % fluorescence intensity and time difference of detection were carried out in Microsoft Excel according to Tran and colleagues. The percent fluorescent intensity of each channel at each time point  $t$  was calculated as:

$$\% \text{ fluorescence intensity } (t) = [\text{fluorescence intensity } (t) - \text{fluorescence intensity } (t_0)] / [\text{max fluorescence intensity} - \text{fluorescence intensity } (t_0)] \times 100.$$

“ $t_0$ ” is the time frame at which one of the two channels being measured begins to continually increase in fluorescence intensity and was manually determined from the obtained measurements. “max fluorescence intensity” is the maximum fluorescence

intensity value reached for each respective channel being measured. “% fluorescence intensity” values that were negative due to fluctuations in intensity values were set to 0. To determine the average time difference in the detection of each component in the pairwise comparisons, the time between  $t_0$  and when fluorescence intensity of the second component began to continually increase and was at least 1% higher than the previous time point for at least 5 time points (10s) was calculated. Accordingly, measurement of time of cargo expulsion was determined by calculating the time difference between detection of LifeAct and minimal Sgs3 fluorescence in the region of interest.

### **3.6 Crumpling analysis of secreting vesicles**

Salivary glands of Lifeact-GFP expressing larvae were imaged from top view as described in Lehne & Bogdan. Single vesicles were traced manually every 10s (WT) or 30s (mutant) from appearing of F-actin coat to complete release of cargo (no visible lumen). Circularity of the vesicle was measure using ImageJ shape descriptors. Crumpling was analyzed and plotted as change of vesicle circularity over time.

### **3.7 Protein purification**

Expression of GST-tagged Swip-1 variants in *E. coli* strain ArcticExpress competent cells (Agilent) was induced with 1mM IPTG at 10°C for 24h. The bacteria were harvested and lysed by ultrasonication in PBS, pH 7.4 containing cOmplete™ protease inhibitor cocktail (Sigma). The fusion protein was purified from bacterial extracts by affinity chromatography using glutathione-conjugated GSTrap™ FF column (GE Healthcare) and the GST-tag cleaved off on the column by adding PreScission protease (GE Healthcare) over night. Fractions containing Swip-1 and no or faint amounts of residual cleaved GST were determined by Coomassie Blue and antibody staining. Fractions were pooled, snap frozen in liquid nitrogen and stored at -80°C.

### **3.8 Low-speed actin co-sedimentation assay**

For F-actin bundling analysis, the Actin Binding Protein Spin-Down Assay Biochem Kit: Rabbit Skeletal Muscle Actin (Cytoskeleton, Inc.) was used and carried out according to manufactures instructions. Prior to protein addition, an extra centrifugation step of the polymerized F-actin was performed. Proteins of interest were diluted to identical

molarities. The amount of F-actin added to the various proteins was doubled, therefore resuspension volume of the pellet was adjusted as well. To quantitate co-sedimentation of Swip-1 variants with F-actin, after SDS-PAGE and Coomassie Blue staining, the amount of the proteins in the pellet and supernatant fractions was determined densitometrically using ImageJ software. GST and  $\alpha$ -actinin served as negative and positive control, respectively.

### **3.9 Size exclusion chromatography**

S2R+ cells were lysed by ultrasonication in 25mM Tris-HCl, pH 7.6 and 1% Triton-X100 containing cOmplete™ protease inhibitor cocktail (Sigma). Size exclusion was performed with a Superose® 6 Increase 10/300 GL column (Sigma). Fractions of 500 $\mu$ L volume were collected and solved proteins precipitated with trichloroacetic acid (TCA) and resuspended in SDS-sample buffer. For quantitate relative Swip-1 concentration in each fraction, after SDS-PAGE and Western blot stained against Swip-1, the amount of protein in each fraction was determined densitometrically using ImageJ software.

### **3.10 Quantification of directed migration of macrophages**

All analyses were conducted according to Hirschhäuser et al. (2021).

## 4 Additional Results

### 4.1 Swip-1 localizes to protruding lamellipodia

The *Drosophila* genome contains only one gene encoding Swip-1, which shows highest sequence homology to the human EFHD2. *swip-1* is located on the second chromosome corresponding to the cytological location 37B8. Using CRISPR/Cas9 technique (Gratz et al., 2015), a deletion of seven base pairs shortly after the start codon was introduced. This resulted in a premature stop codon and therefore a null mutant allele named *swip*<sup>Δ1</sup> (Publication 1, figure 2a). Loss of *swip-1* was confirmed by Western blot analysis using a specific anti-Swip-1 antibody (Publication 1, figure 2b). In order to exclude any off-target deletions caused by the CRISPR-target sequence, the *swip*<sup>Δ1</sup> allele was tested in combination with a deficiency spanning the cytological region 37B1 – 37C5 (Df(2L)<sup>ED1202</sup>). Compared to wildtype macrophages, both the heterozygous Df(2L)<sup>ED1202</sup> and the *swip-1* deficient *Drosophila* macrophages displayed an irregular lamellipodium when spread on the lectin concanavalin A (ConA) (Figure 8A-A''). This was quantified as decreased circularity of the cells (Figure 8D). The trans-heterozygous macrophages containing both the deficiency and *swip-1* mutant allele, displayed an even more reduced circularity (Figure 8A''', D).

Because loss of *swip-1* led to a disrupted lamellipodia formation in macrophages, overexpression of the protein was analyzed. Compared to wildtype, overexpression of Swip-1 in macrophages led to a visible increase in lamellipodia width (Figure 8B) as has been already shown for transfected S2R+ cells (Publication 1, figure 1f, g).

Strikingly, RNAi-mediated knock down of Swip-1 caused macrophages to display thick F-actin bundles shown by Phalloidin staining (Publication 1, figure 1a). These thick F-actin bundles were even more prominent when macrophages were plated on the ECM protein vitronectin (Figure 8C).

In fixed macrophages, Swip-1 and F-actin were shown to colocalize in the lamellipodium (Publication1, figure 1d). In order to further characterize this colocalization, fluorescently tagged transgenes of Swip-1 and the F-actin probe Lifeact were analyzed. Even though *ex vivo* macrophages plated on ConA do not migrate, they still display waves of lamellipodia protrusion and retraction. Kymographs of *ex vivo* macrophages expressing Swip-1-mScarlet and Lifeact-GFP transgenes revealed same localization dynamics during lamellipodia protrusion and retraction (Figure 8E).

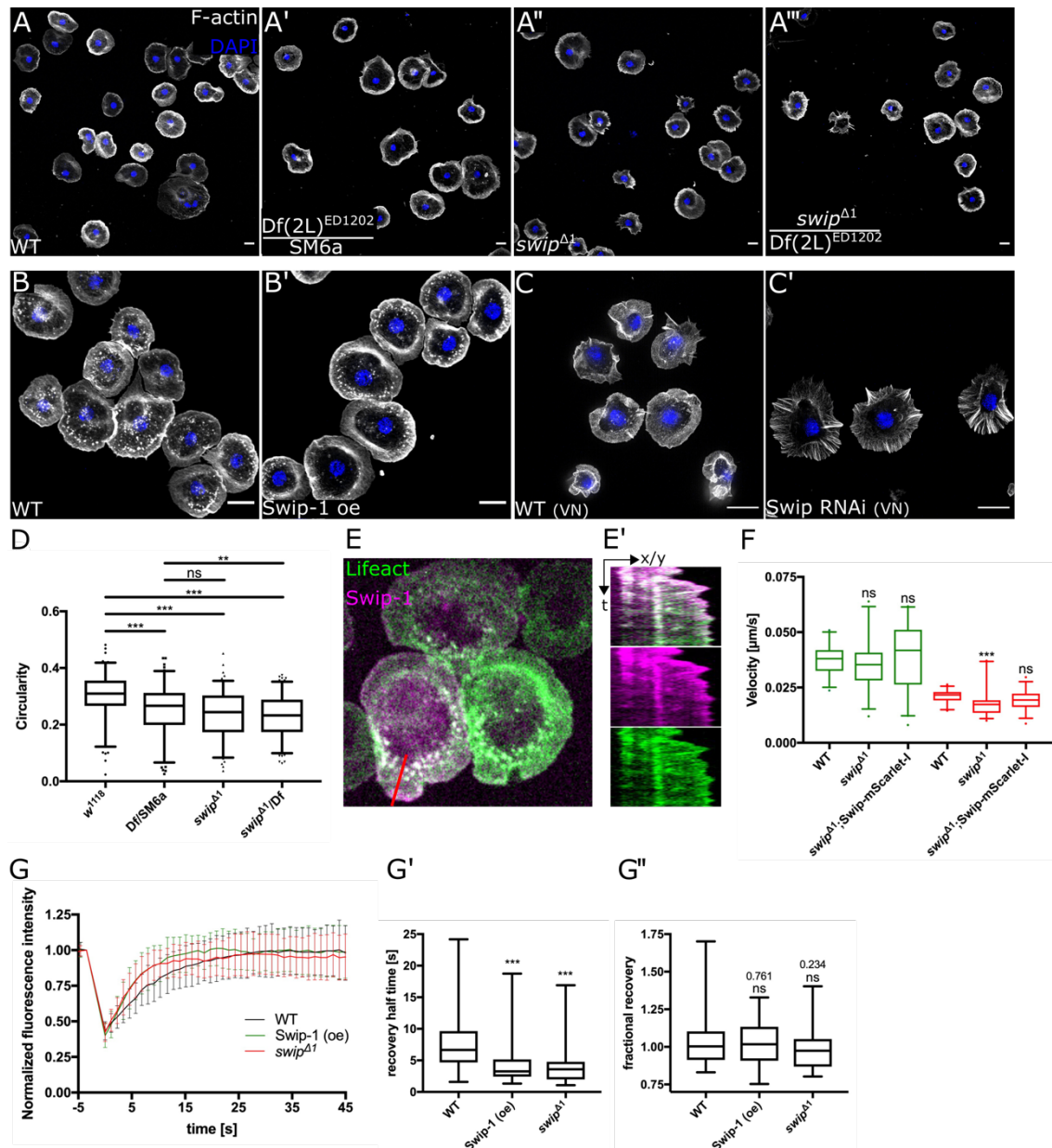


**Figure 8 – Swip-1 localizes in the protruding lamellipodia of macrophages.** (A-C) Maximum intensity projection of confocal images of the actin cytoskeleton in prepupal macrophages. Cells were co-stained for F-actin (white) and DAPI (blue). Genotypes as indicated. Scale bars 10 $\mu$ m. (D) Circularity of macrophages was measured using FIJI shape descriptors.  $n = w^{1118}$ : 120, Df/SM6a: 113, swip $\Delta 1$ : 116, swip $\Delta 1$ /Df: 141 cells. (E) Frame of spinning disc microscopy video of protruding macrophages expressing Lifeact-GFP (green) and Swip-1-mScarlet (magenta) fusion proteins. Images were taken every 5s for 10min. (E') Kymograph of protruding and retracting lamellipodium indicated by red line in (E). (F) Automated detection and analysis of protrusions (ADAPT) of macrophages. Shown are the velocities of protrusion (green) and retraction (red) of the indicated genotypes.  $n =$  WT: 36, swip $\Delta 1$ : 38, swip $\Delta 1$ , Swip-1-mScarlet: 39 cells. (G) Fluorescence recovery after photobleaching (FRAP) of macrophages expressing GFP-actin. Graph of normalized fluorescence over time and analyses of (G') recovery half time and (G'') fractional recovery with p-values are shown. Three independent experiments with measurement of 10 cells each. (E, F, H, I, I'') Mann-Whitney test, p-value: 0.12 (ns), 0.033 (\*), 0.002 (\*\*), <0.001 (\*\*\*)

To further investigate if Swip-1 has an impact on lamellipodia protrusion or retraction, the velocities of these membrane dynamics were analyzed. Wild-typic macrophages protrude their lamellipodium with a velocity of  $0.0375 \pm 0.0067 \mu\text{m/s}$  and retract it with



$0.0210 \pm 0.0029 \mu\text{m/s}$  (Figure 8F). Even though the protrusion velocity of cells lacking Swip-1 protein did not reveal any significant changes ( $0.0349 \pm 0.0105 \mu\text{m/s}$ ), the measured retraction velocity of  $0.0173 \pm 0.0056 \mu\text{m/s}$  was significantly slower than in wildtype macrophages. Re-expression of the Swip-1-mScarlet fusion protein rescued this phenotype (protrusion velocity:  $0.0393 \pm 0.0142 \mu\text{m/s}$ ; retraction velocity:  $0.0194 \pm 0.0048 \mu\text{m/s}$ ). The lamellipodium retracts when the rate of F-actin disassembly is higher than the rate of F-actin assembly at the leading edge. However, it has been recently shown that also changes in retrograde flow of actin can have an impact on protrusion and retraction velocity (Ryan et al., 2017).

Therefore, the retrograde flow in wildtype and *swip-1* mutant macrophages was analyzed. As parameter for the actin turnover in the lamellipodium, fluorescence recovery after photobleaching (FRAP) of GFP-tagged actin was measured. If retrograde flow is altered, the recovery of fluorescence in a defined bleached area of the lamellipodium would change as well. The fluorescence recovery rate of wildtype macrophages was slower than of *swip-1* mutant and Swip-1 overexpressing macrophages (Figure 8G, G'). Intriguingly, a tendency of less fractional recovery in *swip-1* mutant macrophages compared to both, wildtype and overexpression of Swip-1 could be seen, although no statistical significance was determined (Figure 8G''). A reduced fractional recovery of fluorescence means that after bleaching the initial fluorescence intensity cannot be restored due to immobile fluorophores.

## 4.2 Swip-1's coiled-coil domain is required for F-actin cross-linking

We could show that contrary to previous findings, Swip-1 as well as human EFHD2 cross-link actin filaments at a preferred right angle therefore stabilizing an F-actin network. *In vitro* experiments showed that this cross-linking activity is  $\text{Ca}^{2+}$ -dependent. In the presence of  $\text{Ca}^{2+}$  the cross-links became transient while  $\text{Ca}^{2+}$  reduction led to stable cross-links and rare detachment of Swip-1 from F-actin (Publication 1).

*In vitro* actin co-sedimentation assay was used to further determine which Swip-1 domains are necessary for F-actin cross-linking (Figure 9A). Swip-1-full length protein co-sedimented with approximately 40% of the present F-actin. This is comparable to the results in publication 1 obtained from our collaboration partners (see publication 1, figure 3g). The Swip-1-D82A/D118A variant contains two point mutations of highly conserved aspartates to alanine in both EF-loops. This has been shown to diminish  $\text{Ca}^{2+}$ -binding activity (Ferrer-Acosta et al., 2013). The Swip-1-D82A/D118A variant co-sedimented

with 55% of the F-actin. Lastly, the Swip-1- $\Delta$ CC variant lacks the C-terminus containing the coiled coil domain (aa180-217). It only co-sedimented with 25% of the present F-actin which is comparable to the results of the GST negative control (not shown).

As described above, *in vitro* experiments showed that removal of  $\text{Ca}^{2+}$  leads to stable Swip-1-mediated F-actin cross-links. To analyze the effect on whole cell protein lysates, S2R<sup>+</sup> cells were treated with  $\text{Ca}^{2+}$  chelating agents (Bapta-AM and EGTA). The cell lysate was subjected to size exclusion chromatography to resolve protein complexes by size. The proteins of the different fractions were separated by SDS-PAGE followed by Western blot analysis and antibody staining against Swip-1 (Figure 9B). This revealed, that upon chelation of  $\text{Ca}^{2+}$ , Swip elutes in a higher molecular mass fraction (Figure 9B').

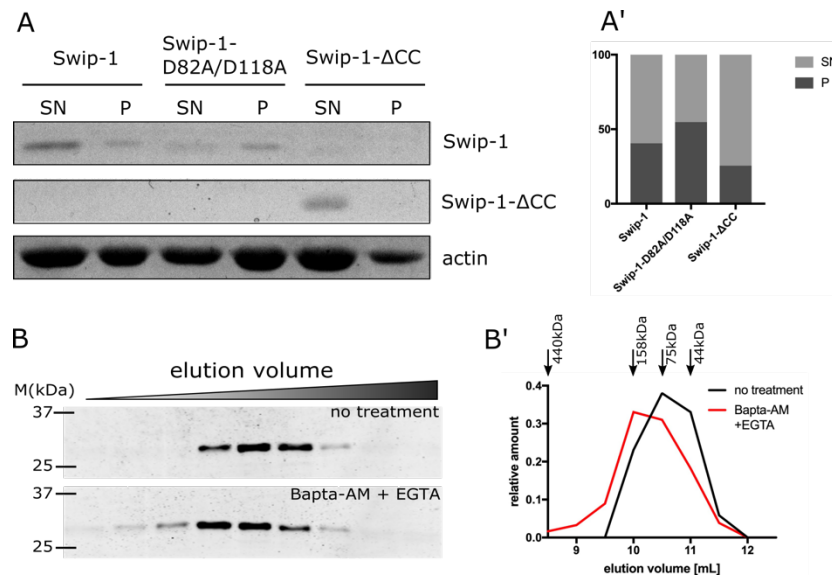


**Figure 9 – Swip-1's binding of calcium impacts F-actin co-sedimentation and apparent complex size.** (A) Co-sedimentation of Swip-1 variants with F-actin in a low-speed pelleting assay at 10,000xg. The proteins in the supernatant (SN) and the pellet (P) fractions were stained with Coomassie blue. (A') Quantification of F-actin in supernatant (light grey) and pellet (dark grey) fractions from experiment shown in (A). (B) Western blot analysis of S2R<sup>+</sup> cell lysates after size exclusion chromatography. The blot was stained for Swip-1. Prior to lysis, cells were either treated with DMSO (no treatment, control) or 100 $\mu$ M Bapta-AM and 1mM EGTA for 16h. (B') Relative amount of Swip-1 in each fraction (elution volume) in (B) was determined densitometrically using ImageJ software. Elution volume of known molecular masses from calibration as indicated.

### 4.3 Swip-1 calcium binding and dimerization are necessary for lamellipodia-based migration of macrophages

To further investigate the necessity of  $\text{Ca}^{2+}$  binding and self-dimerization in migrating macrophages, rescue experiments with three transgenic Swip-1 variants were conducted:

Swip-1-D82A/D118A, Swip-1- $\Delta$ CC and additionally Swip-1- $\Delta$ EF which lacks the complete amino acid sequence of both EF-hands (aa74-137).

First, the localization of the Swip-1 variants was analyzed in fixed macrophages. Prepupal *swip-1* mutant macrophages re-expressing the Swip-1 variants were plated on ConA (Figure 10). Swip-1 full length protein is enriched in the lamellipodia (Figure 10A) while Swip-1-D82A/D118A and Swip-1- $\Delta$ CC localized more cytoplasmic and can only be seen scarcely along the leading edges (Figure 10B, C). Interestingly, the Swip-1-D82A/D118A variant was often seen enriched in thick bundles in the cell center which co-localized with F-actin bundles (Figure 10B').

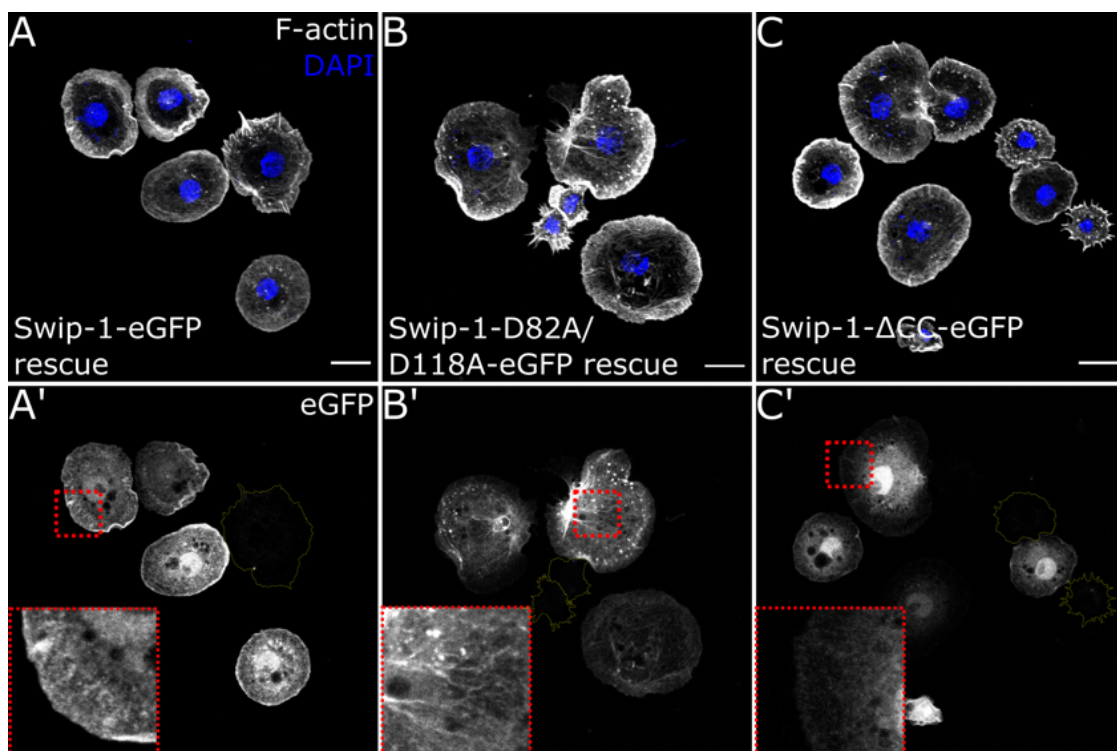


**Figure 10 – Localization of Swip-1 variants in ex vivo macrophages.** (A-C) Maximum intensity projection of confocal images of the actin cytoskeleton in *swip-1* mutant prepupal macrophages re-expressing (A) Swip-1-eGFP, (B) Swip-1-D82A/D118A-eGFP and (C) Swip-1- $\Delta$ CC-eGFP. Cells were plated on ConA and co-stained for F-actin (white) and DAPI (blue). (A'-C') Lower panel shows eGFP fluorescence of Swip-1 variants. Inlets in bottom panel are detailed images of red boxed areas showing changes in localization. Yellow outlines indicate mutant cells not expressing a Swip-1-eGFP fusion protein variant. Genotypes as indicated. Scale bars 10 $\mu$ m.

Next, the random migration of prepupal *swip* <sup>$\Delta$ 1</sup> macrophages re-expressing the Swip-1 variants was performed (Figure 11A). *swip-1* deficient macrophages migrated faster than wild-typic macrophages (Figure 11B). This also led to an increased displacement from origin (Figure 11B'). Neither re-expression of Swip-1- $\Delta$ EF nor Swip-1- $\Delta$ CC variant

could rescue the increased migration speed or displacement (Figure 11B, B'). Re-expression of the Swip-1-D82A/D118A variant did reduce both parameters analyzed. However, the live imaging showed that these macrophages actually cannot properly separate from one another resulting in a “tug-of-war”-like movement (see publication 1, figure 2n)

Lastly, the 3D directed migration of pupal *swip*<sup>Δ1</sup> macrophages was analyzed. *In vivo* laser ablation of a single cell triggers an immune response. Macrophages therefore switch from a random to a directed migration to the wound site and phagocytose the cell debris (Rüder et al., 2018). To analyze this mode of migration, the macrophages were tracked relative to the wound site. This allowed analysis of the directiveness of movement (Figure 11C). Compared to wildtype macrophages, *swip*<sup>Δ1</sup> macrophages showed similar migration speed, directiveness (biased angle) and persistence of migration (Figure 11D).

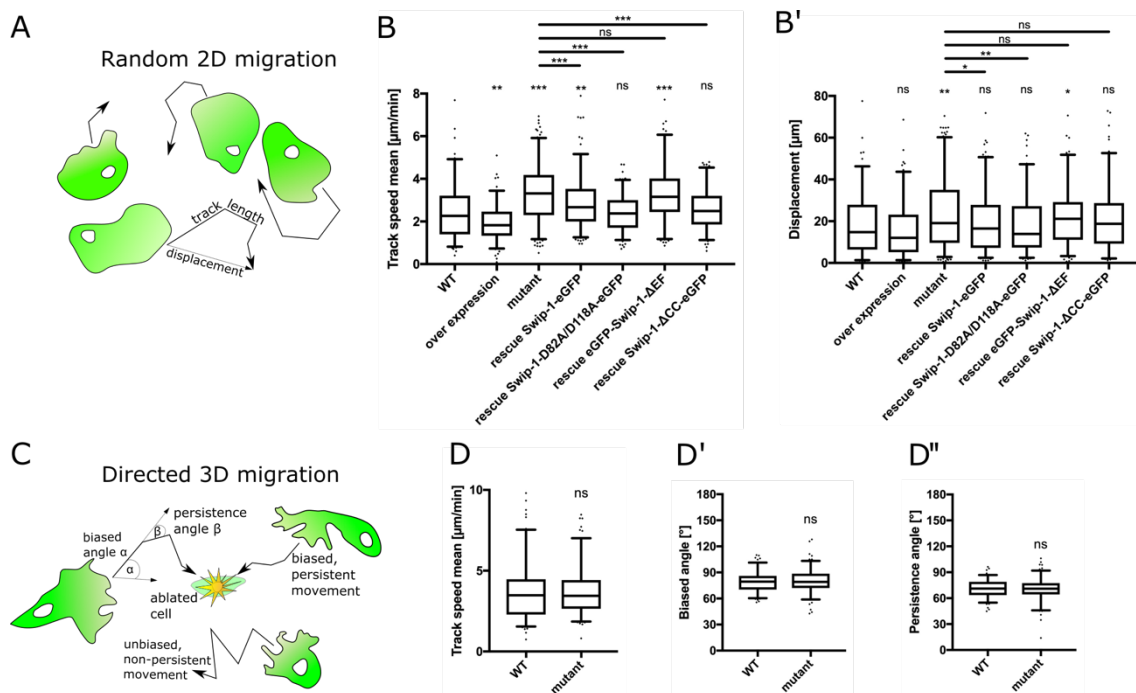


**Figure 11 – Loss of *swip-1* leads to increased velocity of randomly migrating macrophages.** (A) Scheme of random 2D migration. Parameters of analysis are indicated. (B) Quantification of track speed mean and (B') displacement of randomly migrating macrophages of indicated genotypes.  $n =$  WT: 114, OE: 133, *swip-1* mutant: 206, rescue WT: 166, rescue *Swip-1-D82A/D118A*: 136, rescue *Swip-1-ΔEF*: 130, rescue *Swip-1-ΔCC*: 135 tracks. (C) Scheme of directed 3D migration after single cell ablation. Parameters of analysis are indicated. (D) Quantification of track speed mean, (D') biased angle and (D'') persistence angle of wildtype and *swip-1* mutant macrophages migrating to a wound.  $n =$  WT: 130, *swip-1* mutant: 152 tracks. (B, D) Mann–Whitney test,  $P$  value: 0.12 (ns), 0.033 (\*), 0.002 (\*\*), <0.001 (\*\*\*).

#### 4.4 Active non-muscle myosin II has a different localization pattern in macrophages depending on Swip-1 protein levels

Cell migration is also dependent on traction force transmission generated by F-actin polymerization and actomyosin contraction as shown in the molecular clutch hypothesis. Focal adhesions are special sites of clustered integrins that bind to the ECM and therefore attach a cell to the matrix. Swip-1 has been shown to be a specific adaptor for clathrin-independent endocytosis of integrins (Moreno-Layseca et al., 2021). *swip-1* deficient *Drosophila* macrophages plated on the ECM protein vitronectin (VN) displayed an increased cell size and focal contact length (Publication 1, supplemental figure 2). It is known that maturation of nascent focal contacts to mature focal adhesions depends on myosin contraction (Gardel et al., 2010). Therefore, the distribution of active non-muscle myosin II in *Drosophila* macrophages was analyzed.

Active NMII can be detected by a specific antibody against the S19 phosphorylation of MRLC (anti-pMRLC). Wild-typic, Swip-1 over-expressing and *swip-1* mutant macrophages were plated on ConA and stained for active NMII (Figure 12). In wildtype polarized macrophages, active NMII is predominantly located opposite of the leading edge where actin stress-fibers are present (Figure 12A). Macrophages over-expressing Swip-1 often did not display this enrichment of actin stress fibers and active NMII (Figure 12B). Similarly, *swip-1* mutant macrophages also displayed no actin stress fibers with enriched active NMII. However, the anti-pMRLC staining revealed active NMII localization throughout the cell (Figure 12C).

#### 4.5 Loss of Swip-1 impairs actomyosin contraction of secretory vesicles

In order to investigate the relationship of Swip-1 and myosin, the well-described process of regulated exocytosis in *Drosophila* salivary glands was investigated. This process is highly dependent on actomyosin contraction. Correspondingly, Swip-1 expression data also showed a high abundance of Swip-1 protein in adult and larval salivary glands (Leader et al., 2018). Therefore, the *swip*<sup>Δ1</sup> mutant was further characterized in the well-established model system of the *Drosophila* larval salivary glands.

The larval salivary glands are two interconnected tubes of a single layer of epithelial cells. These cells secrete high levels of glue proteins packed in large vesicles. The secretion process is induced by a pulse of the hormone 20-hydroecdysone (20E). This leads to

vesicle fusion with the apical membrane and contraction of an actomyosin coat of the vesicles (Biyasheva et al., 2001; Merrifield, 2016).

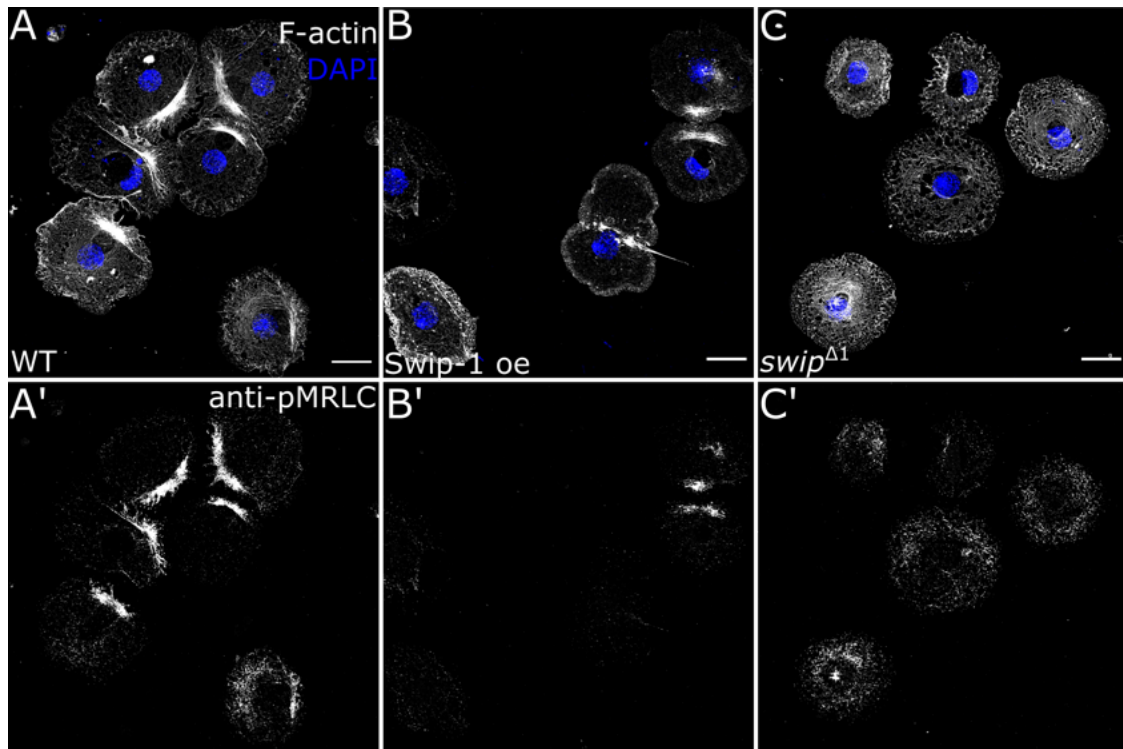


**Figure 12 – Localization of active non-muscle myosin II is dependent on Swip-1 expression.** (A-C) Confocal images of a fixed prepupal macrophages of (A) wildtype, (B) Swip-1 overexpressing and (C) swip-1 mutants stained for F-actin (white), DAPI (blue) and phospho-myosin regulatory light chain (pMRLC) at S19 (white, bottom panel A'-C'). Note that pMRLC staining was imaged with identical excitation laser intensity and adjusted to same grey level values for all images shown. Scale bars 10 $\mu$ m.

In *swip* <sup>$\Delta$ 1</sup> *ex vivo* larval salivary glands, the vesicle size is not changed compared to wildtype (Figure 13A). However, the duration of secretion was found significantly prolonged (Publication 2, figure 3K). It has been shown that the contraction of the vesicle membrane leads to so called crumpling of the membrane (Kamalesh et al., 2021). In order to determine if the increased time needed for secretion is caused by less contraction of the actomyosin coat, this membrane crumpling was analyzed.

Fusing vesicles of salivary glands expressing Lifeact-GFP were imaged in a parallel z-plane to the lumen (top view; see publication 2, figure 1E for explanation of imaging planes). The membrane circularity of individual vesicles was measured in a cross-section over time of secretion (Figure 13B). The circularity of wild-typic fusing vesicle initially decreased due to membrane crumpling but subsequently increased again towards completion of fusion. In *swip-1* mutant salivary glands, a higher circularity throughout the fusion process indicated less membrane crumpling (Figure 13B'). Note that the time of secretion for *swip* <sup>$\Delta$ 1</sup> salivary glands was significantly longer (also see publication 2,

figure 3K). Therefore, the circularity was measured in longer intervals (every 30s) compared to wildtype (every 10s).

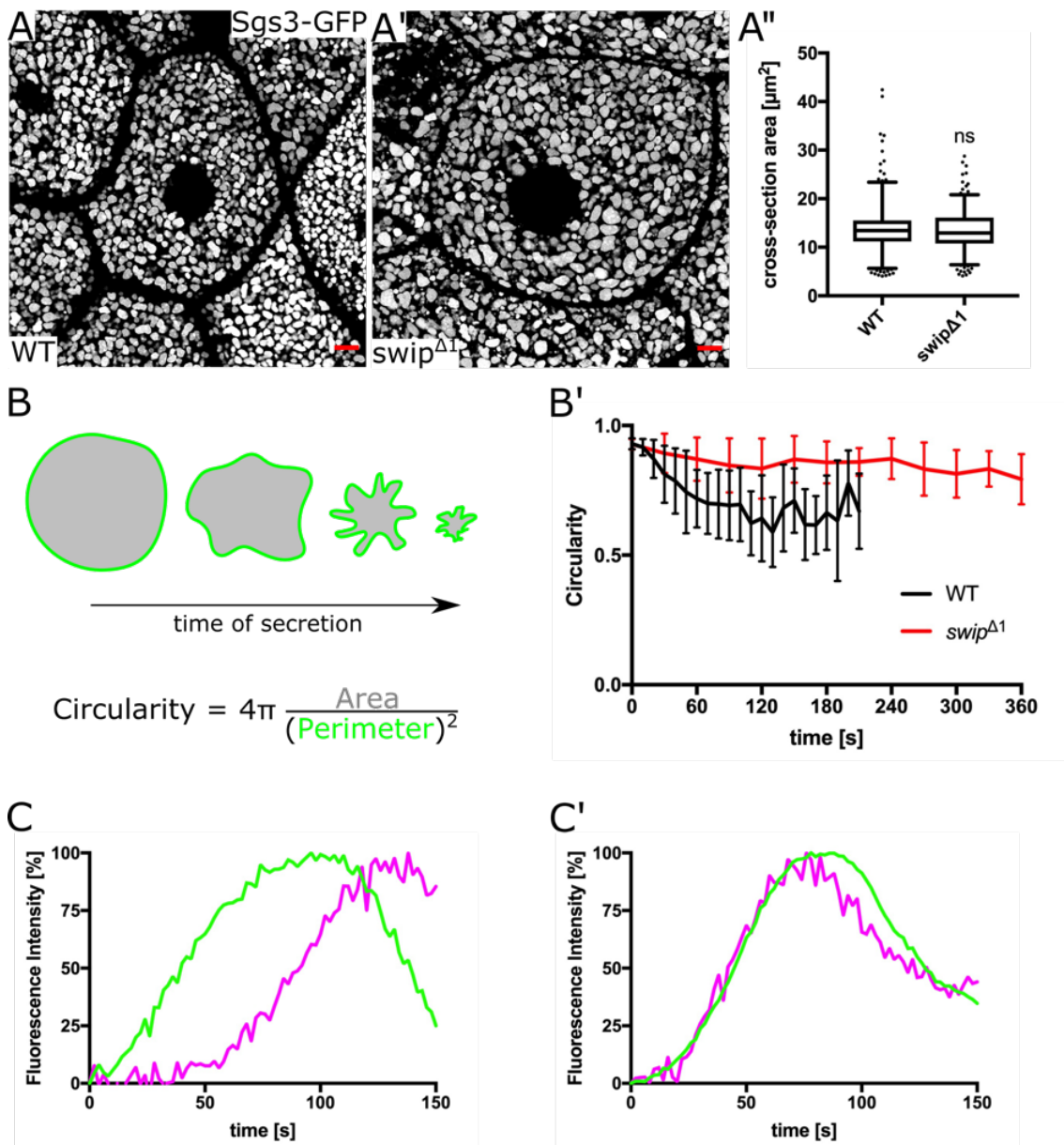


**Figure 13 – Loss of *swip-1* reduces secretion efficiency by acting on the crumpling of vesicle membrane.** (**A**, **A'**) Representative confocal images of epithelial cells of larval salivary glands expressing *Sgs3-GFP* (white) in their packed vesicles. Genotypes as indicated. Scale bars (red) 5 $\mu$ m. (**A''**) Distribution of cross-section area of three z-planes for each cell was calculated.  $n = 3$  salivary glands with 3 analyzed cells for each genotype. Mann–Whitney test,  $p$ -value > 0.12 (ns). (**B**) Analysis of vesicle crumpling during exocytosis. Single secreting vesicles of salivary glands expressing *Lifact-GFP* transgene were followed and traced as shown schematically. (**B'**) Circularity of the vesicles was measure over time.  $n=20$  vesicles from four glands of each genotypes. (**C**) Representative graph of *Lifact* (green) and non-muscle myosin II (magenta) recruitment to the vesicle membrane of wildtype and (**C'**) *swip-1* mutant secretory larval salivary glands.

The reduced crumpling in *swip-1* mutant salivary glands prompted the question if this is caused by a decreased NMII activity in the actomyosin coat of the fusing vesicles.

Therefore, secreting larval salivary glands were dissected and stained with the anti-pMRLC antibody. Surprisingly, *swip*<sup>Δ1</sup> salivary glands showed an increase of phosphorylated MRLC at the membrane of secreting vesicles (Publication 2, figure 4). Consequently, the recruitment of NMII to the vesicle membrane was analyzed in live imaging of secreting salivary glands. *spaghetti squash* (*sqh*) encodes the *Drosophila* myosin light chain. Live imaging of *ex vivo* salivary glands expressing fluorescently tagged Lifeact and *sqh* revealed a premature recruitment of NMII to the membrane of secreting vesicles in *swip*<sup>Δ1</sup>. On average, NMII was detected  $11.7 \pm 27.2$ s after F-actin at fusing vesicle (Figure 13C') compared to  $53.0 \pm 29.9$ s in wildtype salivary glands (Figure 13C).



## 5 Discussion

### 5.1 Swip-1 is highly expressed in tissues that require dynamic calcium-dependent actin remodeling

In *Drosophila* Swip-1 is expressed in various tissues with very high expression in the larval and adult central nervous system and moderately high to very high expression in the larval and adult salivary gland (Leader et al., 2018). Swip-1 was also shown to be expressed in embryonic macrophages (Hornbruch-Freitag et al., 2011) and our bulk RNAseq data revealed an upregulation during metamorphosis when macrophages transition from a sessile to a highly migratory state (Publication 1). The established model systems of *in vivo Drosophila* prepupal macrophages (Rüder et al., 2018), *ex vivo* larval salivary glands (Biyasheva et al., 2001; Tran & Ten Hagen, 2017) and the novel *in vivo* wound closure model of larval epidermal cells (Publication 1) allowed the dissection of Swip-1's role in these tissues by analyzing the associated Ca<sup>2+</sup>-dependent processes of migration, wound closure and regulated exocytosis.

### 5.2 Swip-1 cross-links F-actin in a calcium-dependent manner

Swip-1 is a Ca<sup>2+</sup>-binding protein that could be shown to cross-link F-actin *in vitro*. These cross-links are stable in the absence but transient in the presence of Ca<sup>2+</sup>. The resulting dynamic cross-linking by Swip-1 seems to be essential for the rapid changes of the actin cytoskeleton which are necessary for dynamic processes such as lamellipodia formation during cell migration and wound closure (Publication 1).

Using the Swip-1-D82A/D118A variant further underlined the Ca<sup>2+</sup> dependent F-actin cross-linking activity. The mutated aspartates were shown to be essential for the stereochemistry of the EF-loop and its ability to coordinate the Ca<sup>2+</sup> ions correctly (Ferrer-Acosta et al., 2013). Total internal reflection microscopy (TIRF-M) as well as low-speed actin co-sedimentation assay of Swip-1-D82A/D118A showed comparable results to Swip-1 treated with EGTA (Publication 1).

It has been shown that both EF-hand domains of human EFHD2 bind a Ca<sup>2+</sup> ion (Hagen et al., 2012; K. R. Park et al., 2016; Vega et al., 2008). However, different results concerning its affinity to calcium have been published. Isothermal titration calorimetry experiments with EFHD2 mutated in either one EF-hand determined K<sub>D</sub> values of EF-hand 1 with 96 ± 15nM and EF-hand 2 with 70 ± 1nM (K. R. Park et al., 2016). Yet, the authors suggested that *in vivo* the affinity of both EF-hands to Ca<sup>2+</sup> could be lower than measured. They suggested that at

resting levels no  $\text{Ca}^{2+}$  is bound to EFHD2. A second study using  $\text{Ca}^{2+}$  equilibrium centrifugation determined a  $K_D$  value of  $110\mu\text{M}$  (Hagen et al., 2012) which is significantly higher than the isothermal titration calorimetry experiment showed. Here, the authors proposed that EFHD2 might relay  $\text{Ca}^{2+}$  signals within the cell similar to calmodulin (Chin & Means, 2000). Therefore, *Drosophila* Swip-1 could act as a  $\text{Ca}^{2+}$  sensor protein locally responding to the transient changes of  $\text{Ca}^{2+}$  concentration such as at the leading edge of migrating cells or after wounding in an epidermal sheet (Hagen et al., 2012; Mielenz & Gunn-Moore, 2016).

We have also found that, like *Drosophila* Swip-1, human EFHD2 cross-links F-actin in  $\text{Ca}^{2+}$ -dependent manner but additionally exhibits a  $\text{Ca}^{2+}$ -independent F-actin bundling activity. This finding is contrary to prior studies. It has been previously published that EFHD2 bundles F-actin and this activity is induced by  $\text{Ca}^{2+}$  binding to the EF-hand domains. However, high protein concentrations of EFHD2 had been used. For example,  $1\mu\text{M}$  GST-EFHD2 incubated with F-actin *in vitro* showed a F-actin network with some loose parallel bundles (Huh et al., 2013) and  $4\mu\text{M}$  GST-EFHD2 induced thick F-actin bundles (M.-S. Kwon et al., 2013). We found these concentrations to be non-physiological (Publication 1).

Actually, the concentration of a cross-linking protein has been shown to be crucial for its function (Lieleg et al., 2010). For example, the cross-linker  $\alpha$ -actinin has been shown to bundle F-actin at high concentrations (Lieleg et al., 2010; Tseng et al., 2002). Thus, *in vitro* experiments are an important tool to investigate the mechanisms of a protein in a controlled environment. But the subsequent *in vivo* analysis of a protein in a physiological context with regulating mechanisms in place adjusting for example the protein concentration, is crucial for our understanding of how proteins function.

It has to be kept in mind that in this present work, transgenes with a fluorescence tag, mostly GFP, were introduced to visualize Swip-1 *in vivo*. GFP and Swip-1 have almost identical sizes of about 25kDa and no additional linker between C-terminus of Swip-1 and N-terminus of GFP had been introduced. Even though the fluorophore could potentially interfere with the dimerization capability of Swip-1, throughout this work, rescue experiments with a full-length Swip-1 tagged C-terminally with GFP have been successful.

### **5.3 Loss of *swip-1* increases macrophage random migration through stabilization of focal adhesions**

Using CRISPR/Cas9 genome editing technique (Gratz et al., 2015) a *Drosophila* fly line lacking Swip-1 protein has been successfully established. Remarkably, the flies are viable and fertile as previously reported for EFHD2 knock out mice (Brachs et al., 2014; Morowski et al., 2014).

Site specific introduction of Swip-1 variant transgenes into the *Drosophila* genome allowed rescue experiments and further dissecting the role of  $\text{Ca}^{2+}$  binding *in vivo*.

*swip-1* mutant macrophages displayed an increased speed of random migration but unchanged directed migration behavior. Re-expression of eGFP-Swip-1- $\Delta$ EF failed to rescue the random migration phenotype. It has been suggested that the first EF-hand domain contains an actin binding site (ABS) because deletion of the EF-hand domains was shown to not only diminish  $\text{Ca}^{2+}$  binding but also F-actin binding (Moreno-Layseca et al., 2021).

Surprisingly, Swip-1- $\Delta$ CC-eGFP was able to rescue the increased random migration speed of *swip-1* deficient macrophages. This suggests that *in vivo* dimerization of Swip-1 is not required for lamellipodia formation. However, *in vitro* low speed actin co-sedimentation assay showed that removal of the CC-domain also abolishes co-sedimentation of F-actin. It could be possible that in the absence of full length Swip-1, F-actin is cross-linked and stabilized by a different actin cross-linker due to F-actin cross-linker redundancy *in vivo*.

Nevertheless,  $\text{Ca}^{2+}$  binding of Swip-1 is required for proper random migration of *Drosophila* macrophages. Rescue of the *swip-1* mutant by re-expressing the  $\text{Ca}^{2+}$  binding-deficient Swip-1-D82A/D118A variant resulted in macrophages unable to separate from each other. Antibody staining of the  $\beta$ PS-integrin *myspheroid* of macrophages plated on VN revealed enlarged focal adhesions between the cells and the underlying ECM (Publication 1). It has been recently shown that EFHD2-silenced human breast adenocarcinoma cells also accumulate focal adhesions. There, EFHD2 was found to directly interact with Rab21 for clathrin-independent endocytosis of integrins coupling the endosomes to the actin cytoskeleton. It is therefore possible that in *Drosophila* macrophages,  $\text{Ca}^{2+}$  binding and sensing by Swip-1 is involved in focal adhesion turnover.

Consistently, 2D random migration of prepupal macrophages is an integrin-dependent process (Moreira et al., 2013). Therefore increased adhesion of *swip-1* deficient macrophages could lead to an increased migration speed as has been shown for *zyxin* knock down macrophages (Moreira et al., 2013). Concurrently, less focal contacts were observed in monkey kidney fibroblasts overexpressing the actin cross-linkers T- and L-plastin (Arpin et al., 1994). Also, the S100P of the EF-hand containing S100 protein family was shown to dissociate focal adhesion sites and NMIIA filaments in rat mammary and HeLa cells (Du et al., 2012).

It has to be kept in mind that myosin contractility is necessary for focal adhesion maturation (Vicente-Manzanares et al., 2009). Moreover, for activation, NMII needs to be phosphorylated at S19. This phosphorylation can be achieved through the Rho-associated kinase (ROCK) that is a downstream target of RhoA. It was shown that overexpression of EFHD2 in B16F10

melanoma cells acts on small Rho GTPase activity. While Rac and Cdc42 activity increased, RhoA activity was reduced. Concomitantly, knock down of EFHD2 expression increased RhoA activity (Huh et al., 2015). Similarly, overexpression of EFHD2 in CHO-K1 cells increased Rac activity (M.-S. Kwon et al., 2013) which act antagonistically to RhoA. Therefore, loss of EFHD2/Swip-1 could lead to activation of RhoA which in turn leads to more active NMII and thus focal adhesion maturation and stability.

#### **5.4 Proposed model for Swip-1 function in lamellipodia formation for 2D cell migration**

Local changes of  $\text{Ca}^{2+}$  concentration direct a cell's movements. Swip-1 plays a central role in the underlying necessary dynamic rearrangements of the F-actin network. Here, I propose a model of a possible underlying pathway leading to Swip-1-dependent dynamic lamellipodia formation (Figure 15).

Swip-1 is an F-actin cross-linking protein whose cross-links are stable in the absence of  $\text{Ca}^{2+}$  but become transient when  $\text{Ca}^{2+}$  levels increase. The transient cross-links relax the F-actin network allowing severing proteins to generate new barbed ends. Subsequently, new filaments are polymerized by the Arp2/3-complex. Locally increased  $\text{Ca}^{2+}$  concentration during migration lead to the dynamic rearrangement of the F-actin network in the lamellipodium. The  $\text{Ca}^{2+}$  signal also induces a positive feedback loop by activating the F-actin severing protein gelsolin (H. Q. Sun et al., 1999) and stimulating PKC activity (Huang, 1989). PKC is a potential kinase involved in EFHD2 translocation to the plasma membrane (and will be discussed later). Furthermore, Swip-1 locally inhibits RhoA activity at the membrane resulting in increased Rac and therefore promoting Arp2/3-complex activity. However, local inhibition of RhoA also leads to less active non-muscle myosin II (Z. Sun et al., 2016) and therefore contractility. The contractility of an F-actin network is determined by its connectivity and has to be carefully balanced. By binding of NMII filaments to actin it also acts as a crosslinker. Loss of *swip-1* leads to an imbalance and reduced contractility because it alters the F-actin to myosin ratio while overexpression of Swip-1 leads to Arp2/3-complex overactivation and therefore large lamellipodia. Lastly, increased levels of active myosin can also lead to focal adhesion stability.

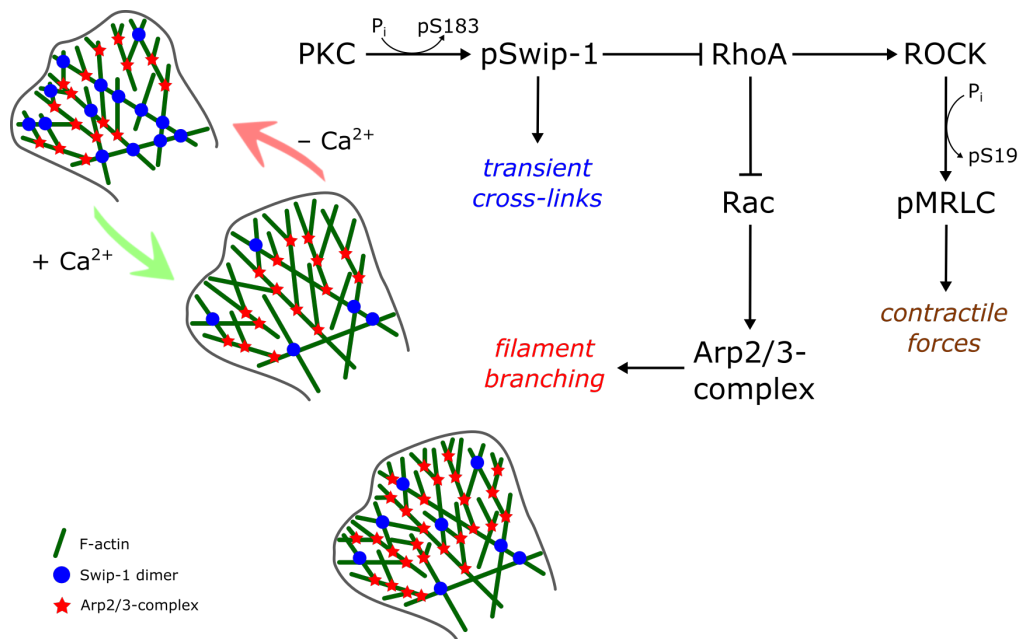


**Figure 14 – Model for Swip-1's function in lamellipodia formation.** Shown are the proposed Ca<sup>2+</sup>-dependent crosslinking activity as well as a possible pathway of Arp2/3-complex and non-muscle myosin II regulation. Swip-1 cross-links become transient in the presence of calcium. This relaxes the actin meshwork allowing Arp2/3-complex to bind and polymerize new filament branches. Decrease of calcium levels leads to stabilization of the new F-actin network. Simultaneously, Swip-1 activity inhibits RhoA. This leads to further activation of Arp2/3-complex via Rac and reduced myosin activation via ROCK activity.

## 5.5 Wound closure is dependent on Swip-1 transient F-actin cross-links

In this present work, I established a novel wound closure model of *Drosophila* larval epidermis cells (Publication 1). Laser ablation of a single cell triggers a Ca<sup>2+</sup> wave that is rapidly propagated across several cell rows away from the wound site and lasts for about 15min. In multicellular epidermis wounds, it has been shown that the initial influx of Ca<sup>2+</sup> in the cell surrounding the wound is dependent on the transient receptor potential channel M (TRPM) (Antunes et al., 2013). The subsequent propagation of the Ca<sup>2+</sup> signal was shown to be dependent on gap junctions composed of *Drosophila* innexins (Razzell et al., 2013). Further, it has been shown that the amplitude of a Ca<sup>2+</sup> signal correlates with wound size (Razzell et al., 2013). Therefore, different wound sizes might evoke different cellular responses. Analysis of wound closure after single cell wounding in the epidermis has, to my knowledge, not been performed so far.

The increase of Ca<sup>2+</sup> in the cells surrounding the wound induces massive cytoskeletal rearrangements that are dependent on Swip-1 function. It could also lead to activation of severing proteins, such as gelsolin, to supply G-actin to the wound edge (Antunes et al., 2013). Most strikingly, Swip-1 localized to the forming lamellipodium at the wound edge that drives the initial phase of wound closure. Later Swip-1 was also seen in the actin cable around the

wound that contracts, closing the wound further. Concurrently, loss of *swip-1* dramatically reduced wound closure. Rescue by re-expression of the Ca<sup>2+</sup> binding-deficient Swip-1-D82A/D118A variant also failed, demonstrating the Ca<sup>2+</sup> dependency of Swip-1's function in wound closure (Publication 1).

The F-actin rearrangements in the cells surrounding the wound could also temporally reduce their adhesion to the underlying ECM. In order to regain tissue integrity, the cells need to migrate over the wound to close it. Disassembly of adhesion could aid this migration (Nakamura et al., 2018). Since *swip-1* mutant macrophages displayed more mature, stable focal adhesions, this could also explain a reduced migratory response after wounding of larval epidermis cells. This has not been analyzed, yet.

Furthermore, it was shown that NMII was recruited to the rear end of more distal cells to the wound (Abreu-Blanco et al., 2011). The polar localization of NMII could direct the movement of the epidermis cells towards to wound (Y. C. Kwon et al., 2010; Wu et al., 2009). Loss of *swip-1* in macrophages showed active NMII localization across the entire cell. This would suggest that also in larval epidermis cells of *swip*<sup>Δ1</sup>, after wounding, NMII is not properly recruited to the distal end of the cells causing an uncoordinated cell movement of the epidermal sheet that is not directed towards the wound site.

It was shown in pinch wounds of larval epidermis that wound closure required Rac and Cdc42 but not RhoA (Lesch et al., 2010). However, in our novel single cell wounding model, overexpression of CYRI, a Rac inhibitor (Fort et al., 2018), suggests that the contractility of the actin cable is the major force pulling the wound edge close. These cells generate no lamellipodium but could still close the single cell wound (Zedler et al., in preparation). Also, *Drosophila* embryos deficient for Rac1, Rac2 and Mtl were still able to close a laser-induced wound entirely (Wood et al., 2002). Further dissecting the role of Rho GTPases in our novel model system is needed. Importantly, single cell wounds in the larval epidermis are easily reproducible and the large cell size of up to 100μm across allow detailed imaging of the forming lamellipodia protrusions.

For instance, the role of RhoA needs to be investigated. As described above, RhoA could be a target of Swip-1 to regulate actin polymerization and myosin activity. It has also been shown to be essential for actin cable formation in dorsal closure and syncytial embryo wound closure (Abreu-Blanco et al., 2014; Wood et al., 2002). Therefore, imaging of the RhoA-GTP-sensor AniRBD-GFP (Munjal et al., 2015) in the single cell larval epidermis wound closure model could elucidate the role of this Rho GTPase.

Interestingly, Swip-1- $\Delta$ CC rescue seemed to close the wound in the first 15min of observation, but then failed to fully constrict the wound edge close and could not be seen in the actin cable surrounding the wound edge (Publication 1). In the first approximately 10min of wound closure broad lamellipodial protrusions of the cells adjacent to the wound are formed. It is therefore possible that, like in randomly migrating macrophages, Swip-1's function for lamellipodia stabilization is compensated for by a different actin cross-linking protein. But when the wound closure mechanism shifts to contraction of an actomyosin ring, proper dimerization of Swip-1 might be essential for the appropriate force generation.

## 5.6 Swip-1 is necessary for regulated exocytosis

Another  $\text{Ca}^{2+}$ -dependent process that requires actomyosin contraction is the exocytosis of glue granules in *Drosophila* larval salivary glands. This regulated exocytosis involves the recruitment of actin regulators and constriction of the vesicle membrane to expulse the cargo into the salivary gland lumen.

It was previously suggested that Swip-1 regulates Arp2/3-independent exocytosis of electron-dense vesicles during myoblast fusion (Hornbruch-Freitag et al., 2011). Also, high throughput RNAseq data showed high expression levels of Swip-1 in *Drosophila* larval salivary glands (Leader et al., 2018).

In *Drosophila* salivary glands, secreting vesicles are coated with an F-actin network promoted by the formin Dia, the nucleation promoting factor WASP and the Arp2/3-complex (Rousso et al., 2016; Tran et al., 2015). Swip-1, like F-actin, located to the apical membrane of the secreting epithelial salivary gland cells. Prior to fusion, both F-actin and Swip-1 are cleared from the fusion site. Upon vesicle fusion, Swip-1 and F-actin coat the vesicle simultaneously (Publication 2). Loss of *swip-1* resulted in overall prolonged exocytosis while average vesicles size was not affected. However, reduced membrane crumpling suggests a decrease of actomyosin contractility at the vesicle membrane to efficiently expulse the cargo.

Re-expression of the dimerization incapable Swip-1- $\Delta$ CC variant in *swip-1* deficient salivary glands could not rescue the retarded secretion. This suggests that Swip-1 cross-linking is crucial for its function in this regulated exocytosis. Here, unlike in lamellipodia, the cross-linking activity does not seem to be compensated for by other cross-linking proteins.

By using surface micropatterning of actin and numerical simulations it was shown that actomyosin contractility depends on its connectivity (Ennomani et al., 2016). According to these findings, addition of a cross-linker, such as Swip-1, would reduce the contractility of the F-actin network around a fusing vesicle. However, loss of either *swip-1* or Swip-1's cross-

linking capability (Swip-1- $\Delta$ ACC rescue) led to a prolonged exocytosis possibly due to lower contractility.

It could be shown that *swip-1* deficient salivary glands have increased amounts of active NMII, as shown by anti-pMRLC staining, and also recruit NMII prematurely to the vesicle membrane (Publication 2). Binding of NMII to F-actin also adds to the cross-linking of the actin filaments. Therefore, there could be a tightly regulated balance of F-actin to Swip-1 and NMII for most efficient secretion. Disruption of this balance might lead to the observed reduction of contractility at the membrane of the secreting vesicles.

Moreover, it was shown that a continuous cycle of F-actin assembly and turnover is necessary for effective secretion. RhoA undergoes a negative feedback regulation by F-actin and can promote this necessary cycling (Segal et al., 2018). Since Swip-1 was also shown to affect F-actin depolymerization through cofilin (Huh et al., 2013), it might have an additional effect on F-actin turnover during vesicle constriction.

Taken together, the regulated exocytosis of *Drosophila* larval salivary gland granules could depend on a highly controlled actin contraction governed by defined ratios of (1) a cross-linked F-actin network by Swip-1, (2) NMII to exert contractile forces and (3) cofilin for F-actin depolymerization. This would allow a mechanism of sliding of actin and myosin along each other while Swip-1 provides the necessary network stability and cofilin reduces the size of the vesicle's actin coat during secretion (Publication 2).

Noteworthy, rescue experiments of the *swip-1* mutant were successful with the Ca<sup>2+</sup>-binding deficient Swip-1-D82A/D118A variant. This suggests that Swip-1's function in exocytosis is independent of its Ca<sup>2+</sup> binding and that possibly only Swip-1-mediated stable F-actin cross-links are necessary. Previous findings showed elevated Ca<sup>2+</sup> levels 2 hours after 20E induction (Biyasheva et al., 2001). However, in our set-up of analyzing *Drosophila* larval salivary glands *ex vivo*, secretion could neither be induced by addition of the SERCA inhibitor Thapsigargin nor could 20E-induced secretion be abolished through chelating Ca<sup>2+</sup> intra- and extracellularly by Bapta-AM and EGTA, respectively (Publication 2).

### 5.7 Loss of *swip-1* might lead to increased non-muscle myosin activation

A murine brain interactome study revealed an interaction of EFHD2 with myosin heavy chain isoforms NMIIA and NMIIB (Soliman et al., 2021). This interaction seems to be conserved. In *Drosophila* an interaction study based on co-affinity purification coupled with mass spectrometry also showed an interaction of Swip-1 with zipper (*zip*), the *Drosophila* myosin heavy chain homolog (Guruharsha et al., 2011). In this work, antibody staining of



phosphorylated MRLC at S19 in *swip-1* mutants showed increased active NMII at secreting vesicles of larval salivary glands and strong staining but a non-polar distribution in macrophages.

It was found that an increased activation of NMII led to large actin bundles, stable adhesions as well as decreased protrusion (Vicente-Manzanares et al., 2009) and NMIIA-depleted CHO-K1 cells displayed broader lamellipodia than control cells (Vicente-Manzanares et al., 2007). These findings could explain the increased actin bundles observed in fixed Swip-1 RNAi-mediated knock down macrophages. as well as the broad lamellipodia all around the cell body of Swip-1 overexpressing cells (Publication 1).

It was shown in fish keratocytes that inhibition of NMII led to an increased retrograde flow rate (Jurado et al., 2005). Interestingly, it was suggested that this change in retrograde flow rate might not be a result of myosin dependent adhesion, as described in the molecular clutch model. Rather myosin's F-actin cross-linking activity leads to stiffening of the actin cytoskeleton reducing retrograde flow (Wolgemuth, 2005). Consequently, depriving *Drosophila* macrophages of Swip-1-mediated F-actin cross-linking would suggest that the actin retrograde flow is increased which results in increased retraction velocity. However, the opposite could be observed. The reduction in retraction velocity could, however, also be explained by increased F-actin cross-linking through overactivated NMII.

Furthermore, FRAP experiments of GFP-Actin in *swip*<sup>Δ1</sup> macrophages revealed a slightly decreased fractional recovery. CHO-K1 cells transfected with GFP-labeled NMII mutants that remain bound to actin, also showed a reduction of fractional recovery (Vicente-Manzanares et al., 2007) further supporting the notion that loss of *swip-1* leads to an overactivation of NMII and therefore increased NMII-mediated actin cross-linking.

## **5.8 Phosphorylation of human EFHD2 might act as a switch from F-actin bundling to cross-linking activity**

In human EFHD2 several phosphorylation sites for regulation have been identified. Three sites are located at the N-terminus (S74, S76, Y83) (M.-S. Kwon et al., 2013). However, only the tyrosine is conserved in *Drosophila* Swip-1. Cycles of phosphorylation and dephosphorylation of EFHD2 at these residues might be necessary for regular membrane dynamics and coordinated actin movements in lamellipodia (Huh et al., 2013).

Secondly, phosphorylation of S183 located in the LM helix of EFHD2 was shown to induced local re-coordination of the actin binding site in the EFHD2 dimer. This was shown to not affect F-actin binding but decrease its F-actin bundling activity (K. R. Park et al., 2017). Due to the

decreased F-actin bundling activity, the phosphorylation of EFHD2 at S183 was found to allow cofilin access to F-actin for depolymerization (Huh et al., 2013). Remarkably, it was also shown that this phosphorylation is needed to translocate EFHD2 to the lamellipodium in B16F10 melanoma cells (Huh et al., 2013).

Phosphorylation of EFHD2 at S183 might therefore be the molecular switch of F-actin bundling in stable structure in the cell center (e.g. stress fibers) and dynamic F-actin cross-linking in the lamellipodium. Together with the phosphorylation-induced recruitment of cofilin this could be potentially highly important for the  $\text{Ca}^{2+}$ -dependent rapid rearrangements of the F-actin network needed for processes like migration and wound closure. This could also explain, why *in vitro* experiments of EFHD2 only found F-actin bundles (Huh et al., 2013; M.-S. Kwon et al., 2013; K. R. Park et al., 2016).

Surprisingly, protein alignment of human EFHD2 and *Drosophila* Swip-1 showed that S183 corresponds to E160 in *Drosophila*. Chemically, the glutamate in Swip-1 is mimicking a phosphoserine. In TIRF microscopy, human EFHD2 was found to bundle F-actin in a  $\text{Ca}^{2+}$ -independent manner while *Drosophila* Swip-1 did not display any bundling and exclusively cross-linking activity (Publication 1). It could be possible, that Swip-1 does not require phosphorylation but instead constitutively cross-links F-actin dynamically in the lamellipodium.

Though the open question remains, why Swip-1 is not regulated by this phosphorylation site and only shows F-actin cross-linking activity. Possibly, more complex organism than *Drosophila* also require more intricate regulation of their proteins. Thus, evolutionary pressure might have led to the introduction of the phosphorylation sites in humans (Jin & Pawson, 2012). But why this has also led to a F-actin bundling activity, has yet to be addressed.

It has been suggested that protein kinase C (PKC) is the responsible kinase phosphorylating EFHD2 at S183. Notably, PKC can be stimulated by an increase of  $\text{Ca}^{2+}$  (Huang, 1989). Thus  $\text{Ca}^{2+}$ -dependent PKC activation could serve as a positive feed-back loop leading to more EFHD2 translocated to the plasma membrane. The *Drosophila* genome contains six different genes for PKC (Shieh et al., 2002). Hence, it would be interesting to see if a transgenic Swip-1-E160S variant or the human EFHD2 could be phosphorylated by an endogenous PKC in *Drosophila* and if this is sufficient to introduce the dual bundling/cross-linking activity.

## 5.9 Understanding how EFHD2/Swip-1 upregulation causes pathologies

Upregulation of EFHD2 is associated with several neurodegenerative diseases and invasive forms of cancer (Mielenz & Gunn-Moore, 2016). Abnormal kinase activities have been linked

to the increased EFHD2 activity. In this present work, phosphorylation of Swip-1 was not experimentally addressed but it has a big potential to further shed light on how  $\text{Ca}^{2+}$ -independent regulation of EFHD2/Swip-1 alters its function. For example, S74 at the N-terminus of EFHD2 was shown to be phosphorylated by cyclin-dependent kinase 5 (Cdk5) which is a hyperactivated kinase in tauopathies (Vázquez-Rosa et al., 2014).

Moreover, as discussed above, loss of *swip-1* protein function might promote MLRC phosphorylation. Interestingly, abnormal NMII activity is likewise associated with neurological disorders such as schizophrenia. Concurrently, investigations of novel therapeutic approaches to treat Alzheimer's or Parkinson's disease have included the use of ROCK inhibitors (Brito & Sousa, 2020).

Secondly, the apparent impact on focal adhesion turnover could be the mechanism promoting abnormal cell motility of invasive cancer types. Release of cancerous cells from the underlying ECM by focal adhesion disassembly could promote their translocation. Therefore, upregulation of EFHD2/Swip-1 could promote this first step in the metastatic cascade.

Further studies of how EFHD2/Swip-1 is involved in regulatory pathways can help to understand the underlying mechanism causing the pathologies associated with upregulated EFHD2/Swip-1.

## 6 Conclusion and Outlook

In this work, Swip-1 was identified as a novel actin cross-linking protein. While often redundant, each F-actin cross-linker occupies a specific niche of cross-linker length, thus individually altering the properties of the F-actin cytoskeletal network. The collaborative interaction of several cross-linking proteins with F-actin in a dynamic network can spatiotemporally adjust the mechanical and viscoelastic properties of the cell. Here, I showed how  $\text{Ca}^{2+}$  signaling affects the F-actin cross-linking by Swip-1 needed for dynamic actin-remodeling in migration and wound closure, how vesicles coated with Swip-1 cross-linked F-actin can efficiently secrete their cargo and discussed its potential regulatory function for myosin activation and contraction. My results suggest multiple  $\text{Ca}^{2+}$ -dependent functions of Swip-1 from lamellipodia formation, cell-matrix adhesion turnover to actomyosin contractility. However, much is left to be addressed.

Firstly, how does Swip-1 protein level and function affect myosin? Here, the pathway in which Swip-1 is involved and what downstream effectors are potentially regulated to modify the phosphorylation of MRLC have to be identified as well as possible differences of Swip-1 monomer versus Swip-1 dimer function. To address whether the proposed interactions are directly linked, pull down assays of Swip-1 with Rac and RhoA could be performed. Moreover, the RhoA sensor AniRBD-GFP allows to spatiotemporally visualize RhoA activity *in vivo* and could therefore prove to be a powerful tool to investigate alterations in the myosin activation pathway during migration, wound closure and exocytosis.

Moreover, rescue experiments of the overactivation of myosin due to loss of *swip-1* could be addressed by using pharmacological ROCK or myosin inhibitors like Y27632 or Blebbistatin, respectively. However, one has to keep in mind that activated myosin unfolds itself therefore changing its geometry which may also interfere with its transport to its site of requirement, a fact which is likely to contribute to the non-polar distribution shown in *swip* <sup>$\Delta$ 1</sup> macrophages. This may result in a phenotype due to mis-localization or activity at the wrong location rather than simply the overactivation itself.

Secondly, how is Swip-1 regulated by phosphorylation? Phosphorylation could affect cell adhesion and motility as well. For example, integrin-activated focal adhesion kinase (FAK) phosphorylates  $\alpha$ -actinin at its ABS reducing its affinity to actin (Sjöblom et al., 2008). This can therefore not only influence the mechanical properties of the F-actin network, but also regulate adhesion and thus cell motility. Human Swip-1 is phosphorylated possibly by PKC at an ABS that could act as a switch between loose bundles and cross-links. However, *Drosophila*

Swip-1 is lacking this regulatory site as a glutamate at the position of interest is structurally already mimicking the phosphoserine. Rescue experiments of the *swip-1* mutant with a the human EFHD2 or a Swip-1-E160S variant, as has been done for the Ca<sup>2+</sup>-binding-deficient variant Swip-1-D82A/D118A, could show if this regulation can be introduced in *Drosophila*. This would potentially allow easy characterization and manipulation of this and other phosphorylation sites with relatively quick screening options through the established *Drosophila* model systems.

Thirdly, the processes leading to effective wound closure seem to be dependent on how a wound is induced and how many cells are affected. Therefore, the novel single cell wounding assay of *Drosophila* larval epidermis needs to be further characterized. Genes and signal pathways involved in the mechanisms regulating Ca<sup>2+</sup> release and wave propagation as well as lamellipodia and actin cable formation need to be identified. Because of the simple genetic manipulations possible in *Drosophila*, the relatively easy handling of pupae omitting any anesthetic step and the sheer giant size of LEC for excellent visualization proves this system a powerful tool to dissect protein functions and gain more insight into wound closure regulation. Lastly, does Swip-1 also impact cell-cell adhesions through adherens junctions (AJ)? Human Swip-1 was found in a interactome study of E-cadherin (Guo et al., 2014). Staining of endogenous Swip-1 in *Drosophila* egg chambers revealed distinct localization in the follicular epithelium and in the migrating border cell cluster (data not shown). Since the actin cytoskeleton and myosin are also associated with these adhesions (Huveneers & de Rooij, 2013; Vicente-Manzanares et al., 2009), a possible involvement of Swip-1 in maintenance or remodeling of these structure is easily conceivable. Interestingly, AJs are also important to re-establish tissue integrity after wounding. During wound closure, E-cadherin anchors the contractile actomyosin ring to the plasma membrane to generate the necessary traction force to pull the wound edge close (Abreu-Blanco et al., 2011). Moreover, it was shown that in *Drosophila* embryos blocking endocytosis resulting in increased levels of E-cadherin, prevents actomyosin to efficiently close a wound (Hunter et al., 2015). Interestingly, during epithelial remodeling processes, AJs have been suggested to be involved in Rho GTPase recruitment (Takeichi, 2014). Therefore, investigating a possible interaction of Swip-1 with E-cadherin or AJ turnover in the novel wound closure model would be interesting.

All in all, the plethora of live-imaging techniques, easy genetic manipulation, the single copy of Swip-1 and the now available *swip-1* mutant might prove *Drosophila* an excellent model to further investigate Swip-1 function and regulation *in vivo*.

## 7 References

- Abreu-Blanco, M. T., Verboon, J. M., & Parkhurst, S. M. (2011). Cell wound repair in *Drosophila* occurs through three distinct phases of membrane and cytoskeletal remodeling. *Journal of Cell Biology*, *193*(3), 455–464. <https://doi.org/10.1083/jcb.201011018>
- Abreu-Blanco, M. T., Verboon, J. M., & Parkhurst, S. M. (2014). Coordination of Rho family GTPase activities to orchestrate cytoskeleton responses during cell wound repair. *Current Biology*, *24*(2), 144–155. <https://doi.org/10.1016/j.cub.2013.11.048>
- Adams, J. C. (2004). Roles of fascin in cell adhesion and motility. *Current Opinion in Cell Biology*, *16*(5), 590–596. <https://doi.org/10.1016/j.ceb.2004.07.009>
- Agarwal, P., & Zaidel-Bar, R. (2019). Principles of Actomyosin Regulation In Vivo. *Trends in Cell Biology*, *29*(2), 150–163. <https://doi.org/10.1016/j.tcb.2018.09.006>
- Antunes, M., Pereira, T., Cordeiro, J. V., Almeida, L., & Jacinto, A. (2013). Coordinated waves of actomyosin flow and apical cell constriction immediately after wounding. *Journal of Cell Biology*, *202*(2), 365–379. <https://doi.org/10.1083/jcb.201211039>
- Arpin, M., Friederich, E., Algrain, M., Vernel, F., & Louvard, D. (1994). Functional differences between L- and T-plastin isoforms. *Journal of Cell Biology*, *127*(6 II), 1995–2008. <https://doi.org/10.1083/jcb.127.6.1995>
- Avramidou, A., Kroczeck, C., Lang, C., Schuh, W., Jäck, H.-M., & Mielenz, D. (2007). The novel adaptor protein Swiprosin-1 enhances BCR signals and contributes to BCR-induced apoptosis. *Cell Death & Differentiation*, *14*(11), 1936–1947. <https://doi.org/10.1038/sj.cdd.4402206>
- Baek, S. H., Kwon, Y. C., Lee, H., & Choe, K. M. (2010). Rho-family small GTPases are required for cell polarization and directional sensing in *Drosophila* wound healing. *Biochemical and Biophysical Research Communications*, *394*(3), 488–492. <https://doi.org/10.1016/j.bbrc.2010.02.124>
- Belacortu, Y., & Paricio, N. (2011). *Drosophila* as a model of wound healing and tissue regeneration in vertebrates. *Developmental Dynamics*, *240*(11), 2379–2404. <https://doi.org/10.1002/dvdy.22753>
- Biyasheva, A., Do, T. V., Lu, Y., Vaskova, M., & Andres, A. J. (2001). Glue secretion in the *Drosophila* salivary gland: A model for steroid-regulated exocytosis. *Developmental Biology*, *231*(1), 234–251. <https://doi.org/10.1006/dbio.2000.0126>
- Blanchoin, L., Amann, K. J., Higgs, H. N., Marchand, J., Kaiser, D. A., & Pollard, T. D. (2000). Direct observation of dendritic actin filament networks nucleated by Arp2/3 complex and WASP/Scar proteins. *Nature*, *404*(6781), 1007–1011. <https://doi.org/10.1038/35010008>
- Blanchoin, L., Boujemaa-Paterski, R., Sykes, C., & Plastino, J. (2014). Actin Dynamics, Architecture, and Mechanics in Cell Motility. *Physiological Reviews*, *94*(1), 235–263. <https://doi.org/10.1152/physrev.00018.2013>
- Brachs, S., Turqueti-Neves, A., Stein, M., Reimer, D., Brachvogel, B., Bösl, M., Winkler, T., Voehringer, D., Jäck, H.-M., & Mielenz, D. (2014). Swiprosin-1/EFhd2 limits germinal center responses and humoral type 2 immunity. *European Journal of Immunology*, *44*(11), 3206–3219. <https://doi.org/10.1002/eji.201444479>
- Brito, C., & Sousa, S. (2020). Non-Muscle Myosin 2A (NM2A): Structure, Regulation and Function. *Cells*, *9*(7), 1590. <https://doi.org/10.3390/cells9071590>
- Brundage, R. A., Fogarty, K. E., Tuft, R. A., & Fay, F. S. (1991). Calcium gradients underlying polarization and chemotaxis of eosinophils. *Science*, *254*(5032), 703–706. <https://doi.org/10.1126/science.1948048>
- Chalovich, J. M., Chock, P. B., & Eisenberg, E. (1981). Mechanism of action of troponin . tropomyosin. Inhibition of actomyosin ATPase activity without inhibition of myosin

- binding to actin. *The Journal of Biological Chemistry*, 256(2), 575–578.  
<https://www.ncbi.nlm.nih.gov/pmc/articles/PMC3624763/pdf/nihms412728.pdf>
- Chin, D., & Means, A. R. (2000). Calmodulin: a prototypical calcium sensor. *Trends in Cell Biology*, 10(8), 322–328. [https://doi.org/10.1016/S0962-8924\(00\)01800-6](https://doi.org/10.1016/S0962-8924(00)01800-6)
- Chou, S. Z., & Pollard, T. D. (2019). Mechanism of actin polymerization revealed by cryo-EM structures of actin filaments with three different bound nucleotides. *Proceedings of the National Academy of Sciences of the United States of America*, 116(10), 4265–4274. <https://doi.org/10.1073/pnas.1807028115>
- Clapham, D. E. (2007). Calcium Signaling. *Cell*, 131(6), 1047–1058.  
<https://doi.org/10.1016/j.cell.2007.11.028>
- Cordeiro, J. V., & Jacinto, A. (2013). The role of transcription-independent damage signals in the initiation of epithelial wound healing. *Nature Reviews Molecular Cell Biology*, 14(4), 249–262. <https://doi.org/10.1038/nrm3541>
- Courtemanche, N. (2018). Mechanisms of formin-mediated actin assembly and dynamics. *Biophysical Reviews*, 10(6), 1553–1569. <https://doi.org/10.1007/s12551-018-0468-6>
- Dekraker, C., Boucher, E., & Mandato, C. A. (2018). Regulation and Assembly of Actomyosin Contractile Rings in Cytokinesis and Cell Repair. *Anatomical Record*, 301(12), 2051–2066. <https://doi.org/10.1002/ar.23962>
- Delanote, V., Vandekerckhove, J., & Gettemans, J. (2005). Plastins: Versatile modulators of actin organization in (patho)physiological cellular processes. *Acta Pharmacologica Sinica*, 26(7), 769–779. <https://doi.org/10.1111/j.1745-7254.2005.00145.x>
- Du, M., Wang, G., Ismail, T. M., Gross, S., Fernig, D. G., Barraclough, R., & Rudland, P. S. (2012). S100P dissociates myosin IIA filaments and focal adhesion sites to reduce cell adhesion and enhance cell migration. *Journal of Biological Chemistry*, 287(19), 15330–15344. <https://doi.org/10.1074/jbc.M112.349787>
- Dütting, S., Brachs, S., & Mielenz, D. (2011). Fraternal twins: Swiprosin-1/EFhd2 and Swiprosin-2/EFhd1, two homologous EF-hand containing calcium binding adaptor proteins with distinct functions. *Cell Communication and Signaling*, 9(1), 2.  
<https://doi.org/10.1186/1478-811X-9-2>
- Ennomani, H., Letort, G., Guérin, C., Martiel, J.-L., Cao, W., Nédélec, F., De La Cruz, E. M., Théry, M., & Blanchoin, L. (2016). Architecture and Connectivity Govern Actin Network Contractility. *Current Biology*, 26(5), 616–626.  
<https://doi.org/10.1016/j.cub.2015.12.069>
- Evans, J. H., & Falke, J. J. (2007). Ca<sup>2+</sup> influx is an essential component of the positive-feedback loop that maintains leading-edge structure and activity in macrophages. *Proceedings of the National Academy of Sciences of the United States of America*, 104(41), 16176–16181. <https://doi.org/10.1073/pnas.0707719104>
- Falke, J. J., & Ziemba, B. P. (2014). Interplay between phosphoinositide lipids and calcium signals at the leading edge of chemotaxing amoeboid cells. *Chemistry and Physics of Lipids*, 182, 73–79. <https://doi.org/10.1016/j.chemphyslip.2014.01.002>
- Ferrer-Acosta, Y., N. Rodriguez Cruz, E., del C. Vaquer, A., & E. Vega, I. (2013). Functional and Structural Analysis of the Conserved EFhd2 Protein. *Protein & Peptide Letters*, 20(5), 573–583. <https://doi.org/10.2174/0929866511320050011>
- Fort, L., Batista, J. M., Thomason, P. A., Spence, H. J., Whitelaw, J. A., Tweedy, L., Greaves, J., Martin, K. J., Anderson, K. I., Brown, P., Lilla, S., Neilson, M. P., Tafelmeyer, P., Zanivan, S., Ismail, S., Bryant, D. M., Tomkinson, N. C. O., Chamberlain, L. H., Mastick, G. S., ... Machesky, L. M. (2018). Fam49/CYRI interacts with Rac1 and locally suppresses protrusions. *Nature Cell Biology*, 20(10), 1159–1171.  
<https://doi.org/10.1038/s41556-018-0198-9>
- Fujii, T., Iwane, A. H., Yanagida, T., & Namba, K. (2010). Direct visualization of secondary structures of F-actin by electron cryomicroscopy. *Nature*, 467(7316), 724–728.

- <https://doi.org/10.1038/nature09372>
- Gardel, M. L., Schneider, I. C., Aratyn-Schaus, Y., & Waterman, C. M. (2010). Mechanical Integration of Actin and Adhesion Dynamics in Cell Migration. *Annual Review of Cell and Developmental Biology*, 26(1), 315–333.  
<https://doi.org/10.1146/annurev.cellbio.011209.122036>
- Geeves, M. A., Fedorov, R., & Manstein, D. J. (2005). Molecular mechanism of actomyosin-based motility. *Cellular and Molecular Life Sciences*, 62(13), 1462–1477.  
<https://doi.org/10.1007/s00018-005-5015-5>
- Giganti, A., Plastino, J., Janji, B., Van Troys, M., Lentz, D., Ampe, C., Sykes, C., & Friederich, E. (2005). Actin-filament cross-linking protein T-plastin increases Arp2/3-mediated actin-based movement. *Journal of Cell Science*, 118(6), 1255–1265.  
<https://doi.org/10.1242/jcs.01698>
- Goley, E. D., & Welch, M. D. (2006). The ARP2/3 complex: An actin nucleator comes of age. *Nature Reviews Molecular Cell Biology*, 7(10), 713–726.  
<https://doi.org/10.1038/nrm2026>
- Gratz, S. J., Rubinstein, C. D., Harrison, M. M., Wildonger, J., & O’Connor-Giles, K. M. (2015). CRISPR-Cas9 Genome Editing in Drosophila. *Current Protocols in Molecular Biology*, 111(1), 1–27. <https://doi.org/10.1002/0471142727.mb3102s111>
- Gunning, P. W., Ghoshdastider, U., Whitaker, S., Popp, D., & Robinson, R. C. (2015). The evolution of compositionally and functionally distinct actin filaments. *Journal of Cell Science*, 128(11), 2009–2019. <https://doi.org/10.1242/jcs.165563>
- Guo, Z., Neilson, L. J., Zhong, H., Murray, P. S., Zanivan, S., & Zaidel-Bar, R. (2014). E-cadherin interactome complexity and robustness resolved by quantitative proteomics. *Science Signaling*, 7(354), 1–13. <https://doi.org/10.1126/scisignal.2005473>
- Gurtner, G. C., Werner, S., Barrandon, Y., & Longaker, M. T. (2008). Wound repair and regeneration. *Nature*, 453(7193), 314–321. <https://doi.org/10.1038/nature07039>
- Guruharsha, K. G., Zhai, B., Mintseris, J., Vaidya, P., Vaidya, N., Beekman, C., Wong, C., Rhee, D. Y., Cenaj, O., Mckillip, E., Shah, S., Stapleton, M., Wan, K. H., Yu, C., Parsa, B., Carlson, J. W., Chen, X., Kapadia, B., Vijayraghavan, K., ... Artavanis-tsakonas, S. (2011). Resource A Protein Complex Network of Drosophila melanogaster. *Cell*, 147(3), 690–703. <https://doi.org/10.1016/j.cell.2011.08.047>
- Hagen, S., Brachs, S., Kroczeck, C., Fürnrohr, B. G., Lang, C., & Mielenz, D. (2012). Cell Calcium The B cell receptor-induced calcium flux involves a calcium mediated positive feedback loop. *Cell Calcium*, 51(5), 411–417. <https://doi.org/10.1016/j.ceca.2012.01.004>
- Hardy, L. R. (2012). Fluorescence Recovery After Photobleaching (FRAP) with a Focus on F-actin. *Current Protocols in Neuroscience*, 61(1), 1–12.  
<https://doi.org/10.1002/0471142301.ns0217s61>
- Heuzé, M. L., Sankara Narayana, G. H. N., D’Alessandro, J., Cellerin, V., Dang, T., Williams, D. S., Van Hest, J. C. M., Marcq, P., Mège, R. M., & Ladoux, B. (2019). Myosin II isoforms play distinct roles in adherens junction biogenesis. *eLife*, 8, 1–30.  
<https://doi.org/10.7554/eLife.46599>
- Hirschhäuser, A., van Cann, M., & Bogdan, S. (2021). CK1 $\alpha$  protects WAVE from degradation to regulate cell shape and motility in the immune response. *Journal of Cell Science*, 134(23). <https://doi.org/10.1242/jcs.258891>
- Hornbruch-Freitag, C., Griemert, B., Buttgerit, D., & Renkawitz-Pohl, R. (2011). Drosophila Swiprosin-1/EFHD2 accumulates at the prefusion complex stage during Drosophila myoblast fusion. *Journal of Cell Science*, 124(19), 3266–3278.  
<https://doi.org/10.1242/jcs.083907>
- Huang, K.-P. (1989). The mechanism of protein kinase C activation. *Trends in Neurosciences*, 12(11), 425–432. [https://doi.org/10.1016/0166-2236\(89\)90091-X](https://doi.org/10.1016/0166-2236(89)90091-X)
- Huh, Y. H., Kim, S. H., Chung, K.-H., Oh, S., Kwon, M.-S., Choi, H.-W., Rhee, S., Ryu, J.-



- H., Park, Z. Y., Jun, C.-D., & Song, W. K. (2013). Swiprosin-1 modulates actin dynamics by regulating the F-actin accessibility to cofilin. *Cellular and Molecular Life Sciences*, *70*(24), 4841–4854. <https://doi.org/10.1007/s00018-013-1447-5>
- Huh, Y. H., Oh, S., Yeo, Y. R., Chae, I. H., Kim, S. H., Lee, J. S., Yun, S. J., Choi, K. Y., Ryu, J.-H., Jun, C.-D., & Song, W. K. (2015). Swiprosin-1 stimulates cancer invasion and metastasis by increasing the Rho family of GTPase signaling. *Oncotarget*, *6*(15), 13060–13071. <https://doi.org/10.18632/oncotarget.3637>
- Hunter, M. V., Lee, D. M., Harris, T. J. C., & Fernandez-Gonzalez, R. (2015). Polarized E-cadherin endocytosis directs actomyosin remodeling during embryonic wound repair. *Journal of Cell Biology*, *210*(5), 801–816. <https://doi.org/10.1083/jcb.201501076>
- Huveneers, S., & de Rooij, J. (2013). Mechanosensitive systems at the cadherin–F-actin interface. *Journal of Cell Science*, *126*(2), 403–413. <https://doi.org/10.1242/jcs.109447>
- Jacinto, A., Martinez-Arias, A., & Martin, P. (2001). Mechanisms of epithelial fusion and repair. *Nature Cell Biology*, *3*(5), E117–E123. <https://doi.org/10.1038/35074643>
- Jayo, A., & Parsons, M. (2010). Fascin: A key regulator of cytoskeletal dynamics. *International Journal of Biochemistry and Cell Biology*, *42*(10), 1614–1617. <https://doi.org/10.1016/j.biocel.2010.06.019>
- Jin, J., & Pawson, T. (2012). Modular evolution of phosphorylation-based signalling systems. *Philosophical Transactions of the Royal Society B: Biological Sciences*, *367*(1602), 2540–2555. <https://doi.org/10.1098/rstb.2012.0106>
- Jurado, C., Haserick, J. R., & Lee, J. (2005). Slipping or gripping? Fluorescent speckle microscopy in fish keratocytes reveals two different mechanisms for generating a retrograde flow of actin. *Molecular Biology of the Cell*, *16*(2), 507–518. <https://doi.org/10.1091/mbc.E04-10-0860>
- Kamalesh, K., Scher, N., Biton, T., Schejter, E. D., Shilo, B. Z., & Avinoam, O. (2021). Exocytosis by vesicle crumpling maintains apical membrane homeostasis during exocrine secretion. *Developmental Cell*, *56*(11), 1603–1616.e6. <https://doi.org/10.1016/j.devcel.2021.05.004>
- Koestler, S. A., Auinger, S., Vinzenz, M., Rottner, K., & Small, J. V. (2008). Differentially oriented populations of actin filaments generated in lamellipodia collaborate in pushing and pausing at the cell front. *Nature Cell Biology*, *10*(3), 306–313. <https://doi.org/10.1038/ncb1692>
- Kühn, S., & Geyer, M. (2014). Formins as effector proteins of rho GTPases. *Small GTPases*, *5*(JUNE), 14–16. <https://doi.org/10.4161/sgtp.29513>
- Kwon, M.-S., Park, K. R., Kim, Y.-D., Na, B.-R., Kim, H.-R., Choi, H.-J., Piragyte, I., Jeon, H., Chung, K. H., Song, W. K., Eom, S. H., & Jun, C.-D. (2013). Swiprosin-1 Is a Novel Actin Bundling Protein That Regulates Cell Spreading and Migration. *PLoS ONE*, *8*(8), e71626. <https://doi.org/10.1371/journal.pone.0071626>
- Kwon, Y. C., Baek, S. H., Lee, H., & Choe, K. M. (2010). Nonmuscle myosin II localization is regulated by JNK during Drosophila larval wound healing. *Biochemical and Biophysical Research Communications*, *393*(4), 656–661. <https://doi.org/10.1016/j.bbrc.2010.02.047>
- Laevsky, G., & Knecht, D. A. (2003). Cross-linking of actin filaments by myosin II is a major contributor to cortical integrity and cell motility in restrictive environments. *Journal of Cell Science*, *116*(18), 3761–3770. <https://doi.org/10.1242/jcs.00684>
- Lauffenburger, D. A., & Horwitz, A. F. (1996). Cell migration: A physically integrated molecular process. *Cell*, *84*(3), 359–369. [https://doi.org/10.1016/S0092-8674\(00\)81280-5](https://doi.org/10.1016/S0092-8674(00)81280-5)
- Leader, D. P., Krause, S. A., Pandit, A., Davies, S. A., & Dow, J. A. T. (2018). FlyAtlas 2: a new version of the Drosophila melanogaster expression atlas with RNA-Seq, miRNA-Seq and sex-specific data. *Nucleic Acids Research*, *46*(D1), D809–D815.

- <https://doi.org/10.1093/nar/gkx976>
- Lehne, F., & Bogdan, S. (n.d.). EFhd2/Swip-1 promotes exocytosis of glue granules in the exocrine *Drosophila* salivary gland. *Submitted*.
- Lehne, F., Pokrant, T., Parbin, S., Salinas, G., Großhans, J., Rust, K., Faix, J., & Bogdan, S. (2022). Calcium bursts allow rapid reorganization of EFhd2/Swip-1 cross-linked actin networks in epithelial wound closure. *Nature Communications*, *13*(1), 2492. <https://doi.org/10.1038/s41467-022-30167-0>
- Lesch, C., Jo, J., Wu, Y., Fish, G. S., & Galko, M. J. (2010). A targeted UAS-RNAi screen in *Drosophila* larvae identifies wound closure genes regulating distinct cellular processes. *Genetics*, *186*(3), 943–957. <https://doi.org/10.1534/genetics.110.121822>
- Letort, G., Ennomani, H., Gressin, L., Théry, M., & Blanchoin, L. (2015). Dynamic reorganization of the actin cytoskeleton. *F1000Research*, *4*(940), 940. <https://doi.org/10.12688/f1000research.6374.1>
- Lieleg, O., Claessens, M. M. A. E., & Bausch, A. R. (2010). Structure and dynamics of cross-linked actin networks. *Soft Matter*, *6*(2), 218–225. <https://doi.org/10.1039/b912163n>
- Ma, C.-I., & Brill, J. (2021). Quantitation of Secretory Granule Size in *Drosophila* Larval Salivary Glands. *BIO-PROTOCOL*, *11*(11), 1–11. <https://doi.org/10.21769/BioProtoc.4039>
- Merrifield, C. J. (2016). Actin puts the squeeze on *Drosophila* glue secretion. *Nature Cell Biology*, *18*(2), 142–144. <https://doi.org/10.1038/ncb3305>
- Mielenz, D., & Gunn-Moore, F. (2016). Physiological and pathophysiological functions of Swiprosin-1/EFhd2 in the nervous system. *Biochemical Journal*, *473*(16), 2429–2437. <https://doi.org/10.1042/BCJ20160168>
- Moreira, C. G. A., Jacinto, A., & Prag, S. (2013). *Drosophila* integrin adhesion complexes are essential for hemocyte migration in vivo. *Biology Open*, *2*(8), 795–801. <https://doi.org/10.1242/bio.20134564>
- Moreno-Layseca, P., Jääntti, N. Z., Godbole, R., Sommer, C., Jacquemet, G., Al-Akhrass, H., Conway, J. R. W., Kronqvist, P., Kallionpää, R. E., Oliveira-Ferrer, L., Cervero, P., Linder, S., Aepfelbacher, M., Zaubner, H., Rae, J., Parton, R. G., Disanza, A., Scita, G., Mayor, S., ... Ivaska, J. (2021). Cargo-specific recruitment in clathrin- and dynamin-independent endocytosis. *Nature Cell Biology*, *23*(10), 1073–1084. <https://doi.org/10.1038/s41556-021-00767-x>
- Morowski, M., Brachs, S., Mielenz, D., Nieswandt, B., & Dütting, S. (2014). The adaptor protein swiprosin-1/EFhd2 is dispensable for platelet function in mice. *PLoS ONE*, *9*(9). <https://doi.org/10.1371/journal.pone.0107139>
- Munjal, A., Philippe, J.-M., Munro, E., & Lecuit, T. (2015). A self-organized biomechanical network drives shape changes during tissue morphogenesis. *Nature*, *524*(7565), 351–355. <https://doi.org/10.1038/nature14603>
- Nakamura, M., Dominguez, A. N. M., Decker, J. R., Hull, A. J., Verboon, J. M., & Parkhurst, S. M. (2018). Into the breach: How cells cope with wounds. *Open Biology*, *8*(10). <https://doi.org/10.1098/rsob.180135>
- Nakamura, M., Verboon, J. M., & Parkhurst, S. M. (2017). Prepatterning by RhoGEFs governs Rho GTPase spatiotemporal dynamics during wound repair. *Journal of Cell Biology*, *216*(12), 3959–3969. <https://doi.org/10.1083/jcb.201704145>
- Nakayama, S., & Kretsinger, R. H. (1994). Evolution of the EF-Hand Family of Proteins. *Annual Review of Biophysics and Biomolecular Structure*, *23*(1), 473–507. <https://doi.org/10.1146/annurev.bb.23.060194.002353>
- Park, K. R., An, J. Y., Kang, J. Y., Lee, J.-G., Lee, Y., Mun, S. A., Jun, C., Song, W. K., & Eom, S. H. (2017). Structural mechanism underlying regulation of human EFhd2/Swiprosin-1 actin-bundling activity by Ser183 phosphorylation. *Biochemical and Biophysical Research Communications*, *483*(1), 442–448.

- <https://doi.org/10.1016/j.bbrc.2016.12.124>
- Park, K. R., Kwon, M.-S., An, J. Y., Lee, J.-G., Youn, H.-S., Lee, Y., Kang, J. Y., Kim, T. G., Lim, J. J., Park, J. S., Lee, S. H., Song, W. K., Cheong, H.-K., Jun, C.-D., & Eom, S. H. (2016). Structural implications of Ca<sup>2+</sup>-dependent actin-bundling function of human EFhd2/Swiprosin-1. *Scientific Reports*, 6(1), 39095. <https://doi.org/10.1038/srep39095>
- Park, S. H., Lee, C. wool, Lee, J. H., Park, J. Y., Roshandell, M., Brennan, C. A., & Choea, K. M. (2018). Requirement for and polarized localization of integrin proteins during Drosophila wound closure. *Molecular Biology of the Cell*, 29(18), 2137–2147. <https://doi.org/10.1091/mbc.E17-11-0635>
- Parsons, B., & Foley, E. (2016). Cellular immune defenses of Drosophila melanogaster. *Developmental & Comparative Immunology*, 58, 95–101. <https://doi.org/10.1016/j.dci.2015.12.019>
- Peskin, C. S., Odell, G. M., & Oster, G. F. (1993). Cellular motions and thermal fluctuations: the Brownian ratchet. *Biophysical Journal*, 65(1), 316–324. [https://doi.org/10.1016/S0006-3495\(93\)81035-X](https://doi.org/10.1016/S0006-3495(93)81035-X)
- Pilo Boyl, P., & Witke, W. (2014). Small, smaller... dendritic spine. *The EMBO Journal*, 33(23), 2737–2739. <https://doi.org/10.15252/embj.201490137>
- Pollard, T. D. (2007). Regulation of actin filament assembly by Arp2/3 complex and formins. *Annual Review of Biophysics and Biomolecular Structure*, 36, 451–477. <https://doi.org/10.1146/annurev.biophys.35.040405.101936>
- Pollard, T. D. (2016). Actin and actin-binding proteins. *Cold Spring Harbor Perspectives in Biology*, 8(8), 1–17. <https://doi.org/10.1101/cshperspect.a018226>
- Pollard, T. D., & Borisy, G. G. (2003). Cellular Motility Driven by Assembly and Disassembly of Actin Filaments. *Cell*, 112(4), 453–465. [https://doi.org/10.1016/S0092-8674\(03\)00120-X](https://doi.org/10.1016/S0092-8674(03)00120-X)
- Ramesh, T. P., Kim, Y.-D., Kwon, M.-S., Jun, C.-D., & Kim, S.-W. (2009). Swiprosin-1 Regulates Cytokine Expression of Human Mast Cell Line HMC-1 through Actin Remodeling. *Immune Network*, 9(6), 274. <https://doi.org/10.4110/in.2009.9.6.274>
- Razzell, W., Evans, I. R., Martin, P., & Wood, W. (2013). Calcium Flashes Orchestrate the Wound Inflammatory Response through DUOX Activation and Hydrogen Peroxide Release. *Current Biology*, 23(5), 424–429. <https://doi.org/10.1016/j.cub.2013.01.058>
- Razzell, W., Wood, W., & Martin, P. (2011). Swatting flies: Modelling wound healing and inflammation in Drosophila. *DMM Disease Models and Mechanisms*, 4(5), 569–574. <https://doi.org/10.1242/dmm.006825>
- Ridley, A. J., Schwartz, M. A., Burridge, K., Firtel, R. A., Ginsberg, M. H., Borisy, G., Parsons, J. T., & Horwitz, A. R. (2003). Cell Migration: Integrating Signals from Front to Back. *Science*, 302(5651), 1704–1709. <https://doi.org/10.1126/science.1092053>
- Rouiller, I., Xu, X. P., Amann, K. J., Egile, C., Nickell, S., Nicastro, D., Li, R., Pollard, T. D., Volkman, N., & Hanein, D. (2008). The structural basis of actin filament branching by the Arp2/3 complex. *Journal of Cell Biology*, 180(5), 887–895. <https://doi.org/10.1083/jcb.200709092>
- Rouso, T., Schejter, E. D., & Shilo, B. Z. (2016). Orchestrated content release from Drosophila glue-protein vesicles by a contractile actomyosin network. *Nature Cell Biology*, 18(2), 181–190. <https://doi.org/10.1038/ncb3288>
- Rüder, M., Nagel, B. M., & Bogdan, S. (2018). Analysis of Cell Shape and Cell Migration of Drosophila Macrophages In Vivo. *Methods in Molecular Biology*, 1749, 227–238. [https://doi.org/https://doi.org/10.1007/978-1-4939-7701-7\\_17](https://doi.org/https://doi.org/10.1007/978-1-4939-7701-7_17)
- Ryan, G. L., Holz, D., Yamashiro, S., Taniguchi, D., Watanabe, N., & Vavylonis, D. (2017). Cell protrusion and retraction driven by fluctuations in actin polymerization: A two-dimensional model. *Cytoskeleton*, 74(12), 490–503. <https://doi.org/10.1002/cm.21389>
- Schwayer, C., Sikora, M., Slovák, J., Kardos, R., & Heisenberg, C.-P. (2016). Actin Rings

- of Power. *Developmental Cell*, 37(6), 493–506.  
<https://doi.org/10.1016/j.devcel.2016.05.024>
- Segal, D., Zaritsky, A., Schejter, E. D., & Shilo, B. Z. (2018). Feedback inhibition of actin on Rho mediates content release from large secretory vesicles. *Journal of Cell Biology*, 217(5), 1815–1826. <https://doi.org/10.1083/jcb.201711006>
- Sept, D., & McCammon, J. A. (2001). Thermodynamics and kinetics of actin filament nucleation. *Biophysical Journal*, 81(2), 667–674. [https://doi.org/10.1016/S0006-3495\(01\)75731-1](https://doi.org/10.1016/S0006-3495(01)75731-1)
- Shieh, B.-H., Parker, L., & Popescu, D. (2002). Protein Kinase C (PKC) Isoforms in Drosophila. *Journal of Biochemistry*, 132(4), 523–527.  
<https://doi.org/10.1093/oxfordjournals.jbchem.a003252>
- Sjöblom, B., Salmazo, A., & Djinović-Carugo, K. (2008).  $\alpha$ -Actinin structure and regulation. *Cellular and Molecular Life Sciences*, 65(17), 2688–2701.  
<https://doi.org/10.1007/s00018-008-8080-8>
- Small, J. V., Rottner, K., Kaverina, I., & Anderson, K. I. (1998). Assembling an actin cytoskeleton for cell attachment and movement. *Biochimica et Biophysica Acta (BBA) - Molecular Cell Research*, 1404(3), 271–281. [https://doi.org/10.1016/S0167-4889\(98\)00080-9](https://doi.org/10.1016/S0167-4889(98)00080-9)
- Small, J. V., Stradal, T., Vignat, E., & Rottner, K. (2002). The lamellipodium: where motility begins. *Trends in Cell Biology*, 12(3), 112–120. [https://doi.org/10.1016/S0962-8924\(01\)02237-1](https://doi.org/10.1016/S0962-8924(01)02237-1)
- Soliman, A. S., Umstead, A., Grabinski, T., Kanaan, N. M., Lee, A., Ryan, J., Lamp, J., & Vega, I. E. (2021). EFhd2 brain interactome reveals its association with different cellular and molecular processes. *Journal of Neurochemistry*, 159(6), 992–1007.  
<https://doi.org/10.1111/jnc.15517>
- Sun, H. Q., Yamamoto, M., Mejillano, M., & Yin, H. L. (1999). Gelsolin, a Multifunctional Actin Regulatory Protein. *Journal of Biological Chemistry*, 274(47), 33179–33182.  
<https://doi.org/10.1074/jbc.274.47.33179>
- Sun, Z., Guo, S. S., & Fässler, R. (2016). Integrin-mediated mechanotransduction. *Journal of Cell Biology*, 215(4), 445–456. <https://doi.org/10.1083/jcb.201609037>
- Svitkina, T. (2018). The actin cytoskeleton and actin-based motility. *Cold Spring Harbor Perspectives in Biology*, 10(1), 1–21. <https://doi.org/10.1101/cshperspect.a018267>
- Sweeney, H. L., & Hammers, D. W. (2018). Muscle contraction. *Cold Spring Harbor Perspectives in Biology*, 10:a030288. <https://doi.org/doi:10.1101/cshperspect.a023200>
- Takeichi, M. (2014). Dynamic contacts: rearranging adherens junctions to drive epithelial remodelling. *Nature Reviews Molecular Cell Biology*, 15(6), 397–410.  
<https://doi.org/10.1038/nrm3802>
- Thylur, R. P., Gowda, R., Mishra, S., & Jun, C.-D. (2018). Swiprosin-1: Its Expression and Diverse Biological Functions. *Journal of Cellular Biochemistry*, 119(1), 150–156.  
<https://doi.org/10.1002/jcb.26199>
- Totsukawa, G., Wu, Y., Sasaki, Y., Hartshorne, D. J., Yamakita, Y., Yamashiro, S., & Matsumura, F. (2004). Distinct roles of MLCK and ROCK in the regulation of membrane protrusions and focal adhesion dynamics during cell migration of fibroblasts. *Journal of Cell Biology*, 164(3), 427–439. <https://doi.org/10.1083/jcb.200306172>
- Tran, D. T., Masedunskas, A., Weigert, R., & Ten Hagen, K. G. (2015). Arp2/3-mediated F-actin formation controls regulated exocytosis in vivo. *Nature Communications*, 6.  
<https://doi.org/10.1038/ncomms10098>
- Tran, D. T., & Ten Hagen, K. G. (2017). Real-time insights into regulated exocytosis. *Journal of Cell Science*, 130(8), 1355–1363. <https://doi.org/10.1242/jcs.193425>
- Tsai, F.-C., Kuo, G.-H., Chang, S.-W., & Tsai, P.-J. (2015). Ca<sup>2+</sup> Signaling in Cytoskeletal Reorganization, Cell Migration, and Cancer Metastasis. *BioMed Research International*,

- 2015, 1–13. <https://doi.org/10.1155/2015/409245>
- Tseng, Y., Schafer, B. W., Almo, S. C., & Wirtz, D. (2002). Functional synergy of actin filament cross-linking proteins. *Journal of Biological Chemistry*, 277(28), 25609–25616. <https://doi.org/10.1074/jbc.M202609200>
- Tu, Y., Zhang, L., Tong, L., Wang, Y., Zhang, S., Wang, R., Li, L., & Wang, Z. (2018). EFhd2 / swiprosin-1 regulates LPS-induced macrophage recruitment via enhancing actin polymerization and cell migration. *International Immunopharmacology*, 55(September 2017), 263–271. <https://doi.org/10.1016/j.intimp.2017.12.030>
- Urban, E., Jacob, S., Nemethova, M., Resch, G. P., & Small, J. V. (2010). Electron tomography reveals unbranched networks of actin filaments in lamellipodia. *Nature Cell Biology*, 12(5), 429–435. <https://doi.org/10.1038/ncb2044>
- Van Audenhove, I., Denert, M., Boucherie, C., Pieters, L., Cornelissen, M., & Gettemans, J. (2016). Fascin rigidity and L-plastin flexibility cooperate in cancer cell invadopodia and FilopodiaS. *Journal of Biological Chemistry*, 291(17), 9148–9160. <https://doi.org/10.1074/jbc.M115.706937>
- Vázquez-Rosa, E., Rodríguez-Cruz, E. N., Serrano, S., Rodríguez-Laureano, L., & Vega, I. E. (2014). Cdk5 phosphorylation of EFhd2 at S74 affects its calcium binding activity. *Protein Science*, 23(9), 1197–1207. <https://doi.org/10.1002/pro.2499>
- Vega, I. E., Traverso, E. E., Ferrer-Acosta, Y., Matos, E., Colon, M., Gonzalez, J., Dickson, D., Hutton, M., Lewis, J., & Yen, S. H. (2008). A novel calcium-binding protein is associated with tau proteins in tauopathy. *Journal of Neurochemistry*, 106(1), 96–106. <https://doi.org/10.1111/j.1471-4159.2008.05339.x>
- Vicente-Manzanares, M., Ma, X., Adelstein, R. S., & Horwitz, A. R. (2009). Non-muscle myosin II takes centre stage in cell adhesion and migration. *Nature Reviews Molecular Cell Biology*, 10(11), 778–790. <https://doi.org/10.1038/nrm2786>
- Vicente-Manzanares, M., Zareno, J., Whitmore, L., Choi, C. K., & Horwitz, A. F. (2007). Regulation of protrusion, adhesion dynamics, and polarity by myosins IIA and IIB in migrating cells. *Journal of Cell Biology*, 176(5), 573–580. <https://doi.org/10.1083/jcb.200612043>
- Vinzenz, M., Nemethova, M., Schur, F., Mueller, J., Narita, A., Urban, E., Winkler, C., Schmeiser, C., Koestler, S. A., Rottner, K., Resch, G. P., Maeda, Y., & Small, J. V. (2012). Actin branching in the initiation and maintenance of lamellipodia. *Journal of Cell Science*, 125(11), 2775–2785. <https://doi.org/10.1242/jcs.107623>
- Vuadens, F., Rufer, N., Kress, A., Corthésy, P., Schneider, P., & Tissot, J. (2004). Identification of swiprosin 1 in human lymphocytes. *PROTEOMICS*, 4(8), 2216–2220. <https://doi.org/10.1002/pmic.200300779>
- Waterhouse, A. M., Procter, J. B., Martin, D. M. A., Clamp, M., & Barton, G. J. (2009). Jalview Version 2--a multiple sequence alignment editor and analysis workbench. *Bioinformatics*, 25(9), 1189–1191. <https://doi.org/10.1093/bioinformatics/btp033>
- Wei, C., Wang, X., Chen, M., Ouyang, K., Song, L. S., & Cheng, H. (2009). Calcium flickers steer cell migration. *Nature*, 457(7231), 901–905. <https://doi.org/10.1038/nature07577>
- Welch, M. D., DePace, A. H., Verma, S., Iwamatsu, A., & Mitchison, T. J. (1997). The Human Arp2/3 Complex Is Composed of Evolutionarily Conserved Subunits and Is Localized to Cellular Regions of Dynamic Actin Filament Assembly. *Journal of Cell Biology*, 138(2), 375–384. <https://doi.org/10.1083/jcb.138.2.375>
- Wickstead, B., & Gull, K. (2011). The evolution of the cytoskeleton. *Journal of Cell Biology*, 194(4), 513–525. <https://doi.org/10.1083/jcb.201102065>
- Wolgemuth, C. W. (2005). Lamellipodial contractions during crawling and spreading. *Biophysical Journal*, 89(3), 1643–1649. <https://doi.org/10.1529/biophysj.105.066720>
- Wood, W., Jacinto, A., Grose, R., Woolner, S., Gale, J., Wilson, C., & Martin, P. (2002). Wound healing recapitulates morphogenesis in Drosophila embryos. *Nature Cell*

- Biology*, 4(11), 1–7. <https://doi.org/10.1038/ncb875>
- Wu, Y., Brock, A. R., Wang, Y., Fujitani, K., Ueda, R., & Galenko, M. J. (2009). A Blood-Borne PDGF/VEGF-like Ligand Initiates Wound-Induced Epidermal Cell Migration in *Drosophila* Larvae. *Current Biology*, 19(17), 1473–1477. <https://doi.org/10.1016/j.cub.2009.07.019>
- Yamashiro, S., Yamakita, Y., Ono, S., & Matsumura, F. (1998). Fascin, an actin-bundling protein, induces membrane protrusions and increases cell motility of epithelial cells. *Molecular Biology of the Cell*, 9(5), 993–1006. <https://doi.org/10.1091/mbc.9.5.993>
- Ydenberg, C. A., Smith, B. A., Breitsprecher, D., Gelles, J., & Goode, B. L. (2011). Cease-fire at the leading edge: New perspectives on actin filament branching, debranching, and cross-linking. *Cytoskeleton*, 68(11), 596–602. <https://doi.org/10.1002/cm.20543>
- Zanet, J., Stramer, B., Millard, T., Martin, P., Payre, F., & Plaza, S. (2009). Fascin is required for blood cell migration during *Drosophila* embryogenesis. *Development*, 136(15), 2557–2565. <https://doi.org/10.1242/dev.036517>
- Zhang, S., Tu, Y., Sun, Y., Li, Y., Wang, R., Cao, Y., Li, L., Zhang, L., & Wang, Z.-B. (2018). Swiprosin-1 deficiency impairs macrophage immune response of septic mice. *JCI Insight*, 3(3). <https://doi.org/10.1172/jci.insight.95396>

## 8 Appendix

### 8.1 Author Contributions

Publication 1:

Lehne, F., Pokrant, T., Parbin, S., Salinas, G., Großhans, J., Rust, K., Faix, J., & Bogdan, S. (2022). Calcium bursts allow rapid reorganization of EFhD2/Swip-1 cross-linked actin networks in epithelial wound closure. *Nature Communications*, *13*(1), 2492.

Figure 1: I performed all experiments and quantification.  
 Figure 2: I performed all experiments and quantifications.  
 Figure 4: I established the wound closure protocol and performed all experiments.  
 Figure 5: I performed all experiments and quantifications.  
 Figure S2: I performed all experiments and quantifications.  
 Movies S1-3, 10-13: I performed all experiments.  
 Sven Bogdan and Jan Faix wrote the manuscript and I commented on it.

Publication 2:

Lehne, F., & Bogdan, S. EFhD2/Swip-1 promotes exocytosis of glue granules in the exocrine *Drosophila* salivary gland. *Submitted*.

Figure 1: I performed all experiments.  
 Figure 2: I performed all experiments and quantifications.  
 Figure 3: I designed the experiment in (A,B). I performed all experiments and quantifications.  
 Figure 4: I performed the experiment in (A,B).  
 Movies S1-3: I performed all experiments.  
 Sven Bogdan wrote the manuscript and I commented on it.

Hiermit bestätige ich die Richtigkeit der Angaben bezüglich der Eigenanteile von Frau Franziska Lehne an den oben aufgeführten Publikationen.

Marburg, den

---

Sven Bogdan

---

Franziska Lehne

## 8.2 *Drosophila* transgenic lines used in this work

Genotype	Description	Reference/ Stock Number
P{KK102466}VIE-260B	Swip-1 RNAi	v107033
w1118; P{GD7047}v31308	Swip-1 RNAi	v31308
w1118; P{GD7047}v31307	Swip-1 RNAi	v31307
y1 v1; P{TRiP.JF01160}attP2	Swip-1 RNAi	BL31585
2XTY1-SGFP-V5-preTEV-BLRP-3XFLAG PBac{fTRG01300.sfGFP-TVPTBF}VK00033	FlyFos, no GFP expression detectable	v318835
y <sup>1</sup> , w* ; Swip-1 <sup>TrojanMiMIC</sup> /SM6a	GFP knock in, no fluorescence detectable	BL44795
y <sup>1</sup> , w <sup>67c23</sup> ; Swip-1 <sup>EY08031</sup>	for P-element mobilization; no mutant could be generated	BL20014
; YB0230PE FlyTrap ;;	no GFP expression detectable	S. Önel
y[1] w[*]; Mi{Trojan-GAL4.2}Swip-1[MI08585- TG4.2]/SM6a	Gal4 knock in <i>swip-1</i> ; mutant homozygous not viable	BL76699
w[1118]; Df(2L)ED1202, P{w[+mW.Scer\FRT.hs3]=3'.RS5+3.3'}ED1202 / SM6a	deficiency 37B1 – 37C5	Kyoto 150-315
srp-Gal4	hemocyte-unspecific, used for salivary glands	D. Siekhaus
w[-] ; e22c-Gal4/CyO ;;	used for wound closure	M. Leptin
w[-] ;; A58-Gal4/TM6B	used for wound closure	M. Leptin
y[1] M{vas-int.Dm}ZH2A w[*]; M{3xP3- RFP.attP'}ZH-51C	injection 2. chromosome (strong)	BL24482
y[1] M{vas-int.Dm}ZH2A w[*]; M{3xP3- RFP.attP'}ZH-68E	injection 3. chromosome (weak)	BL24485
y[1] M{vas-int.Dm}ZH2A w[*]; M{3xP3- RFP.attP'}ZH-86Fb	injection 3. chromosome (strong)	BL24749
Bl/CyO ; UASP-Swip	injection in 86Fb	
Bl/CyO ; UASP-Swip-eGFP	injection in 86Fb	



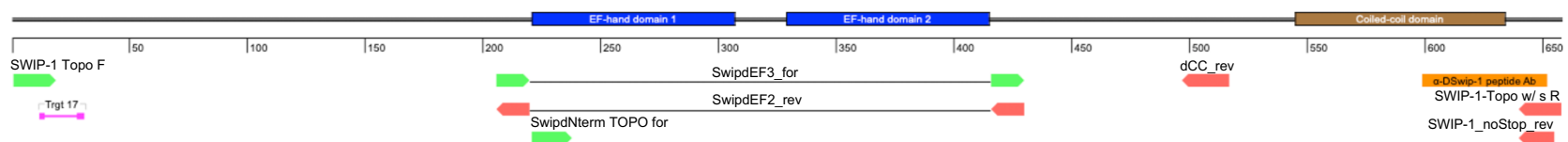
Bl/CyO ; UASP-eGFP-Swip	injection in 86Fb	
Bl/CyO ; UAST-Swip	injection in 86Fb	
Bl/CyO ; UAST-Swip-eGFP/TM6B	injection in 86Fb	
Bl/CyO ; UAST-Swip-mScarlet-H/TM6B	injection in 86Fb	
Bl/CyO ; UAST-Swip-mScarlet-I	injection in 86Fb	
Bl/CyO ; UAST-eGFP-Swip $\Delta$ EF/TM6B	injection in 68E	
Bl/CyO ; UAST-Swip $\Delta$ CC-eGFP/TM6B	injection in 68E	
Bl/CyO ; UAST-SwipD82A/D118A-eGFP/TM6B	injection in 68E	
Swip-Gal4 ; TM2/TM6B	injection in 51C	
Bl/CyO ; Swip-Gal4/TM6B	injection in 68E	
Bl/CyO ; CRISPR Swip Trgt17	injection in 86Fb	
<i>swip</i> <sup><math>\Delta</math>1</sup> ; TM2/TM6B	CRISPR/Cas9 mutant	
	ATGTCCA-----CGACGCC	
<i>swip</i> <sup><math>\Delta</math>2</sup> ; TM2/TM6B	CRISPR/Cas9 mutant	
	ATGTCCGTT-----CAACGCC	
w[*]; PBac{w[+mC]=20XUAS-IVS-NES-jRCaMP1a-p10}VK00005	RCaMP1a	BL63792
w[*]; PBac{w[+mC]=20XUAS-IVS-NES-jRCaMP1b-p10}VK00005	RCaMP1b	BL63793
P{w[+mC]=UAS-LifeAct.GFP.W}3	Lifeact-GFP	BL57326
P{y[+t*] w[+mC]=UAS-LifeAct-Ruby}VIE-19A	Lifeact-Ruby	BL35545
w[*]; M{w[+mC]=UASp-Lifeact.TagRFP.H}ZH-51D/CyO	Lifeact-tagRFP	BL58715
w[*]; P{w[+m*]=Sgs3-GFP}2	salivary glands glue protein	BL5884
P{w[+mC]=Sgs3-GFP}3	salivary glands glue protein	BL5885
w;;UAS-serp-CBD-GFP	salivary glands glue protein	M. Brankatschk
w[*]; P{w[+mC]=PTT-GC}zip[CC01626]/SM6a	endogenous GFP-tag	BL51564
w[1118]; P{w[+mC]=sqh-GFP.RLC}3	endogenous GFP-tag	BL57145

w[*]; P{w[+mC]=sqh-mCherry.M}3	endogenous mCherry-tag	BL59024
Dia-GFP/CyO ; Dr/TM6B	endogenous GFP-tag	J. Großhans
Bl/CyO ; hmlGal4, UASP-Lifeact-GFP/TM6B	recombination, macrophages	
swip <sup>Δ1</sup> , hmlGal4 ; TM2/TM6B	recombination, macrophages	
Bl/CyO ; hmlGal4, UAST-Swip-1-mScarlet-I/TM6B	recombination, macrophages	
ptcGal4, UAS-Lifeact-GFP/CyO ; TM2/TM6B	recombination, salivary glands	
ptcGal4, UAS-Lifeact-Ruby/CyO ; TM2/TM6B	recombination, salivary glands	
Bl/CyO ; srpGal4, UAS-Lifeact-GFP/TM6B	recombination, salivary glands	
Bl/CyO ; srpGal4, UAST-Swip-1-eGFP	recombination, salivary glands	
Bl/CyO ; srpGal4, UAST-eGFP-Swip-1	recombination, salivary glands	
Bl/CyO ; srpGal4, UAST-eGFP-Swip-1-ΔEF/TM6B	recombination, salivary glands	
Bl/CyO ; srpGal4, UASP-Swip-1-ΔCC-eGFP/TM6B	recombination, salivary glands	
Bl/CyO ; srpGal4, UAST-Swip-1-ΔCC-eGFP/TM6B	recombination, salivary glands	
Bl/CyO ; srpGal4, UAST-Swip-1-D82A/D118A-eGFP/TM6B	recombination, salivary glands	
Bl/CyO ; srpGal4, UASP-eGFP-Swip-1, UAS-myr-mRFP/TM6B	recombination, salivary glands	
<i>swip</i> <sup>Δ1</sup> , UASP-Lifeact-Ruby ; TM2/TM6B	recombination, salivary glands	
Bl/CyO ; srpGal4, UAS-myr-mRFP/TM6B	recombination, salivary glands	
Bl/CyO ; srpGal4, UAS-Sgs3-GFP/TM6B	recombination, salivary glands	
Bl/CyO ; srpGal4, UAS-serpCBD-GFP/TM6B	recombination, salivary glands	
ptcGal4, UAST-Arp3-eGFP/CyO ; TM2/TM6B	recombination, salivary glands	
Bl/CyO ; srpGal4, UASP-GFP-Arp3/TM6B	recombination, salivary glands	
Bl/CyO ; srpGal4, WASP-mCherry/TM6B	recombination, salivary glands	
Bl/CyO ; daGal4, UASP-Lifeact-GFP/TM6B	recombination, wound closure	
Bl/CyO ; A58Gal4, UASP-Lifeact-GFP/TM6B	recombination, wound closure	
Bl/CyO ; pnrGal4, UASP-Lifeact-GFP/TM6B	recombination, wound closure	
Bl/CyO ; daGal4, UASP-Swip-eGFP/TM6B	recombination, wound closure	

Bl/CyO ; daGal4, UAST-Swip-eGFP/TM6B	recombination, wound closure
Bl/CyO ; daGal4, UAST-eGFP-Swip/TM6B	recombination, wound closure
Bl/CyO ; daGal4, UAST-eGFP-Swip $\Delta$ EF/TM6B	recombination, wound closure
Bl/CyO ; daGal4, UASP-Swip $\Delta$ CC-eGFP/TM6B	recombination, wound closure
Bl/CyO ; daGal4, UAST-Swip $\Delta$ CC-eGFP/TM6B	recombination, wound closure
Bl/CyO ; daGal4, UAST-SwipD82A/D118A-eGFP/TM6B	recombination, wound closure
<i>swip</i> <sup><math>\Delta</math>1</sup> , UASP-Lifeact-tagRFP ; daGal4/TM6B	recombination, wound closure

## 8.3 Plasmids generated in this work

Swip-1  
(overview)



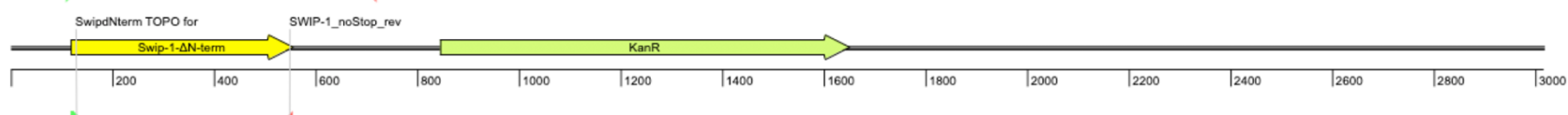
pENTR-Swip-1\_nS



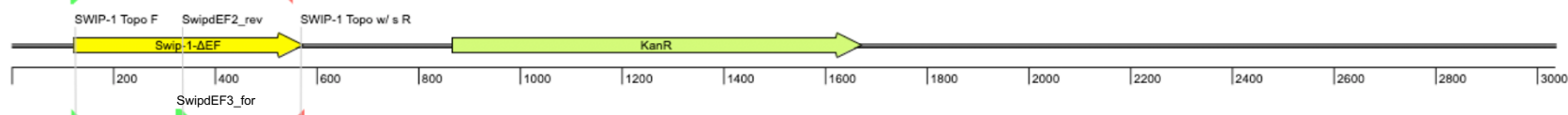
pENTR-Swip-1



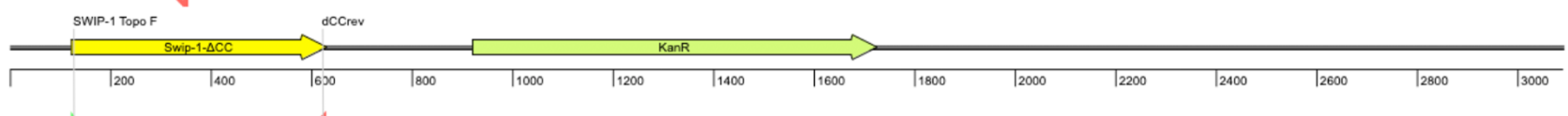
pENTR-Swip-1- $\Delta$ N-term



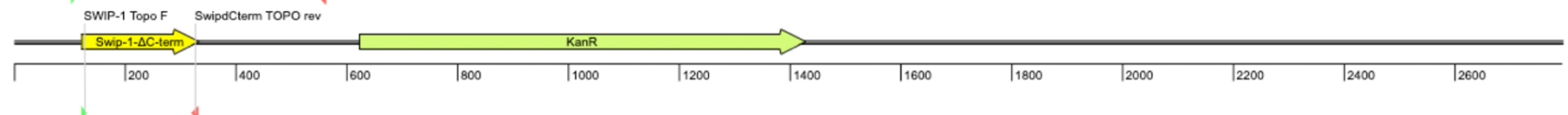
pENTR-Swip-1- $\Delta$ EF



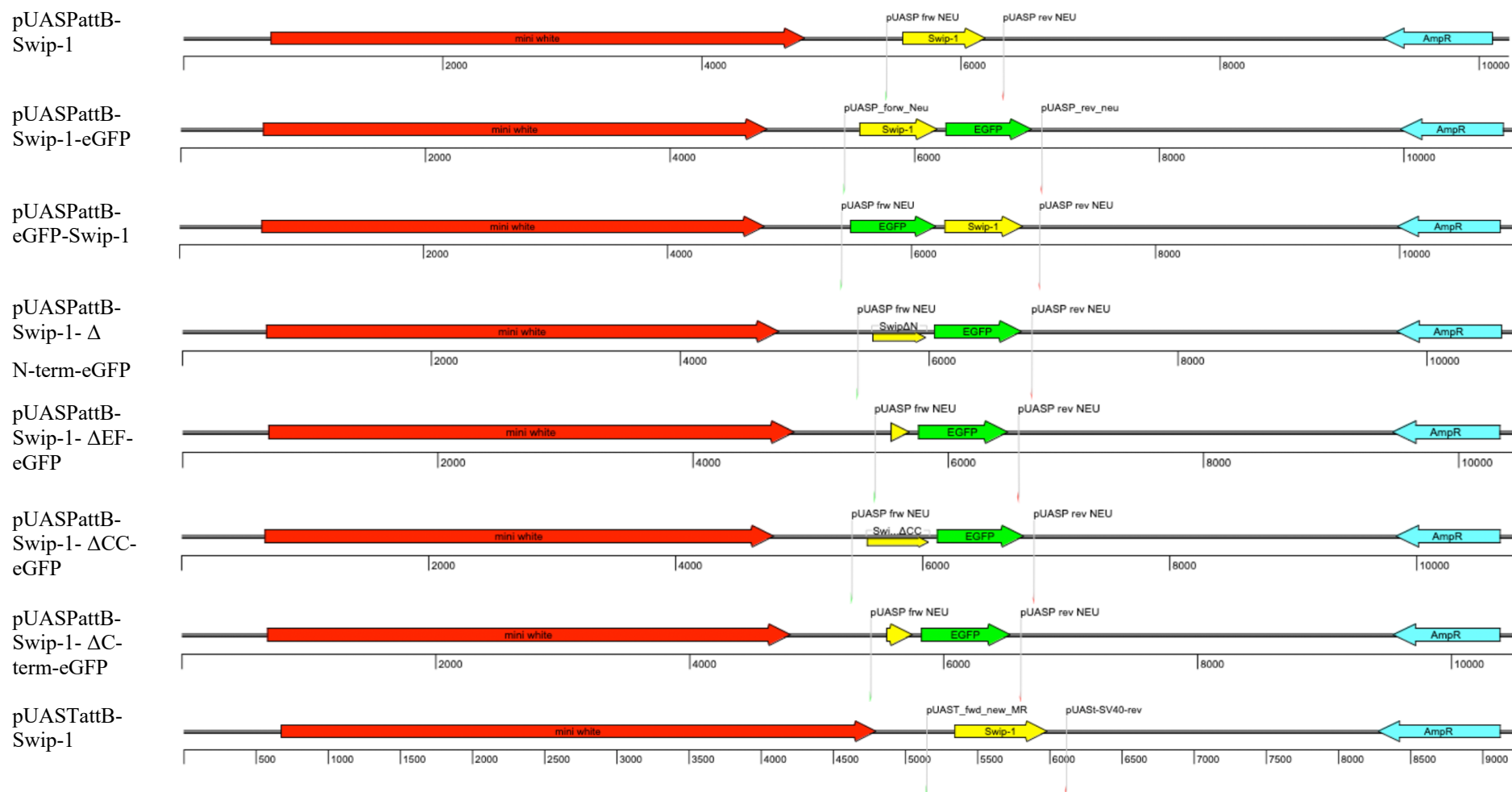
pENTR-Swip-1- $\Delta$ CC



pENTR-Swip-1- $\Delta$ C-term

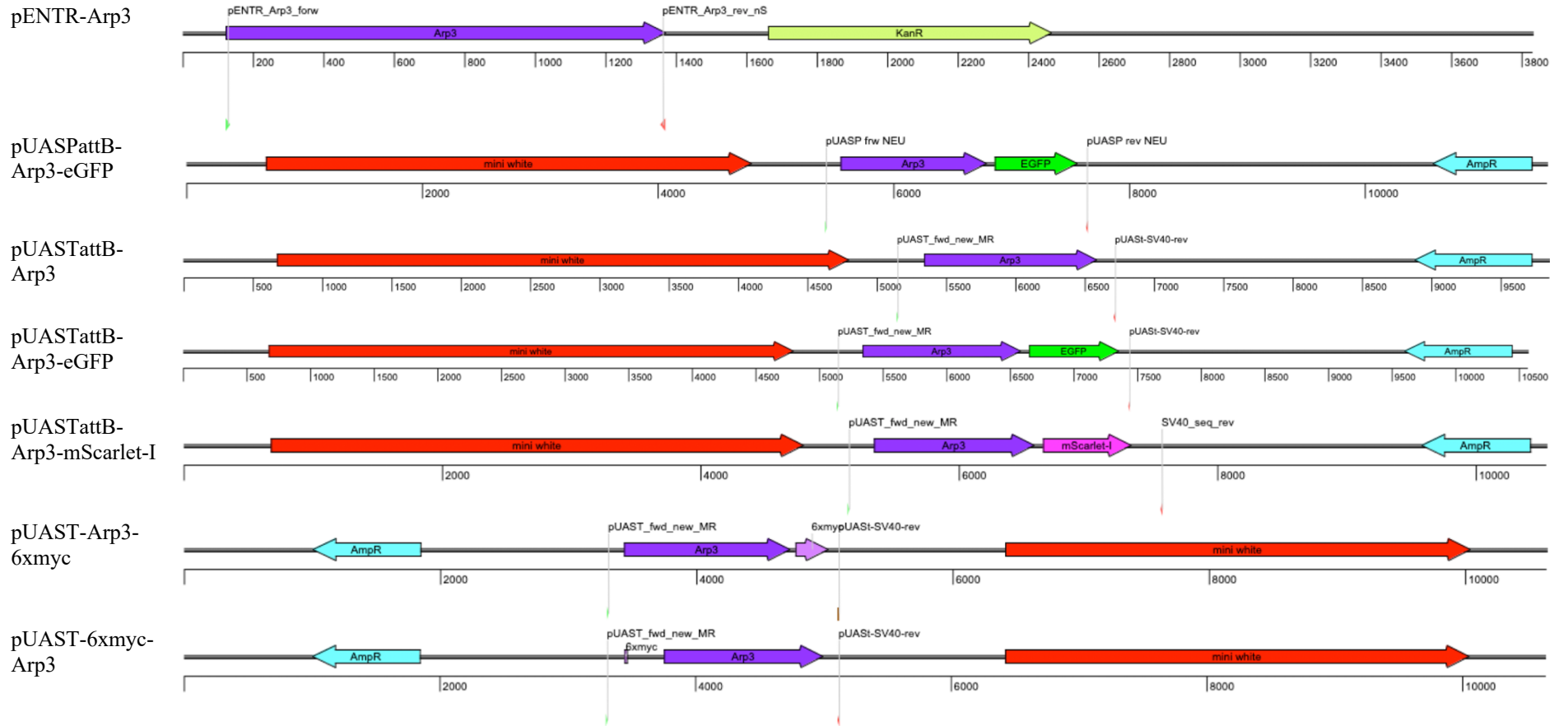


pENTR-Swip-1-D82A/D118A Site directed mutagenesis of pENTR-Swip-1, see list of primers. Subsequent Gateway cloning of pUAST-Swip-1-D82A/D118A-cGFP.











## 8.4 List of PCR primers

SWIP-1 Topo F	CACCATGTCCGTTTCCTCG
SWIP-1_noStop_rev	CTGGAAGATCGCTGCCCCG
SWIP-1 Topo w/ s R	CTACTGGAAGATCGCTGCC
SwipdNterm TOPO for	CACCATGGACTACCAGAAGACCTTC
dCCrev	GAAGAAGTTCTTGGCTCCGCT
SwipdCterm TOPO rev	CTTGATCTGGTTACGGGA
SwipdEF3_for	CGTAACCAGATCAAGCAGGCCGGGGAAGCTG
SwipdEF2_rev	CAGTTCCCCGGCCTGCTTGATCTGGTTACG
pENTR-SwipD82A_for	CAATACATACGCCACGGCTCGTG
pENTR-SwipD82A_rev	AAGGTCTTCTGGTAGTCC
pENTR-SwipD118A_for	TGCCGAGGTGGCCGAGGATAACG
pENTR-SwipD118A_rev	ATCATCTGCTTGAGTCCCAGATG
Swip_BamHI_for	TTAGGATCCCATGTCCGTTTCCT
Swip_NotI_rev	ATTGCGGCCGCCTACTGGAAGATCGCT
SwipdCC_XhoI_rev	TTACTCGAGCTAGAAGAAGTTCTTGG
EFhd2hum_BamHI_for	ATTTGGATTCATGGCCACGGAC
EFhd2hum_XhoI_rev	ATTTCTCGAGCTACTTAAAGGTGG
SwipProm1_for	CACCTTTCATTCGTCTCTCAGCG
SwipProm1,B_rev	TGTGTCGCTCCTTGTTGACTCG
SWIP-1_Trgt17-sense	AAACTTTCCTCGAACGCCTCATC
SWIP-1_Trgt17-antisense	GTCGGATGAGGCGTTCGAGGAAA
pENTR_Arp3_forw	CACCATGGCAGGCAGGCTACCGG
pENTR_Arp3_rev_nS	TGTCATGGTGCCAAAGACG
pENTR_Arp3_rev_Stopp	TTATGTCATGGTGCCAAAGACGG
pBPGUw_Seq_for	AAATAGGGGTTCCGCGCACAT

pBPGUw_Seq_rev	ATAATGGTGCAGGGCGCTGAC
pUASP frw NEU	CCTGTTCAATTGGTACCCG
pUASP rev NEU	CTCTTGACCATGGGTTTAGG
pUAST_fwd_new_MR	TCAATTAAAAGTAACCAGCAACCAA
pUAST-SV40-rev	TAGAGCTTTAAATCTCTGTAGG

## 8.5 Verzeichnis der akademischen Lehrer und Lehrerinnen

Meine akademischen Lehrenden in Braunschweig waren die Damen und Herren:

Bauerecker, Bergmann, Bittner, Böldicke, Brown, Buchberger-Seidl, Dickschat, Drexler, Dübel, Frenzel, Hänsch, Holz, Hust, Ibrom, Jahn, Jänsch, Jones, Jördening, Kampen, Käufer, Korte, Köster, Krull, Kruse, Kwade, Layer, Mazik, Mendel, Noth, Pérez Crespo, Prusov, Rau, Rothkegel, Rottner, Schirrmann, Schmidt, Schmidt-Hohagen, Schnabel, Scholl, Schomburg, Schumpe, Steinert, Süllo, Tinnfeld, Vauti, Walla, Weiß, Winter, Wittmann und Ziehr.

Meine akademischen Lehrenden waren in Río Piedras, San Juan die Dame und die Herren:

Ackerman, Castro Gomez, Emmanuelli Huertas, García Arrarás, Massey

## 8.6 Danksagung

Es weiß wohl jeder, dass ich kein Mensch der langen Reden bin, deswegen halte ich mich auch hier kurz.

Ich möchte mich zu aller erst bei Sven bedanken. Ein großes Dankeschön für die Möglichkeit in deiner Forschungsgruppe zu arbeiten und meine Doktorarbeit zu verfassen. Danke auch für das stetige Vertrauen in meine Arbeit und die große Unterstützung bei der Verfassung dieser Dissertation sowie der Manuskripte.

Danke auch an alle Mitarbeiter\*innen der AG Bogdan, die mich auf dem Weg zur Promotion begleitet haben. Ohne euch hätte es nur halb so viel Spaß gemacht! Damit ich niemanden vergesse, fange ich erst gar nicht an, euch alle namentlich zu nennen. Danke euch für die lustigen Mittagspausen, die doch manchmal notwendige Seelsorge und natürlich, nicht zu vergessen, den wissenschaftlichen Austausch, der mich auch vorangetrieben hat.

Als letztes möchte ich mich noch bei meinen Korrekturleser\*innen bedanken, die sich tapfer durch die erste Fassung mit meiner konfusem Schreibweise durch gequält haben. Die konstruktive Kritik hat sich hoffentlich bemerkbar gemacht.

Allen, vielen Dank!